A geometric nonlinear solid-shell element based on ANDES, ANS and EAS concepts

by

Mohammadreza Mostafa

B.S., Civil Engineering, Amirkabir University of Technology, Tehran, Iran 2000

M.S., Civil Engineering, Amirkabir University of Technology, Tehran, Iran 2003

M.S., Civil Engineering, University of Colorado at Boulder, Boulder, CO, US 2011

A thesis submitted to the

Faculty of the Graduate School of the

University of Colorado in partial fulfillment

of the requirements for the degree of

Doctor of Philosophy

Department of Civil, Environmental and Architectural Engineering

2011

This thesis entitled:
A geometric nonlinear solid-shell element based on ANDES, ANS and EAS concepts
written by Mohammadreza Mostafa
has been approved for the Department of Civil, Environmental and Architectural Engineering

Prof. Mettupalayam Sivaselvan

Prof. Carlos Felippa

Date _____

The final copy of this thesis has been examined by the signatories, and we find that both the content and the form meet acceptable presentation standards of scholarly work in the above mentioned discipline.

Mostafa, Mohammadreza (Ph.D., Civil Engineering)

A geometric nonlinear solid-shell element based on ANDES, ANS and EAS concepts

Thesis directed by Prof. Prof. Mettupalayam Sivaselvan

In this work, first, a computational approach suitable for combined material and geometrically nonlinear analysis for 2D quadrilateral elements is explained. Its main advantage is reuse: once a finite element has been developed with good performance in linear analysis, extension to material and geometrically nonlinear problems is simplified. Extension to geometrically nonlinear problems is enabled by a corotational kinematic description, and that to material nonlinear problems by an optimization-based solution algorithm. The approach thus comprises three ingredients — the development of high performance linear finite element using the Assumed natural deviatoric strain (ANDES) concept, a corotational kinematic description for quadrilateral element, and an optimization algorithm. The work illustrates the realization of the three ingredients on plane stress problems that exhibit elastoplastic material behavior. Numerical examples are presented to illustrate the effectiveness of the approach.

Second, an eight-node solid-shell element based on ANS, ANDES and EAS concepts is presented. The mechanical response of the element is split into three parts: 1) In-plane response, which is also decomposed into membrane and bending, 2) Thickness response or normal strains in thickness direction; and 3) Transverse shear response. This separation gives the liberty of using any type of membrane quadrilateral formulation for the in-plane response. In the present work, ANDES membrane element is used for the in-plane response. ANS concept is implemented to account for the transverse shear and thickness strains, which has proven to circumvent the curvature thickness and transverse shear locking problems. EAS approach with one degree-of-freedom is applied on the thickness strain so as to alleviate the Poisson thickness locking. The formulation yields exact solution for both membrane and

bending patch tests.

Third, an eight-node solid-shell element based on ANS and EAS concepts is presented. Five enhanced degrees-of-freedom are used to improve the in-plane response of the element and one to alleviate the Poisson's thickness locking problem.

Numerical results for some benchmarks show the robustness of both solid-shell formulations in geometrically linear problems.

With the proposed linear element at hand, the corotational kinematic description is used to add geometric nonlinearity to this work. Problems with small strains are addressed in this work, however, EICR could be extended to large deformations. The Corotated frame is defined such that it is independent of whether the mid-surface is warped or not. Numerical results for geometric nonlinear solid-shell and the comparisons with other solid-shell and shell formulations are presented in the end.

Dedication

To my parents who spent their whole life on raising and training me.

Acknowledgements

I would like to express my gratitude to Prof. Mettupalayam Sivaselvan for being a cooperative advisor and an outstanding professor. His interest, support, personality and precious suggestions inspired me to fulfill this work successfully. I am highly indebted to my committee members Prof. Carlos Felippa, Prof. Richard Regueiro, Prof. Kurt Maute and Prof. Mahmoud Hussein for their time and considerations for reviewing the current work.

The financial support for this research from the National Science Foundation through the grant CMMI-0847053 is gratefully acknowledged.

Finally, I want to complete the acknowledgment by recognizing the technical conversations I had with Prof. Carlos Felippa, who has been helping me on different aspects of my research.

Contents

Chapter

Tables

Table

10

Figures

Figure

Chapter 1

Introduction

1.1 Motivation

The final goal is to develop computational schemes to study failures of structures. Clearly, it is important to represent degrading behavior. Often, this is done using softening material models. Softening occurs due to processes at smaller scales. Of these, the focus is on softening at a macro-scale due to geometric instabilities in the micro-scales. Two examples could be considered:

(1) Thin-walled steel members that are used very often as structural components, when loaded sufficiently, transition from a mode that can be described by the beam theory, to a mode where the walls locally buckle plastically as shown in Fig. 1.1(a). This *irreversible* transition leads to reduced engineering utility of system which is referred to as *"Deterioration"* and should be taken into account in the analysis procedure.

(2) Buckling of honeycomb cellular microstructures. Consider the 2D RVE (Representative Volume Element) shown in figure 1.1(b) which is under compressive in-plane force. As can be seen in the deformed shape, the membranes buckle locally. This phenomenon is analogous to the local buckling of the thin-walled columns under compression. Table 1.1 summarizes the the two examples.

One approach to investigate the mentioned effect is fine-grained modeling with finite element using shell elements (which is referred to as the *micro-scale*). This approach is impractical

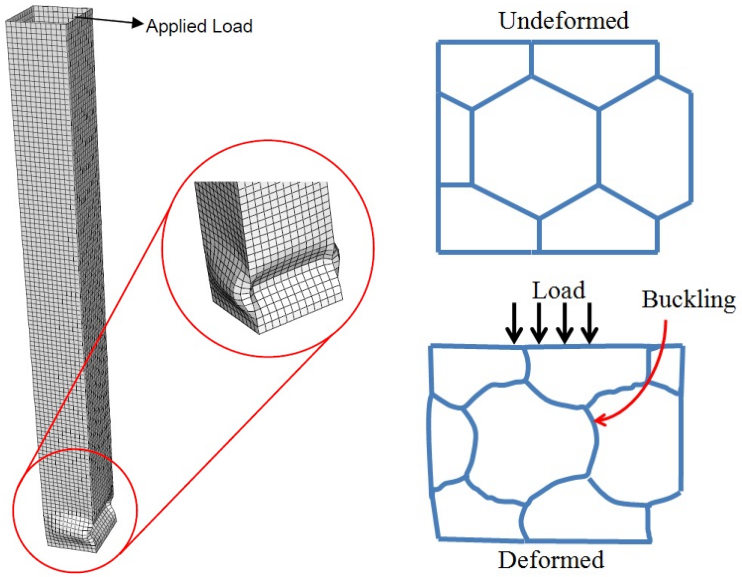

Figure 1.1: Degradation examples;(a)plastic softening of a thin-walled column, (b)buckling of membranes in honeycomb cellular microstructures .

Table 1.1: Summary of model examples

Node	Beam model	Cellular microstructures
Micro-scale	Continuum.	Walls can be considered as flexural components.
Macro-scale	Skeletal structure.	Homogenized continuum.
Remarks	Local buckling appears as softening in moments-rotation model.	Buckling in micro-scale appears as softening in continuum strain-stress model.

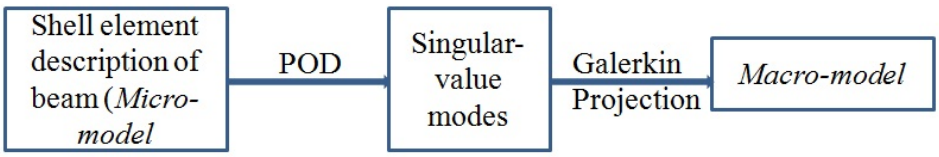

Figure 1.2: Steps from micro-model to macro-model.

when modeling a structure with a large number of members in terms of the number of degrees-of-freedom and analysis time.

The philosophy behind models of deterioration used in structural engineering practice, is to modify constitutive equation to model the observed behavior [134, 75, 132, 51].

> *Strategy*: "Rationally include in macro-model *states* that represent modes of instability in micro-model using model reduction."

In order to develop a macro-scale model, it is required to start from describing the micro-scale behavior and to obtain a similar description of the macro-scale behavior through *structure-preserving model reduction* strategies. This will result, for example, in beam elements, shell elements etc., which in addition to the usual degrees of freedom, will have the *deterioration modes* built in. These elements can then be used to develop system scale models. Developing the macro-scale model could be done by *Proper Orthogonal Decomposition (POD)* [81, 43] and *Galerkin Projection* [85].

Figure 1.2 depicts the steps to develop a macro-model for Beam element as an structural member:

In this research, the micro-model capable of modeling the nonlinear behavior of 3D thin structures has been investigated. Shell elements are one of the most popular and versatile tools that can model 3D structures. The application of shell elements ranges from aerospace structures such as wing of an airplane to columns and slabs of a building. Many authors have worked on different shell element formulations; each of which is suitable for a specific problem.

During the past decade, solid-shell has been introduced as a new class of finite elements which has a three dimensional geometry (like solid element), but behaves similar to degenerated or classical shell finite elements. The advantages of solid-shell to shell formulations are: the capability of modeling the 3D geometry of the structure, modeling the boundaries without any extra kinematic assumptions and avoiding the complicated updating of rotation vector in nonlinear problems.

Corotational kinematic description is one of the approaches to address the geometric nonlinear behavior of the structure. It is based on splitting the motion of the element into rigid-body and deformational displacements. The advantage of this approach is "reusing" the linear element library in developing the nonlinear element. This kinematic description is not restricted to small strain problems and is extensible to finite deformations too.

1.2 Outline of the thesis

In chapter 2 of this research a computational approach suitable for combined material and geometrically nonlinear analysis of 2D plane stress element is presented. Corotational kinematic description is applied to take the geometric nonlinearity into account and an optimization-based solution algorithm is used to address the material nonlinearity. ANDES quadrilateral element is introduced (which is a hight performance 2D element) and used as the linear formulation in this chapter.

In chapter 3, first the linear solid-shell element based on the ANDES, ANS and EAS schemes is presented and in the end, the geometric nonlinearity of the element is investigated using Corotational kinematic description.

In chapter 4, a linear solid-shell element based on the ANS and EAS schemes with six enhanced degrees-of-freedom is presented.

In chapter 5 the nonlinear solution algorithm that is used in this work is reviewed and in chapter 6 some numerical examples for both 2D and 3D elements are presented and the results are compared to some other existing formulations.

Finally in chapter 7 the achievements of this research are summarized and the topics for further investigations are discussed.

Chapter 2

Material and geometrically nonlinear analysis Of 2D quadrilateral ANDES element using the optimization scheme

2.1 Introduction

A computational approach suitable for combined material and geometrically nonlinear analysis by the Finite Element Method is presented. Its main advantage is reuse: once a finite element has been developed with good performance in linear analysis, extension to material and geometrically nonlinear problems is simplified. Extension to geometrically nonlinear problems is enabled by a corotational kinematic description, and that to material nonlinear problems by an optimization-based solution algorithm. The approach thus comprises three ingredients — the development of high performance linear finite element using the Assumed Natural Deviatoric Strain (ANDES) concept, a corotational kinematic description, and an optimization algorithm. The main constraint in the application of the corotational formulation is restriction to small strains. The realization of the three ingredients on plane stress problems that exhibit elastoplastic material behavior is illustrated. Numerical examples are presented to illustrate the effectiveness of the approach. The ANDES linear quadrilateral element passes the uniform strain patch test proposed by MacNeal [92], and shows excellent convergence characteristics in other well-known benchmark problems. For nonlinear problems, comparison of results is made with respect to solutions provided by the commercial nonlinear code ABAQUS as reference, which are presented in chapter 6.

2.2 Templates and the ANDES Quadrilateral Element

It is well known that isoparametric displacement models of low order are susceptible to various types of locking behavior (by "locking" we mean abnormally large stiffness in response to some deformation patterns). Various remedies have been developed over the past four decades to cure or alleviate such behavior. Of particular interest for the applications addressed here is the in-plane bending response of four-node quadrilateral membrane (plane stress) elements. Remedies have included modifications in the formulation of the displacement element proper such as reduced, selective reduced and directional integration, and incompatible modes (example [74, 151]), assumed stress formulations (example [71, 107]), assumed strain formulations (example [90, 17, 105, 130]), and the free formulation [28, 31]. It has been shown in [53] that many of these formulations, in fact all of those that satisfy the Individual Element Test (IET) of Bergan [29], can be unified in the form of finite element **templates**.

Templates represent an outgrowth and generalization of the key idea behind the Free Formulation [28, 31]. The element stiffness behavior is decoupled into two portions: **basic** and **higher order**. The basic stiffness component embodies the response to rigid body and constant strain displacement patterns, which are collectively called **basic modes**. The higher order stiffness responds to **higher order deformational patterns**, collectively called **higher order modes**, which are orthogonal (in an energy sense) to basic modes. Together these two components provide the correct element rank, thus guaranteeing stability. The orthogonality property means that an element derived this way automatically satisfies the Individual Element Test of Bergan, which is a restricted form of the conventional patch test, thus satisfying consistency and completeness.

The template approach can generate families of elements by including **free parameters** in the basic and higher order stiffness matrices. Setting specific numerical values for the parameters produces **instances** of the template. Instances may either reduce to existing

elements, or provide new elements. The parametrized higher order stiffness may be formulated by a wide spectrum of methods: assumed displacements, assumed strains, assumed stresses, or combinations thereof. In this article, a variation of the assumed strain approach, the so-called Assumed Natural DEviatoric Strain (ANDES) formulation, is used.

The ANDES formulation was introduced by Felippa and Militello [98, 58] for membrane and bending components of shell elements. For the 2D quadrilateral, the ANDES formulation proceeds as follows:

(1) Mixed variational principle: The ANDES approach starts from a two-field mixed variational principle with displacement (u) and strain (e) as the independent fields. The Tonti diagram shown in Figure 2.1 serves as a useful mnemonic to construct such a principle (example, [54]). The weak form with the independent displacement and strains fields is

$$\int_V (e - e^u) \cdot \delta\sigma^e \, \mathrm{d}V + \int_{S_t} (t^p - \sigma^e n) \cdot \delta u \, \mathrm{d}S + \int_V (D^* \sigma^e + b) \cdot \delta u \, \mathrm{d}V = 0 \tag{2.1}$$

Following a standard application of the divergence theorem, this can be recognized as the stationarity condition of the two-field functional

$$\begin{aligned} \Pi(u, e) = \int_V \frac{1}{2}(e - e^u) \cdot E \cdot (e - e^u) \, \mathrm{d}V - \int_V \frac{1}{2} e^u \cdot E \cdot e^u \, \mathrm{d}V \\ + \int_V b \cdot u \, \mathrm{d}V + \int_{S_t} t^p \cdot u \, \mathrm{d}S \end{aligned} \tag{2.2}$$

Since the variations δu and δe are independent, we have the two separate conditions

$$\begin{aligned} \int_V (e - e^u) \cdot E \cdot \delta e \, \mathrm{d}V = 0 \\ \int_V \sigma^e \cdot \delta e^u \, \mathrm{d}V = \int b \cdot \delta u \, \mathrm{d}V + \int_{S_t} t^p \cdot \delta u \, \mathrm{d}S \end{aligned} \tag{2.3}$$

The first equation of (2.3) could be interpreted as minimizing the following dislocation energy resulting from incompatible strains (**least squares strain fitting**) [56].

$$J(e) = \int_V \frac{1}{2}(e - e^u) \cdot E \cdot (e - e^u) \, \mathrm{d}V \tag{2.4}$$

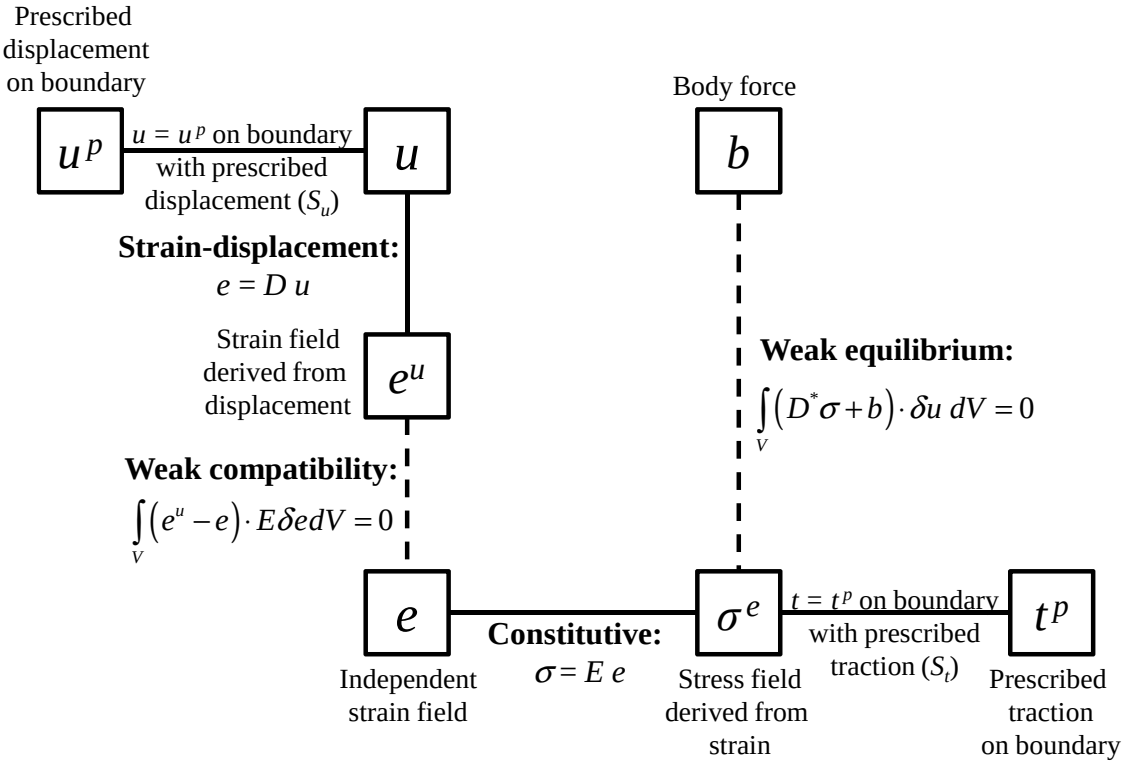

Figure 2.1: Tonti diagram representing the two-field variational principle that is the basis of the ANDES approach. Solid lines represent relations that apply pointwise, and dashed lines those are enforced in weak form. D denotes the strain-displacement operator, and D^* its adjoint.

(2) Assumed strain field: The element kinematics may be visualized using "strain gages" as shown in Figure 2.2. The assumed strain components, χ, can be thought of as the strains in these gages. The gages at the intersection of the element medians (χ_1, χ_2, χ_3) represent the constant **Cartesian** strains (basic modes). The gages at the edges (χ_4, χ_5) represent **natural** strains that are interpolated linearly to obtain the bending (higher order) modes. The significance of this separation into Cartesian and natural strains is that in elements with arbitrary geometry (i.e., where the Jacobian of the transformation for natural to Cartesian coordinates is not constant), the basic constant strains (corresponding to χ_1, χ_2, χ_3) have to be defined in Cartesian coordinates and the higher order strains in natural coordinates in order to pass the patch test as discussed in [53]. The resulting assumed strain field is [55]:

$$e(\xi,\eta) = \begin{pmatrix} e_{xx} \\ e_{yy} \\ \gamma_{xy} \end{pmatrix} (\xi,\eta) = \underbrace{\begin{bmatrix} 1 & 0 & 0 & c_m^2(\eta-\eta_c) & c_n^2(\xi-\xi_c) \\ 0 & 1 & 0 & s_m^2(\eta-\eta_c) & s_n^2(\xi-\xi_c) \\ 0 & 0 & 1 & 2c_m s_m(\eta-\eta_c) & 2c_n s_n(\xi-\xi_c) \end{bmatrix}}_{B^n} \begin{pmatrix} \chi_1 \\ \chi_2 \\ \chi_3 \\ \chi_4 \\ \chi_5 \end{pmatrix} \tag{2.5}$$

where the higher order natural strain components have been transformed to Cartesian components. (c_m, s_m) and (c_n, s_n) are the direction cosines of the images of the ξ and η axes, and (ξ_c, η_c) the coordinates of the pre-image of the the centroid of the element, under the isoparametric map.

Substituting $u(\xi,\eta) = N(\xi,\eta)u^Q$, $e^u(\xi,\eta) = B^{\text{iso}}(\xi,\eta)u^Q$, $e = B^n(\xi,\eta)\chi$ into (2.3) and writing the equations in matrix form, yields a system of equations of the form

$$\left[\begin{array}{c|c} 0 & K_{12} \\ \hline K_{12}^T & K_{22} \end{array}\right] \left(\begin{array}{c} u^Q \\ \hline \chi \end{array}\right) = \left(\begin{array}{c} f^Q \\ \hline 0 \end{array}\right) \tag{2.6}$$

$$\begin{aligned} K_{12}K_{22}^{-1}K_{12}^T u^Q = K^Q u^Q = f^Q \\ \chi = K_{22}^{-1}K_{12}^T u^Q = T^Q u^Q \end{aligned} \tag{2.7}$$

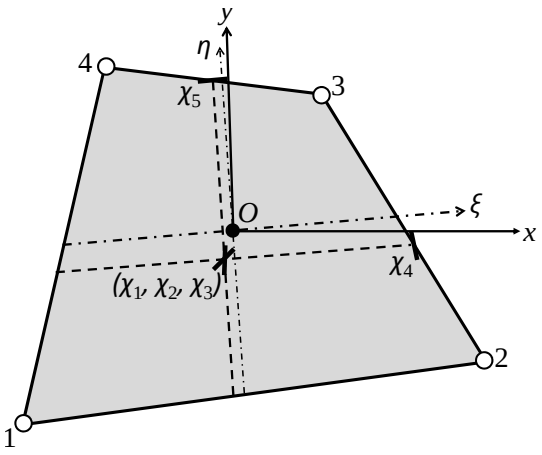

Figure 2.2: Element kinematics represented by "strain gages" (x, y indicate Cartesian coordinates, ξ, η indicate isoparametric coordinates)

where u^Q and f^Q are the vectors of nodal displacements and internal forces of the quadrilateral element, $N(\xi, \eta)$ is the matrix of the usual isoparametric shape functions and B^{iso} the corresponding strain-displacement matrix, and e is the assumed strain field and K^Q is the stiffness matrix of the quadrilateral element.

For the linear higher order strain as used in equation (2.5), the second equation of (2.7) takes the surprisingly simple form [1] [53]:

$$\chi = \underbrace{\begin{bmatrix} B^{\text{iso}}(\xi_C, \eta_C) \\ W H_h \end{bmatrix}}_{T^Q(x,y)} u^Q \tag{2.8}$$

Here, H_h is a filter matrix that extracts from u^Q the higher order modes, and is identical for all quadrilateral elements. Equation (2.8) is an instance of the quadrilateral finite element template, parametrized by W. Expressions for the filter matrix H_h, and for the matrix W in the ANDES instance, are given in [53] in terms of invariants of the quadrilateral geometry.

[1] Following reference [53], E is selected to be identity in calculating the χ in second of equation (2.7). This assumption only affects the bending modes (WH_h) and yields the simplified form shown in equation (2.8).

It is easy to check that the higher order modes are energy orthogonal to the basic modes, which guarantees the convergence of the formulation as discussed in [28]. Considering the basic mode strain-displacement matrix $B_b^Q = B^Q(\xi_C, \eta_C)$, and the higher-order mode strain-displacement matrix $B_h^Q = B^Q(\xi, \eta) - B_b^Q$, the energy-orthogonality requirement between the basic and higher order modes is expressed as

$$\int_V (B_h^Q)^T E B_b^Q dV = 0 \tag{2.9}$$

(3) Strain-displacement matrix: From equations (2.5) and (2.8), the strain-displacement matrix, B^e, can be obtained as

$$e(\xi, \eta) = \underbrace{B^n(\xi, \eta) \begin{bmatrix} B^{\text{iso}}(\xi_C, \eta_C) \\ W H_h \end{bmatrix}}_{B^Q(\xi,\eta)} u^Q \tag{2.10}$$

Equipped with this linear element, its extension to geometric and material nonlinearity are discussed next.

2.3 Corotational kinematic description

The corotational kinematic description is based on decomposing the motion of an element into rigid body and deformation components. Deformations are described with reference to a coordinate frame that translates and rotates with the element. For a plane quadrilateral element, this is depicted in Figure 2.3. The idea is analogous to the right polar decomposition ($F = RU$) of continuum mechanics. An attractive feature of the corotational description, particularly for small strain problems, is that elements that perform well in geometrically linear problems can be extended to nonlinear problems in an **element independent** fashion. This approach referred to as an Element-Independent Corotational formulation (EICR) was introduced by Rankine and Brogan [112]. Felippa and Haugen [57, 68] present a unified formulation of the corotational approach for 3D elements with both

translational and rotational degrees of freedom. In this article, a corotational formulation for the plane quadrilateral element is considered. The formulation mirrors that of Battini [22]. However, it is presented in a manner that its relationship with the unified 3D formulation of [57] is more readily apparent.

Let $\mathcal{R}$ be the matrix representation of the rotation shown in Figure 2.3. Let $R = \text{diag}(\mathcal{R}, \mathcal{R}, \mathcal{R}, \mathcal{R})$. Denote by P_T, the matrix that averages nodal quantities, so that for example $\bar{X}^e = (I - P_T)X^e$ where I is the identity. It can be easily verified that P_T is symmetric, and commutes with rotations (this is true in 3D as well when only translational degrees of freedom are considered). Furthermore, P_T is a projection, so that $(I - P_T)^2 = (I - P_T)$, and $(I - P_T)\bar{X}^e = \bar{X}^e$. In 2D, R is parametrized by a scalar angle of rotation, θ. By direct calculation, $R\left(\frac{dR}{d\theta}\right)^T = \iota$, where $\iota = \text{diag}(\begin{bmatrix} 0 & 1 \\ -1 & 0 \end{bmatrix}, \begin{bmatrix} 0 & 1 \\ -1 & 0 \end{bmatrix}, \begin{bmatrix} 0 & 1 \\ -1 & 0 \end{bmatrix}, \begin{bmatrix} 0 & 1 \\ -1 & 0 \end{bmatrix})$. ι commutes with rotations and with $(I - P_T)$, and $\iota^2 = -I$. From Figure 2.3, it can be seen that the deformational displacements u_d^e are related to the total displacements u^e by

$$\begin{aligned} u_d^e &= R^T(I - P_T)(X^e + u^e) - \bar{X}^e \\ &= (I - P_T)R^T(X^e + u^e) - \bar{X}^e \text{ since } P_T \text{ commutes with rotations} \end{aligned} \tag{2.11}$$

Differentiating equation (2.11) (this may also be thought of as considering variations),

$$\dot{u}_d^e = (I - P_T)R^T\dot{u}^e + (I - P_T)R^T\iota(X^e + u^e)\dot{\theta} \tag{2.12}$$

A number of choices exist for determining the rotated frame given the total displacements at the nodes. Here, the strategy of Battini [22] is used where θ is chosen to minimize the norm of the deformational displacements, $\frac{1}{2}||u_d^e||^2$. This gives

$$(\bar{X}^e)^T R(\theta)^T \iota (I - P_T)(X^e + u^e) = 0 \tag{2.13}$$

which can be solved for θ (the resulting explicit formula for θ can be found in [22]). Differentiating equation (2.13), and using the relationships between different matrices discussed above gives the following expression for $\dot{\theta}$.

$$\dot{\theta} = \frac{1}{(\bar{X}^e)^T R^T (I - P_T)(X^e + u^e)} (\bar{X}^e)^T R^T \iota (X^e + u^e) \tag{2.14}$$

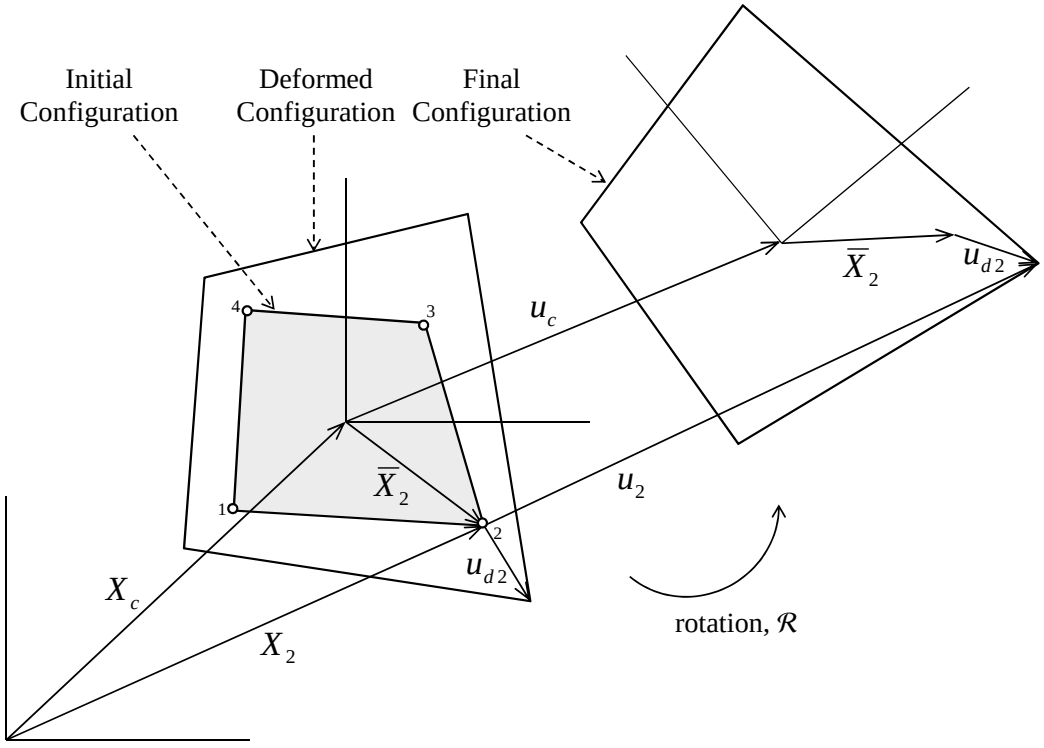

Figure 2.3: Corotational kinematic description: It can be seen that $X_c + u_c + \mathcal{R}(\bar{X}_2 + u_{d2}) = X_2 + u_2$. This is the basis of equation (2.11). (Notation: $u_d^e = (u_{d1}^T, u_{d2}^T, u_{d3}^T, u_{d4}^T)^T$, $u^e = (u_1^T, u_2^T, u_3^T, u_4^T)^T$)

Substituting in equation (2.12), and defining $U = \iota \bar{X}^e$ and $V = \iota R^T (I - P_T)(X^e + u^e)$ results in

$$\dot{u}_d^e = \underbrace{(I - P_T)\left(I - \frac{VU^T}{U^T V}\right)}_{\mathcal{P}} R^T \dot{u}^e \tag{2.15}$$

It is recognized that the matrix $\mathcal{P}$ is a projector as well. If deformations within the corotational frame are assumed small, then equation (2.10) can be differentiated and combined with equation (2.15) to give

$$\dot{e}(\xi, \eta) = B^e(\xi, \eta) \mathcal{P} R^T \dot{u}^e \tag{2.16}$$

This equation describes the nonlinear kinematics of the element. Next, the strategy for material nonlinear computations is presented.

2.4 Optimization algorithm for elastoplastic state update

In the presence of nonlinear material behavior, the displacements and other states of a model are usually computed in a nested fashion. In each increment, a displacement increment is computed from a linearized global equilibrium equation. This displacement increment is then used to determine compatible strain increments at material points. The strain increments are in turn used to compute increments of stresses and other states at material points using constitutive equations. These updated stresses result in an imbalance in the global equilibrium equation, as well as in a new linearization of this equation. A Newton-type method is used to iteratively reduce this imbalance to within a tolerance.

In the present research , a different approach is used to compute the state of the model in an increment. This computation is cast as a **mathematical program**. This approach was first proposed by Maier [93]. Although in the present work only elastic ideal plastic behavior is considered, the approach is applicable wherever the material model can be derived from free energy and dissipation functions. Such models belong to the class of **generalized standard materials** [66]. If the free energy and dissipation functions are convex, then the mathematical program is one of convex minimization. For details, the reader is referred to

[133, 84]. The approach obviates the need for a constitutive model-specific return mapping algorithm.

For a hyperelastic material, the stress is related to the elastic strain by $\sigma = \nabla\psi(e_e)$, where ψ is the free energy and e_e is the elastic strain. The dual consititutive relationship is $e_e = \nabla\psi^c(\sigma)$, where ψ^c is the **complementary** free energy. For ideal plasticity with yield function ϕ, the inelastic part of the constitutive law can be stated in a similarly concise manner as $\dot{e}_p = \nabla\varphi^c(\sigma)$. Here, φ^c is the complementary dissipation function, which for ideal plasticity is the indicator function of the elastic region. With the assumption of small strains within the corotated frame, the additive decomposition of the strain rate into elastic and plastic rates, $\dot{e} = \dot{e}_e + \dot{e}_p$, gives

$$\frac{d}{dt}\nabla\psi^c(\sigma) + \nabla\varphi^c(\sigma) - \dot{e} = 0$$

for each material point. Collecting these equations for all material points,

$$\frac{d}{dt}\nabla\psi^c(\sigma) + \nabla\varphi^c(\sigma) - B(u)\dot{u} = 0 \tag{2.17}$$

where B is the collection of the matrices $B^e(\xi,\eta)\mathcal{P}R^T$ of equation (2.15) and σ, the collection of stresses over all material points. u is the collection of displacements over all nodes. The dependence of B on u is because $\mathcal{P}$ and R depend on u^e. This equation discretized in time together with the global equilibrium condition is

$$\begin{gathered}\frac{\nabla\psi^c(\sigma_{n+1}) - \nabla\psi^c(\sigma_n)}{\Delta t} + \nabla\varphi^c(\sigma_{n+1}) - B(u_n)\frac{u_{n+1}-u_n}{\Delta t} = 0 \\ B_f(u_n)^T\sigma_{n+1} = f_{n+1}\end{gathered} \tag{2.18}$$

where f_{n+1} is the vector of external nodal forces at time $n+1$. The fact that $B(u_n)$ is used in the discretization implies the geometry is updated in an explicit fashion. Further, the matrix B is partitioned as $B = [B_f\ B_p]$ corresponding to free DOF, and boundary DOF with prescribed displacements respectively. The discrete equation can be rearranged to obtain

the following convex minimization problem [133].

$$\begin{gathered} \sigma^{n+1} = \underset{\sigma}{\operatorname{argmin}}\, \psi(\sigma) - b^T\sigma \\ \text{subject to } B_f(u_n)^T\sigma = f_{n+1} \text{ (equilibrium equality constraints)} \\ \phi(\sigma) \leq 0 \text{ (yield equality constraints)} \end{gathered} \tag{2.19}$$

where f is the vector of nodal forces, and $b = B_p(u_n)\Delta u_p + \nabla\psi^c(\sigma_n)$. In words, the optimization problem reads "of all the stresses that satisfy equilibrium and the yield conditions, find the one that minimizes the total complementary potential energy". But for the yield conditions, this statement can be recognized as the principle of complementary potential energy from elementary mechanics. Displacement increments are computed as the Lagrange multipliers corresponding to the equality (equilibrium) constraints of the optimization problem (2.19). Recently, efficient algorithms have been developed to solve large scale problems of this type [133, 84], where a system of equations whose size is the number of free DOF needs to be solved in each iteration.

In the present research, the function `fmincon` in the Matlab Optimization Toolbox [95] is used to solve this problem.

Chapter 3

Solid-shell element based on ANDES, ANS and EAS concepts

3.1 Introduction

Shell finite elements are commonly used to model three dimensional structures in which the dimension in one direction (referred to as the thickness direction) is much smaller than the extents in the other two directions. Shell elements may be classified into three broad categories — (i) classical shell elements, (ii) degenerate shell elements, and (iii) solid-shell elements. Classical shell elements are built on the theory of plates and shells, and have nodes with rotational degrees of freedom [32, 34, 76, 37, 89]. Degenerated shell elements start from the continuum theory, but impose constraints to degenerate the kinematics to the shell surface [24, 17, 126, 131, 128, 42]. These elements also have nodes that possess rotational degrees of freedom. Solid-shell elements resemble solid elements in that their nodes have only translational degrees of freedom. However, special measures are taken to overcome problems arising from the thickness being much smaller than the other two dimensions of the element.

In this chapter, a solid-shell formulation is developed using an assumed-strain approach. Attractive features of a solid shell element include (i) simplification resulting from avoiding 3D rotational degrees of freedom (in fact, this work was motivated by an application in model reduction, where the element configuration space with only translational degrees of freedom has a simpler vector space structure), (ii) representation of 3D boundary conditions without need for additional kinematic assumptions, and (iii) coupling with solid elements without

additional kinematic constraints. Examples of the early work on solid-shell are addressed in references [104, 97, 69, 70]. Schwarze and Reese [119] present a comprehensive survey of different solid-shell element formulations.

In modeling shell structures, shape functions of displacement-based solid elements are not rich enough to capture kinematics associated with bending perpendicular to the shell surface. As a result, solid-shell elements are susceptible to various locking phenomena.

(1) *Membrane locking*: happens when the element is subjected to in-plane longitudinal or transverse(shear) loads and the low order shape functions are not capable of modeling the physical behavior of the element.

(2) *Transverse shear locking*: occurs when the element thickness tends to zero or physically speaking the element has high aspect ratio in terms of length versus thickness. EAS method is one way to reduce the effect of parasitic shear terms, see references [6, 8] for small strains and [9, 59] for large strains. Another remedy is the ANS concept, see references [72, 150, 50] for shell and [69, 142, 147, 82, 148, 55, 41, 119] for solid-shell elements.

(3) *Poisson thickness locking*: happens when the displacement is assumed to vary linearly in the thickness direction and as a result the thickness strain becomes constant. However, due to Poisson's effect, the thickness strain is coupled with the in-plane strains that vary linearly across the thickness. This discrepancy results in Poisson thickness locking. The remedies to this defect could be: a) assuming a quadratic displacement distribution in thickness direction, which produces linear thickness strain in thickness direction [104]; b) using EAS degrees-of-freedoms and enhancing the thickness strain to vary linearly across the thickness [119] or c) dividing the strain in thickness direction into a membrane (constant) and bending (linear) part and enforcing the bending stress to be zero [69].

(4) *Curvature* or *trapezoidal locking*: This occurs when the element edges in thickness direction are not perpendicular to the element mid-plane. This type of locking happens in modeling curved structures with solid-shell where the elements are thickness tapered. ANS concept has shown to circumvent the mentioned defect as can be found in references [33, 34, 119].

In the present work, an assumed strain approach is taken for the solid-shell element formulation. The element kinematics is decomposed into in-plane (or membrane), transverse shear and thickness components. The assumed natural deviatoric strain (ANDES) concept, which represents an evolution of the free formulation (FF) [28] and of the assumed natural strain (ANS) formulation, will be used to model the in-plane behavior of the solid-shell. The ANDES approach helps to alleviate membrane locking. Assumed natural strain (ANS) fields are constructed for the out-of-plane components, i.e. transverse shear and thickness components, by computing compatible strains at collocation points and interpolating these strains. This approach mitigates transverse shear locking and curvature locking. In addition, the thickness strain is enhanced to represent linear variation associated with out-of-plane bending. This is necessary to avoid Poisson thickness locking. Gauss integration of full order is used in the formulation. This combined approach is found to result in accurate numerical solutions in challenging benchmark tests.
In general, the mid-surface of a generic solid-shell element is warped and applying the ANDES schme on that warped surface makes the in-plane stiffness polluted with respect to the rigid body modes, i.e. rigid body motions produce nonzero in-plane strains. In order to circumvent that the projection method introduced in reference [113] is used.

Various approaches have been taken in the literature to formulating solid-shell elements with nonlinear kinematics. For example, Schwarze and Reese [120] developed a reduced integration geometric nonlinear element based on total Lagrangian kinematics, while Meraim

and combescure [2, 3] used an updated Lagrangian approach. Other examples of geometric nonlinear solid-shell formulations include [41, 7, 4, 140]. In the current work, the solid-shell element formulation is extended to the geometric nonlinear regime using a corotational kinematic description. The corotational kinematic description pioneered by Wempner [149] and Belytschko and co-workers [23]. Among different CR formulations in the literature (as example see [57] for the history of the formulations), the 'element independent' approach known as (EICR) is selected, which was first introduced by Rankin and Brogan [112]. This approach is based on the use of projection operators. This approach has been widely used on shells (as examples [68, 78, 138, 21]) and continua (as examples [49, 99]). The EICR scheme is of interest since the linear element kernel is reused in developing the geometric nonlinear element and the element library need not be drastically modified. It is noted that EICR is not restricted to small strains and could be extended to address the peroblems with large deformations (e.g. see [114]), but we only address problems with small strains in the current work. The corotated coordinate is defined in such a way that it is independent of whether or not the mid-surface is warped. The element internal force and consistent tangent stiffness matrix are derived by taking variations of the internal energy with respect to nodal degrees-of-freedom to preserve the **consistency** requirement.

The proposed solid-element is tested against several well-known benchmarks, the results of which are presented in chapter 6.

3.2 Linear element formulation

In this section, a solid-shell element formulation based on linearized kinematics is presented. The element geometry is shown in Figure 3.1. One of the directions is identified as the shell-thickness direction. A node-numbering convention is adopted so that edges between nodes (1, 2, 3, 4) and (5, 6, 7, 8) correspond to the thickness direction. Faces 1–2–3–4 and 5–6–7–8 thus constitute the bottom and top surfaces of the element, and the remaining four faces are *in-plane* surfaces. In formulating the element, it proves convenient to

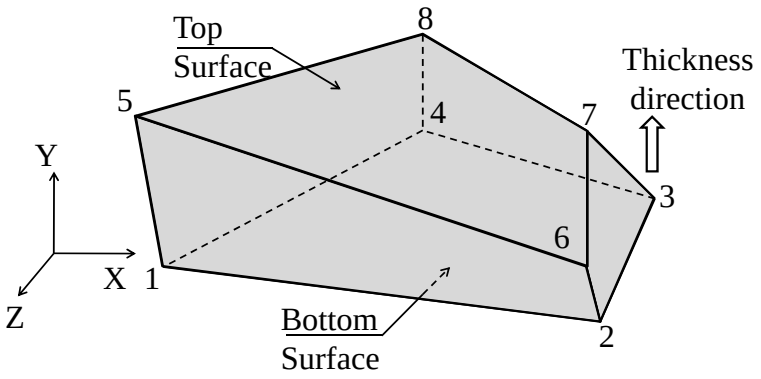

Figure 3.1: The original solid-shell element, warped geometry

introduce different coordinate systems. First these coordinate systems are presented. Next a kinematic decomposition of the element behavior is discussed, motivating the construction of assumed-strain fields. This chapter is concluded by formulating the element stiffness matrix assuming isotropic linear elastic material behavior.

We make a general note on the notation used in the remainder of the chapter. Vectors are denoted by boldface letters, and their components by italicized letters with subscripts. Boldface letters with superscript "e" denote collections of vector components over all the nodes of the element. For the solid-shell element presented here, such vectors are of length 24. Boldface letters with superscript "C" denote averages over the nodes of the element. Therefore, such vectors of length 3. Boldface letters with any other superscript represent vector components at a specific node or point, the superscript being the label or index of the node or point. Boldface letters with no superscripts denote vector fields over the element. Components of vectors are denoted by the corresponding medium weight italicized characters. Matrices and scalars are denoted by italicized letters. The following notation for

a 3×3 matrix M, and a 3-vector $\mathbf{v}$ are also found useful in the derivations that follow.

$$\operatorname{diag}(M) = \begin{array}{c} \\ 1 \\ \vdots \\ n^{\mathrm{e}} \end{array} \begin{array}{c} \begin{array}{ccc} 1 & \cdots & n^{\mathrm{e}} \end{array} \\ \begin{bmatrix} M & & \\ & \ddots & \\ & & M \end{bmatrix} \end{array}; \quad \operatorname{array}(M) = \begin{array}{c} \\ 1 \\ \vdots \\ n^{\mathrm{e}} \end{array} \begin{array}{c} \begin{array}{ccc} 1 & \cdots & n^{\mathrm{e}} \end{array} \\ \begin{bmatrix} M & \cdots & M \\ \vdots & \ddots & \vdots \\ M & \cdots & M \end{bmatrix} \end{array};$$

$$\text{and} \quad \operatorname{stack}(\mathbf{v}) = \begin{array}{c} \\ 1 \\ \vdots \\ n^{\mathrm{e}} \end{array} \begin{array}{c} \begin{array}{c} 1 \end{array} \\ \begin{bmatrix} \mathbf{v} \\ \vdots \\ \mathbf{v} \end{bmatrix} \end{array}$$

where n^{e} is the number of nodes in the element (8 for the solid-shell element presented here), and in each case the number of block row and column repetitions is shown on the border. Other specific notation is described as it appears.

3.2.1 Coordinate systems

In the following, the coordinate systems used in the solid-shell element formulation are presented in order. The base coordinate system in which equilibrium is considered is termed the global coordinate system. Vectors in this coordinate system are denoted by boldface uppercase letters. For example, the position of the all the nodes is denoted by $\mathbf{X}^{\mathrm{e}}$, and their displacements $\mathbf{U}^{\mathrm{e}}$.

3.2.1.1 Local coordinate system

First a coordinate system local to the element is constructed. Vectors in this coordinate system are denoted by boldface lowercase letters. The construction of the local coordinate system is as follows.

Construction: Referring to Figure 3.2, midpoints of edges 1–5,...,4–8 are labeled 1^{w},...,4^{w} respectively, and the midpoints of lines 1^{w}–2^{w},...,4^{w}–1^{w} are labeled 5^{0},...,8^{0}. In

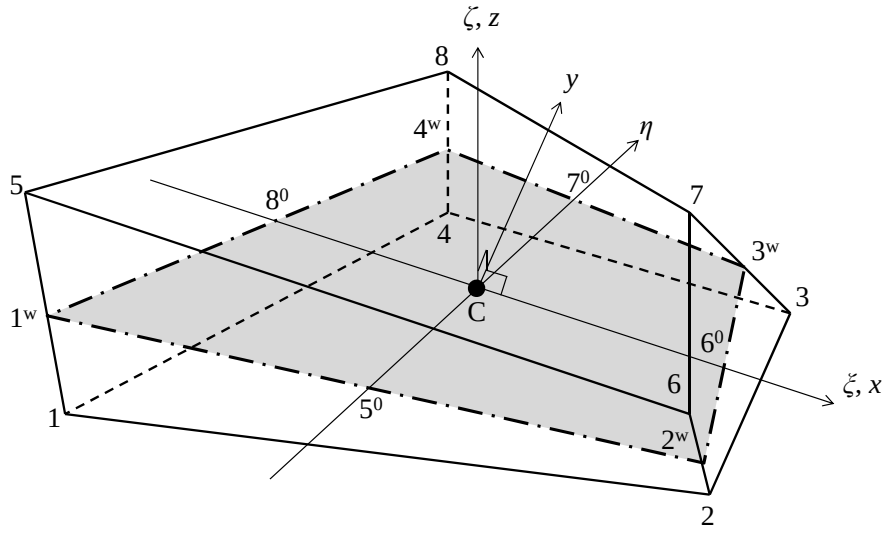

Figure 3.2: Local and natural coordinate systems

general, the mid-surface 1^{w}–2^{w}–3^{w}–3^{w} is not plane, but is warped. However, the lines 5^0–7^0 and 8^0–6^0 intersect at a point C whose global coordinates $\mathbf{X}^{\mathrm{C}}$ are given by the average of the nodal coordinates. This point C is chosen as the origin of the local coordinate system. The plane defined by the lines 5^0–7^0 and 8^0–6^0 is taken as the local xy-plane with x-direction defined along the line 8^0–6^0. The local z-direction is normal to this plane. The components in global coordinates of the unit vectors in the local x, y and z directions are thus obtained as[1]

$$\begin{aligned}
\boldsymbol{\alpha}_x &= \frac{\mathbf{X}^{6^0} - \mathbf{X}^{8^0}}{||\mathbf{X}^{6^0} - \mathbf{X}^{8^0}||} \\
\boldsymbol{\alpha}_z &= \frac{\boldsymbol{\alpha}_x \times (\mathbf{X}^{7^0} - \mathbf{X}^{5^0})}{||\boldsymbol{\alpha}_x \times (\mathbf{X}^{7^0} - \mathbf{X}^{5^0})||} \\
\boldsymbol{\alpha}_y &= \boldsymbol{\alpha}_z \times \boldsymbol{\alpha}_x
\end{aligned} \tag{3.1}$$

The rotation matrix

$$R = \left[\begin{array}{c|c|c} \boldsymbol{\alpha}_x & \boldsymbol{\alpha}_y & \boldsymbol{\alpha}_z \end{array} \right] \tag{3.2}$$

thus transforms components of vectors from local coordinates to global coordinates.

[1] $\boldsymbol{\alpha}$ is an exception to the general notation used for vectors — although it is a lowercase character and does not have a superscript, it represents components in global coordinates, and is not a vector field over the element.

Transformation of positions and displacements: Node positions and displacements are then transformed from global coordinates to local coordinates by

$$\begin{aligned} \mathbf{x}^n &= R^T(\mathbf{X}^n - \mathbf{X}^{\mathrm{C}}) \\ \mathbf{u}^n &= R^T\mathbf{U}^n \end{aligned} \tag{3.3}$$

3.2.1.2 Natural coordinate system

In approximating displacement and strain fields within the element in section 3.2.2, a natural coordinate system is used where the region $[-1,1]\times[-1,1]\times[-1,1]$ is mapped to the region occupied by the element. When positions and displacements need to be approximated, for example in the computation of compatible strains, then the usual trilinear shape functions are used. Thus

$$\begin{aligned} \mathbf{x}(\xi,\eta,\zeta) &= \sum_{n=1}^{8} N^n(\xi,\eta,\zeta)\mathbf{x}^n \\ \mathbf{u}(\xi,\eta,\zeta) &= \sum_{n=1}^{8} N^n(\xi,\eta,\zeta)\mathbf{u}^n \end{aligned} \tag{3.4}$$

where $N^n(\xi,\eta,\zeta) = \frac{1}{8}(1+\xi^n\xi)(1+\eta^n\eta)(1+\zeta^n\zeta)$, (ξ^n,η^n,ζ^n) being the natural coordinates of node n. The Jacobean matrix

$$J(\xi,\eta,\zeta) = \left[\begin{array}{c|c|c} \frac{\partial\mathbf{x}}{\partial\xi} & \frac{\partial\mathbf{x}}{\partial\eta} & \frac{\partial\mathbf{x}}{\partial\zeta} \end{array}\right] \tag{3.5}$$

is used in different occasions in what follows.

3.2.2 Assumed-strain fields

The solid-shell element in this work is developed using an assumed-strain approach. The kinematics of the element are decomposed into three parts, and the assumed-strain field in each part is constructed using a different principle.

(1) *In-plane* deformation: The in-plane assumed-strain field is built using the Assumed Natural Deviatoric Strain (ANDES) concept described in section 2.2. In-plane de-

formation may be thought of as in turn consisting of *membrane* and *bending* components.

(2) *Transverse shear* deformation: Assumed transverse shear strains are derived by the ANS approach.

(3) Deformation in the *thickness* direction: The assumed-strain field in the thickness direction is assembled by a combination of the Assumed Natural Strain (ANS) idea and strain enhancement.

The development of the assumed-strain field is summarized in Figure 3.3. This is elaborated in the following. It is noted that besides the use of the assumed-strain field, no other techniques such as reduced integration and the ensuant hourglass stabilization etc. are used in the element development.

In terms of notation,

$$\mathbf{e}^{\mathrm{C}} = (e_{xx}, e_{yy}, \gamma_{xy}, e_{zz}, \gamma_{yz}, \gamma_{xz})^T$$

denotes the vector strain components in the (Cartesian) local coordinate system, and

$$\mathbf{e}^{\mathrm{n}} = (e_{\xi\xi}, e_{\eta\eta}, \gamma_{\xi\eta}, e_{\zeta\zeta}, \gamma_{\eta\zeta}, \gamma_{\xi\zeta})^T$$

the vector of strain components in natural coordinates. Both vectors, however, are expressed as functions of the natural coordinates to facilitate numerical integration using Gauss quadrature. Furthermore, the subscripts "in-plane" and "out-of-plane" are used to denote collections of the in-plane and out-of-plane parts of these strain vectors. The transformation of natural strain components to Cartesian strain components in local coordinates in given by

$$\mathbf{e}^{\mathrm{C}}(\xi, \eta, \zeta) = T^{\mathrm{nC}}(\xi, \eta, \zeta)\mathbf{e}^{\mathrm{n}}(\xi, \eta, \zeta) \tag{3.6}$$

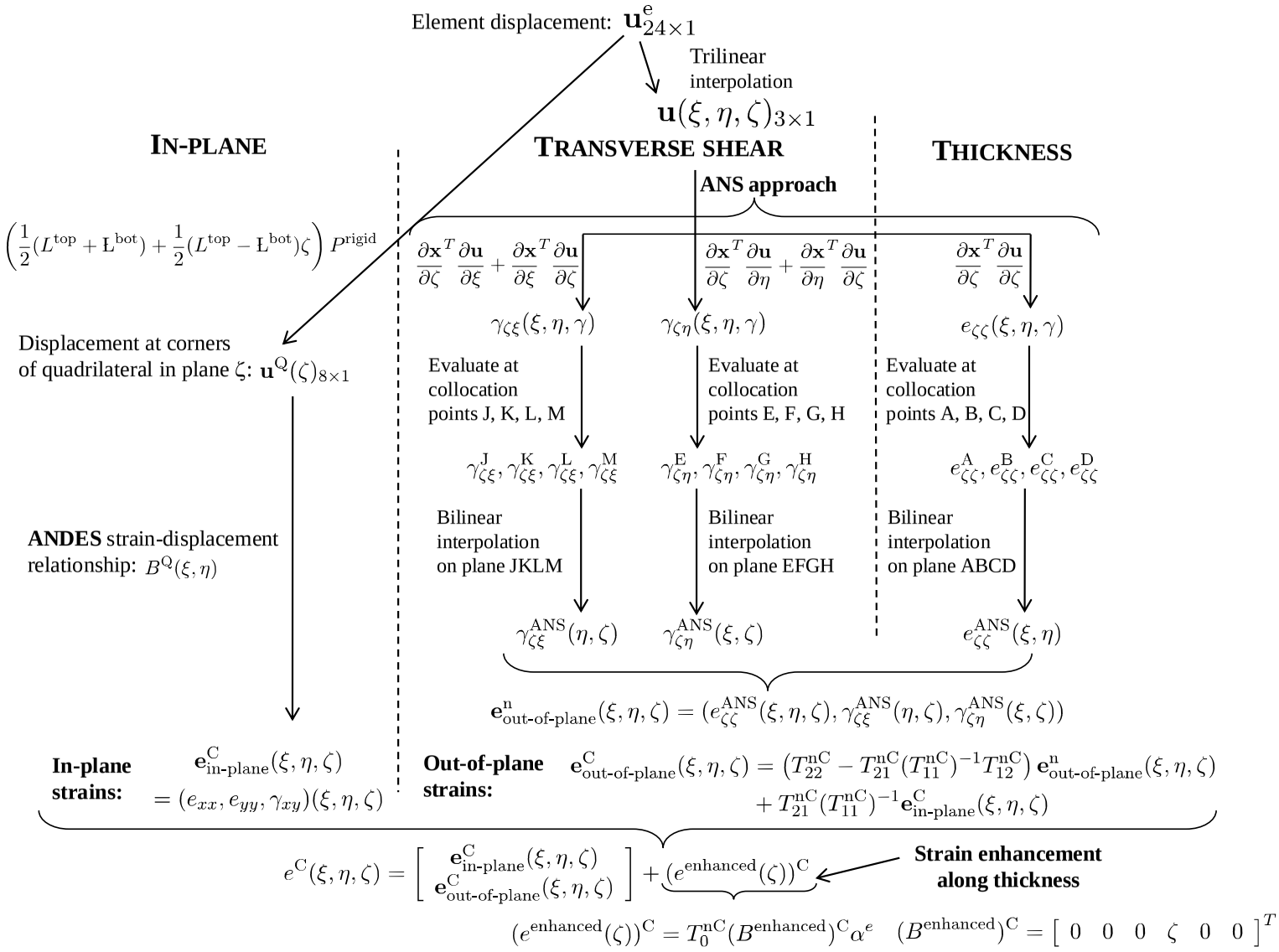

Figure 3.3: Derivation of assumed-strain field

where

$$T^{\mathrm{nC}} = \left[\begin{array}{ccc|ccc} j_{11}^2 & j_{21}^2 & j_{11}j_{21} & j_{31}^2 & j_{21}j_{31} & j_{11}j_{31} \\ j_{12}^2 & j_{22}^2 & j_{12}j_{22} & j_{32}^2 & j_{22}j_{32} & j_{12}j_{32} \\ 2j_{11}j_{12} & 2j_{21}j_{22} & j_{12}j_{21}+j_{11}j_{22} & 2j_{31}j_{32} & j_{22}j_{31}+j_{21}j_{32} & j_{12}j_{31}+j_{11}j_{32} \\ \hline j_{13}^2 & j_{23}^2 & j_{13}j_{23} & j_{33}^2 & j_{23}j_{33} & j_{13}j_{33} \\ 2j_{12}j_{13} & 2j_{22}j_{23} & j_{13}j_{22}+j_{12}j_{23} & 2j_{32}j_{33} & j_{23}j_{32}+j_{22}j_{33} & j_{13}j_{32}+j_{12}j_{33} \\ 2j_{11}j_{13} & 2j_{21}j_{23} & j_{13}j_{21}+j_{11}j_{23} & 2j_{31}j_{33} & j_{23}j_{31}+j_{21}j_{33} & j_{13}j_{31}+j_{11}j_{33} \end{array}\right] \tag{3.7}$$

with $j_{pq}, p, q = 1, \ldots, 3$ being the components of the inverse of the jacobian matrix (3.5). This can also be written in a partitioned format as

$$\begin{pmatrix} \mathbf{e}^{\mathrm{C}}_{\text{in-plane}} \\ \mathbf{e}^{\mathrm{C}}_{\text{out-of-plane}} \end{pmatrix} = \begin{bmatrix} T^{\mathrm{nC}}_{11} & T^{\mathrm{nC}}_{12} \\ T^{\mathrm{nC}}_{21} & T^{\mathrm{nC}}_{22} \end{bmatrix} \begin{pmatrix} \mathbf{e}^{\mathrm{n}}_{\text{in-plane}} \\ \mathbf{e}^{\mathrm{n}}_{\text{out-of-plane}} \end{pmatrix} \tag{3.8}$$

3.2.2.1 In-plane strains

The in-plane strain field is constructed by applying the ANDES formulation of section 2.2 to each quadrilateral cross-section of the solid-shell element in the thickness direction. When applied to highly warped elements, this is found to result in non-zero in-plane Cartesian strains for rigid body displacements of the element, i.e. rigid body motions produce nonzero in-plane strains. To avoid this problem, rigid body components are projected out of the displacement vector using a projection matrix P^{rigid}, before applying the strain-displacement operator. The approach is similar to that used by Rankin and Nour-Omid Rankin and Nour-omid in [113, 100]. The x and y components of the displacement at the

corners of a quadrilateral are then approximated by[2]

$$\mathbf{u}^{\mathrm{Q}}(\zeta) = \frac{1}{2}(1+\zeta)L^{\mathrm{top}}P^{\mathrm{rigid}}\mathbf{u}^{\mathrm{e}} + \frac{1}{2}(1-\zeta)L^{\mathrm{bot}}P^{\mathrm{rigid}}\mathbf{u}^{\mathrm{e}}$$

with

$$P^{\mathrm{rigid}} = \mathbf{I} - \mathbf{\Lambda}\left(\mathbf{\Lambda}^{\mathbf{T}}\mathbf{\Lambda}\right)^{-1}\mathbf{\Lambda}$$

and

$$\mathbf{\Lambda} = \begin{bmatrix} 1 & 0 & 0 & \dots & 1 & 0 & 0 \\ 0 & 1 & 0 & \dots & 0 & 1 & 0 \\ 0 & 0 & 1 & \dots & 0 & 0 & 1 \\ y_1 & -x_1 & 0 & \dots & y_8 & -x_8 & 0 \\ 0 & z_1 & -y_1 & \dots & 0 & z_8 & -y_8 \\ -z_1 & 0 & x_1 & \dots & -z_8 & 0 & x_8 \end{bmatrix} \tag{3.9}$$

where L^{top} and L^{bot} are matrices consisting of ones and zeros that extract the x and y displacement components of nodes (1, 2, 3, 4) and nodes (5, 6, 7, 8) respectively and $\mathbf{\Lambda}$ is the matrix containing the first six columns of **GRC** introduced by Bergan in [28, 31]. Applying the strain-displacement operator from equation (2.10) gives the in-plane strain field and the corresponding strain-displacement operator.

$$\begin{aligned} \mathbf{e}^{\mathrm{C}}_{\text{in-plane}}(\xi,\eta,\zeta) &= B^{\mathrm{Q}}(\xi,\eta)\mathbf{u}^{\mathrm{Q}}(\zeta) \\ &= \underbrace{B^{\mathrm{Q}}(\xi,\eta)\frac{1}{2}(L^{\mathrm{top}}+L^{\mathrm{bot}})P^{\mathrm{rigid}}\mathbf{u}^{\mathrm{e}}}_{\text{membrane}} + \underbrace{B^{\mathrm{Q}}(\xi,\eta)\frac{1}{2}(L^{\mathrm{top}}-L^{\mathrm{bot}})\zeta P^{\mathrm{rigid}}\mathbf{u}^{\mathrm{e}}}_{\text{bending}} \\ &= B^{\mathrm{C}}_{\text{in-plane}}(\xi,\eta,\zeta)\mathbf{u}^{\mathrm{e}} \end{aligned} \tag{3.10}$$

The in-plane strain field thus consists of membrane and bending parts, the former being constant and the latter varying linearly over the element thickness.

[2] $\mathbf{u}^{\mathrm{Q}}(\zeta)$ is an exception to the general vector notation used in this work. It denotes the collection of x and y components of the displacements at the corners of the quadrilateral cross-section of constant natural coordinate ζ

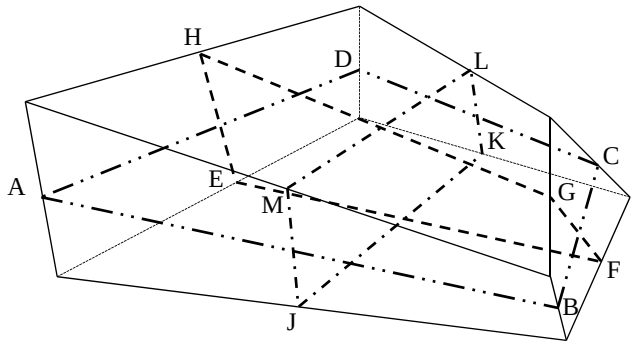

Figure 3.4: Collocation points of the ANS approach

3.2.2.2 Transverse shear strains

Transverse shear strains are approximated using the Assumed Natural Strain (ANS) concept. Compatible natural strain components corresponding to transverse shear are obtained as

$$\begin{aligned}\gamma_{\xi\zeta}(\xi,\eta,\zeta) &= \left(\frac{\partial \mathbf{x}}{\partial \zeta}\right)^T \left(\frac{\partial \mathbf{u}}{\partial \xi}\right) + \left(\frac{\partial \mathbf{x}}{\partial \xi}\right)^T \left(\frac{\partial \mathbf{u}}{\partial \zeta}\right) \\ \gamma_{\eta\zeta}(\xi,\eta,\zeta) &= \left(\frac{\partial \mathbf{x}}{\partial \zeta}\right)^T \left(\frac{\partial \mathbf{u}}{\partial \eta}\right) + \left(\frac{\partial \mathbf{x}}{\partial \eta}\right)^T \left(\frac{\partial \mathbf{u}}{\partial \zeta}\right)\end{aligned} \tag{3.11}$$

Each of these strain components is evaluated at four collocation points (shown in Figure 3.4), and the four values are interpolated bilinearly to obtain the assumed-strain field. The assumed transverse shear strain field is thus given by

$$\begin{aligned}\gamma_{\eta\zeta}^{\text{ANS}} &= \sum_{i=\text{E}}^{\text{H}} N^i_{\gamma_{\eta\zeta}}(\xi,\zeta)\gamma_{\eta\zeta}(\xi^i,\zeta^i), \quad N^i_{\gamma_{\eta\zeta}}(\xi,\zeta) = \frac{1}{4}(1+\xi^i\xi)(1+\zeta^i\zeta), \quad i = \text{E},\ldots,\text{H} \\ \gamma_{\xi\zeta}^{\text{ANS}} &= \sum_{i=\text{J}}^{\text{M}} N^i_{\gamma_{\xi\zeta}}(\eta,\zeta)\gamma_{\xi\zeta}(\eta^i,\zeta^i), \quad N^i_{\gamma_{\xi\zeta}}(\eta,\zeta) = \frac{1}{4}(1+\eta^i\eta)(1+\zeta^i\zeta), \quad i = \text{J},\ldots,\text{M}\end{aligned} \tag{3.12}$$

Cardoso et. al. [41] have shown that this approach to constructing the transverse shear strain field is effective in alleviating transverse shear locking in the element behavior. In full-integration solid-shell elements, many authors have used only two collocation points per transverse shear term (for example, [147, 55, 70]). However, it is found that such an element is still susceptible to curvature locking in the presence of inextensional bending. Furthermore, in reduced-integration elements, the use of two collocation points leads to a rank deficient stiffness matrix [41, 119].

3.2.2.3 Thickness strain

The thickness strain field is constructed by a combination of the ANS approach and strain enhancement. These are discussed in order.

The ANS approach for the thickness strain field follows along the same lines as for transverse shear strains. First the natural strain component corresponding to the thickness direction is obtained using

$$e_{\zeta\zeta}(\xi,\eta,\zeta) = \left(\frac{\partial \mathbf{x}}{\partial \zeta}\right)^T \left(\frac{\partial \mathbf{u}}{\partial \zeta}\right) \tag{3.13}$$

This is evaluated at the collocation points (A, B, C, D) shown in Figure 3.4 and interpolated bilinearly.

$$e^{\text{ANS}}_{\zeta\zeta}(\xi,\eta) = \sum_{i=\text{A}}^{\text{A}} N^i_{e_{\zeta\zeta}}(\xi,\eta)\gamma_{\eta\zeta}(\xi^i,\eta^i), \quad N^i_{e_{\zeta\zeta}}(\xi,\eta) = \frac{1}{4}(1+\xi^i\xi)(1+\eta^i\eta), \quad i = \text{A},\ldots,\text{D} \tag{3.14}$$

It has been shown by Schwarze et. al. [119], as well as can be seen from the the numerical solutions in this work (6) involving curved shells, that for thickness tapered elements, this assumed strain is a good remedy to alleviate thickness curvature locking.

Cartesian strain components: It is recognized that equation (3.10) gives Cartesian components of in-plane strains while equations (3.11) and (3.13) give natural components of out-of-plane strains. The Cartesian components of the out-of-plane strains are obtained using equation (3.8) as follows.

$$\begin{aligned}\mathbf{e}^{\text{C}}_{\text{out-of-plane}}(\xi,\eta,\zeta) = \left(T^{\text{nC}}_{22} - T^{\text{nC}}_{21}(T^{\text{nC}}_{11})^{-1}T^{\text{nC}}_{12}\right)\mathbf{e}^{\text{n}}_{\text{out-of-plane}}(\xi,\eta,\zeta) \\ +T^{\text{nC}}_{21}(T^{\text{nC}}_{11})^{-1}\mathbf{e}^{\text{C}}_{\text{in-plane}}(\xi,\eta,\zeta)\end{aligned} \tag{3.15}$$

which in turn can be written as

$$\mathbf{e}^{\text{C}}_{\text{out-of-plane}}(\xi,\eta,\zeta) = B^{\text{C}}_{\text{out-of-plane}}(\xi,\eta,\zeta)\mathbf{u}^{\text{e}} \tag{3.16}$$

Thus the strain-displacement matrix for the element is

$$(B^{ANS}(\xi,\eta,\zeta))^C = \left[\begin{array}{c} B^{\text{C}}_{\text{in-plane}}(\xi,\eta,\zeta) \\ \hline B^{\text{C}}_{\text{out-of-plane}}(\xi,\eta,\zeta) \end{array}\right] \tag{3.17}$$

where $B(\xi,\eta,\zeta)^{ANS}$ is a 6×24 matrix.

Strain enhancement: The assumed natural thickness strain $e^{\mathrm{ANS}}_{\zeta\zeta}$ is independent of ζ. This causes thickness locking, particularly in thick elements. In order to mitigate thickness locking, motivated by the fact that Poisson's effect would cause the thickness strain accompanying bending to vary linearly, the assumed natural strain is enhanced by the following thickness-dependent component.

$$(e^{\mathrm{enhanced}}_{\zeta\zeta}(\zeta))^n = \alpha^{\mathrm{e}}\zeta \tag{3.18}$$

where α^{e} is an element degree-of-freedom resulting from the enhancement of the strain field. Thus the total strain field for the element is given by

$$\begin{gathered} e^C_{elem} = \left[\begin{array}{cc} (B^{ANS}(\xi,\eta,\zeta))^C & (B^{\mathrm{enhanced}}(\zeta))^C \end{array}\right] \left(\begin{array}{c} \mathbf{u}^e \\ \alpha^e \end{array}\right) = \mathbf{B}_{elem} \left(\begin{array}{c} \mathbf{u}^e \\ \alpha^e \end{array}\right) \\ \text{with} \quad (B^{\mathrm{enhanced}}(\zeta))^C = T_0^{nC}(B^{\mathrm{enhanced}}(\zeta))^n \\ \text{and} \quad (B^{\mathrm{enhanced}}(\zeta))^n = \left[\begin{array}{cccccc} 0 & 0 & 0 & \zeta & 0 & 0 \end{array}\right]^T \end{gathered} \tag{3.19}$$

where the last column of $\mathbf{B}_{elem}$, which is a 6×25 matrix, corresponds to the enhanced-strain degree-of-freedom in the thickness direction. T_0^{nC} is the transformation matrix (3.7) evaluated at $\xi=\eta=\zeta=0$. It is noted that the enhanced strain is constant in the shell plane. The element stiffness matrix in local coordinates, K_{l}, is obtained by computing $\int_V \mathbf{B}^T_{elem} E \mathbf{B}_{elem} dV$ and eliminating the enhanced-strain degree-of-freedom by static condensation. This can be transformed to the representation in global coordinates in the usual manner.

3.3 Geometric nonlinear formulation using corotational kinematics

3.3.1 Kinematic description

In this section, the solid-shell element formulation is extended to the geometric nonlinear regime using a corotational kinematic description. The corotational description is based on decomposing the motion of an element into rigid body and deformation components.

Deformations are described with reference to a coordinate frame that translates and rotates with the element as shown in Figure 3.5. An attractive feature of the corotational description is that, elements that perform well in geometrically linear problems can be extended to nonlinear problems in an **element independent** fashion. This approach, referred to as an Element-Independent Corotational formulation (EICR), was introduced by Rankine and Brogan [112]. Felippa and Haugen [57, 68] present a unified formulation of the corotational approach for 3D elements with both translational and rotational degrees of freedom. In the current work, this unified formulation is adopted, and proofs of some results are presented in greater detail.

For a given deformed configuration, i.e., node positions with respect to the global frame, there are a number of strategies for constructing a corotated reference frame. In the formulation presented here, the origin of the corotational frame, C, is established by simply averaging the positions of the element nodes. The orientation R of the corotational frame depends on the positions of the nodes $\mathbf{X}^{\mathrm{e}}$. The specific construction of $R(\mathbf{X}^{\mathrm{e}})$ used in this work is described in section 3.3.2. In the remainder of this section, some generic relationships are derived assuming only the following invariance properties of $R(\mathbf{X}^{\mathrm{e}})$.

(1) *Rotation invariance*: If all the nodes are subject to a rigid-body rotation Q, then the resulting corotated frame is also rotated by Q.

$$R(\mathrm{diag}(Q)\mathbf{X}^{\mathrm{e}}) = QR(\mathbf{X}^{\mathrm{e}}) \text{ for any rotation matrix } Q \tag{3.20}$$

(2) *Translation invariance*: A uniform translation of all the nodes by $\mathbf{v}$ does not alter the orientation of the corotated frame.

$$R(\mathbf{X}^{\mathrm{e}} + \mathrm{stack}(\mathbf{v})) = R(\mathbf{X}^{\mathrm{e}}) \text{ for any 3-vector } \mathbf{v} \tag{3.21}$$

From Figure 3.5, it can be deduced that for node A,

$$R(\mathbf{X}^{\mathrm{e}}(t))(\mathbf{x}^{\mathrm{A}} + \mathbf{u}_{\mathrm{d}}^{\mathrm{A}}(t)) = \mathbf{X}^{\mathrm{A}}(t) - \mathbf{X}^{\mathrm{C}}(t)$$

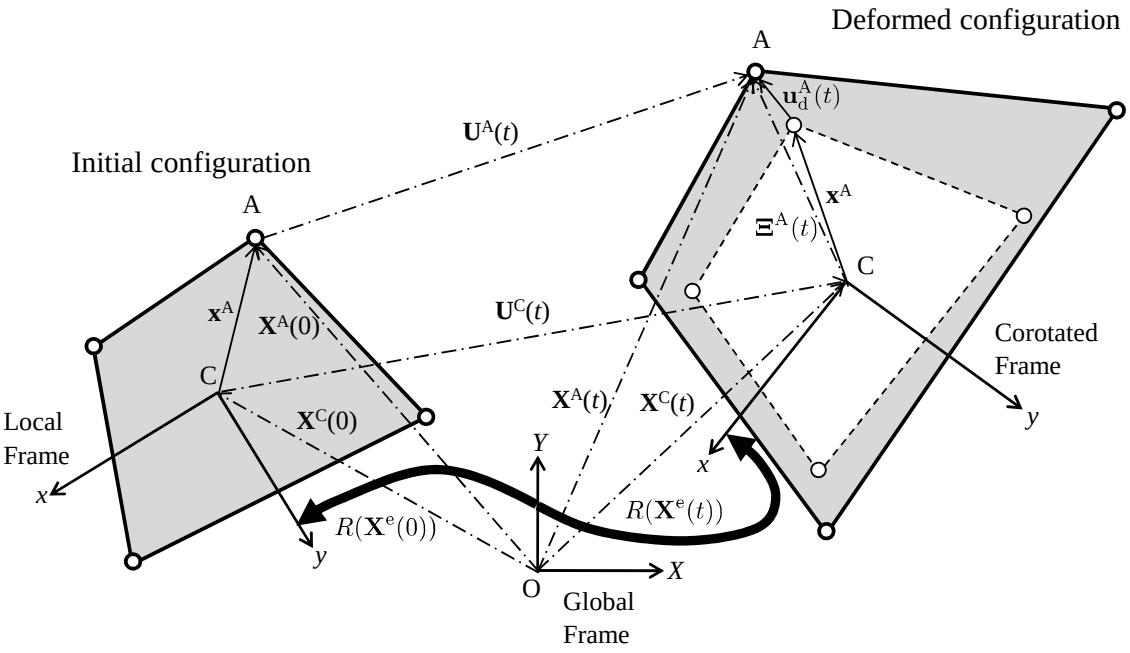

Figure 3.5: Corotational element kinematics highlighting the motion of a point A. For clarity, a two dimensional setting is shown the figure. $\mathbf{X}^{\mathrm{C}}$ is the average of the positions of the element nodes. Vectors represented by components in a local frame ($\mathbf{x}^{\mathrm{A}}$ and $\mathbf{u}_{\mathrm{d}}^{\mathrm{A}}$) are shown in solid arrows, and those represented by components in the global frame by dash-dot arrows. It can be seen that $\boldsymbol{\Xi}^{\mathrm{A}}(t) = \mathbf{X}^{\mathrm{A}}(t) - \mathbf{X}^{\mathrm{C}}(t) = R(\mathbf{X}^{\mathrm{e}}(t))(\mathbf{x}^{\mathrm{A}} + \mathbf{u}_{\mathrm{d}}^{\mathrm{A}}(t))$.

or rewriting,

$$\mathbf{u}_{\mathrm{d}}^{\mathrm{A}}(t) = R(\mathbf{X}^{\mathrm{e}}(t))^T(\mathbf{X}^{\mathrm{A}}(t) - \mathbf{X}^{\mathrm{C}}(t)) - R(\mathbf{X}^{\mathrm{e}}(0))^T(\mathbf{X}^{\mathrm{A}}(0) - \mathbf{X}^{\mathrm{C}}(0))$$

This can be collected for all the nodes of the element, giving the element deformational displacement

$$\mathbf{u}_{\mathrm{d}}^{\mathrm{e}}(t) = \mathcal{R}(\mathbf{X}^{\mathrm{e}}(t))^T(\mathbf{X}^{\mathrm{e}}(t) - \mathrm{stack}(\mathbf{X}^{\mathrm{C}}(t))) - \mathcal{R}(\mathbf{X}^{\mathrm{e}}(0))^T(\mathbf{X}^{\mathrm{e}}(0) - \mathrm{stack}(\mathbf{X}^{\mathrm{C}}(0))) \tag{3.22}$$

where $\mathcal{R} = \mathrm{diag}(R)$. Further, defining $P_T = \frac{1}{n^{\mathrm{e}}}\,\mathrm{array}(I_{3\times 3})$, $\mathrm{stack}(\mathbf{X}^{\mathrm{C}})$ can be written as $\mathrm{stack}(\mathbf{X}^{\mathrm{C}}) = P_T\mathbf{X}^{\mathrm{e}}$, Defining $\mathbf{\Xi}^{\mathrm{e}} = (I - P_T)\mathbf{X}^{\mathrm{e}}$ and using the translation invariance property (3.21) of R, equation (3.22) becomes

$$\mathbf{u}_{\mathrm{d}}^{\mathrm{e}}(t) = \mathcal{R}(\mathbf{\Xi}^{\mathrm{e}}(t))^T\mathbf{\Xi}^{\mathrm{e}}(t) - \mathcal{R}(\mathbf{\Xi}^{\mathrm{e}}(0))^T\mathbf{\Xi}^{\mathrm{e}}(0) \tag{3.23}$$

To obtain a relationship between change in displacement and change in deformational displacement, equation (3.23) is differentiated with respect to time.

$$\dot{\mathbf{u}}_{\mathrm{d}}^{\mathrm{e}} = \mathcal{R}(\mathbf{\Xi}^{\mathrm{e}}(t))^T\dot{\mathbf{\Xi}}^{\mathrm{e}} + (D\mathcal{R}(\mathbf{\Xi}^{\mathrm{e}}(t))\dot{\mathbf{\Xi}}^{\mathrm{e}}e)^T\mathbf{\Xi}^{\mathrm{e}}(t) \tag{3.24}$$

where D denotes the derivative. It follows from the fact that $R(\mathbf{\Xi}^{\mathrm{e}}(t))R(\mathbf{\Xi}^{\mathrm{e}}e(t))^T = I$ for all t, that $(DR(\mathbf{\Xi}^{\mathrm{e}}(t))\dot{\mathbf{\Xi}}^{\mathrm{e}})R(\mathbf{\Xi}^{\mathrm{e}}(t))^T$ is a skew-symmetric matrix. Furthermore, $(DR(\mathbf{\Xi}^{\mathrm{e}}(t))\dot{\mathbf{\Xi}}^{\mathrm{e}})R(\mathbf{\Xi}^{\mathrm{e}}(t))^T$ is linear in $\dot{\mathbf{\Xi}}^{\mathrm{e}}$. Consequently, this term can be written as

$$(DR(\mathbf{\Xi}^{\mathrm{e}}(t))\dot{\mathbf{\Xi}}^{\mathrm{e}})R(\mathbf{\Xi}^{\mathrm{e}}(t))^T = \mathrm{spin}(G(\mathbf{\Xi}^{\mathrm{e}}e(t))\dot{\mathbf{\Xi}}^{\mathrm{e}}) \tag{3.25}$$

where

$$\mathrm{spin}(\mathbf{v}) = \begin{bmatrix} 0 & -v_3 & v_2 \\ v_3 & 0 & -v_1 \\ -v_2 & v_1 & 0 \end{bmatrix}$$

It is also noted that $\mathrm{spin}(\mathbf{v})\mathbf{u} = \mathbf{v}\times\mathbf{u}$. The matrix $G(\mathbf{\Xi}^{\mathrm{e}})$ can be interpreted as the operation of extracting the spatial angular velocity from an instantaneous motion starting from the configuration $\mathbf{\Xi}^{\mathrm{e}}$.

Using (3.25), equation (3.24) can be written as

$$\dot{\mathbf{u}}^{\mathrm{e}}_{\mathrm{d}} = \mathcal{R}(\boldsymbol{\Xi}^{\mathrm{e}}(t))^T\dot{\boldsymbol{\Xi}}^{\mathrm{e}} - \mathcal{R}(\boldsymbol{\Xi}^{\mathrm{e}}(t))^T \operatorname{diag}(\operatorname{spin}(G(\boldsymbol{\Xi}^{\mathrm{e}}(t))\dot{\boldsymbol{\Xi}}^{\mathrm{e}}))\boldsymbol{\Xi}^{\mathrm{e}}(t) \tag{3.26}$$

Moreover corresponding to a node n,

$$\operatorname{spin}(G(\boldsymbol{\Xi}^{\mathrm{e}}(t))\dot{\boldsymbol{\Xi}}^{\mathrm{e}})\boldsymbol{\Xi}^{n}(t) = (G(\boldsymbol{\Xi}^{\mathrm{e}}(t))\dot{\boldsymbol{\Xi}}^{\mathrm{e}}) \times \boldsymbol{\Xi}^{n}(t)$$

$$= -\boldsymbol{\Xi}^{n}(t) \times (G(\boldsymbol{\Xi}^{\mathrm{e}}(t))\dot{\boldsymbol{\Xi}}^{\mathrm{e}}) = -\operatorname{spin}(\boldsymbol{\Xi}^{n}(t))G(\boldsymbol{\Xi}^{\mathrm{e}}(t))\dot{\boldsymbol{\Xi}}^{\mathrm{e}}$$

Therefore, setting

$$S(\boldsymbol{\Xi}^{\mathrm{e}}) = \left[-\operatorname{spin}(\boldsymbol{\Xi}^{1})^T, -\operatorname{spin}(\boldsymbol{\Xi}^{2})^T, \ldots, -\operatorname{spin}(\boldsymbol{\Xi}^{n^{\mathrm{e}}})^T\right]^T$$

and

$$P_R(\boldsymbol{\Xi}^{\mathrm{e}}) = S(\boldsymbol{\Xi}^{\mathrm{e}})G(\boldsymbol{\Xi}^{\mathrm{e}})$$

and using the fact that $\dot{\boldsymbol{\Xi}}^{\mathrm{e}} = (I - P_T)\dot{\mathbf{U}}^{\mathrm{e}}$, equation (3.26) can be written as

$$\dot{\mathbf{u}}^{\mathrm{e}}_{\mathrm{d}} = \mathcal{R}(\boldsymbol{\Xi}^{\mathrm{e}}(t))^T(I - P_R(\boldsymbol{\Xi}^{\mathrm{e}}(t)))(I - P_T)\dot{\mathbf{U}}^{\mathrm{e}} \tag{3.27}$$

In the following, some results concerning the matrices P_T and $P_R(\boldsymbol{\Xi}^{\mathrm{e}})$ are derived.

(i) *P_T is a projector*: It can be verified by direct calculation that $P_T^2 = P_T$. Thus P_T is a projector.

(ii) *$P_R(\mathbf{X}^e)$ is a projector*: $P_R(\boldsymbol{\Xi}^{\mathrm{e}})^2 = S(\boldsymbol{\Xi}^{\mathrm{e}})G(\boldsymbol{\Xi}^{\mathrm{e}})S(\boldsymbol{\Xi}^{\mathrm{e}})G(\boldsymbol{\Xi}^{\mathrm{e}})$. To show that $P_R(\boldsymbol{\Xi}^{\mathrm{e}})$ is a projector, it is sufficient to show that $G(\boldsymbol{\Xi}^{\mathrm{e}})S(\boldsymbol{\Xi}^{\mathrm{e}}) = I$, or equivalently that $G(\boldsymbol{\Xi}^{\mathrm{e}})S(\boldsymbol{\Xi}^{\mathrm{e}})\boldsymbol{\omega} = \boldsymbol{\omega}$ for any $\boldsymbol{\omega}$.

$S(\boldsymbol{\Xi}^{\mathrm{e}})\boldsymbol{\omega} = \operatorname{diag}(\operatorname{spin}(\boldsymbol{\omega}))\boldsymbol{\Xi}^{\mathrm{e}}$. Therefore, $S(\boldsymbol{\Xi}^{\mathrm{e}})\boldsymbol{\omega}$ is the velocity of the nodes when the element is subject to a rigid-body rotation with spatial angular velocity $\boldsymbol{\omega}$. From the interpretation of $G(\boldsymbol{\Xi}^{\mathrm{e}})$ as the operation of extracting the angular velocity, it can be conjectured that $G(\boldsymbol{\Xi}^{\mathrm{e}})S(\boldsymbol{\Xi}^{\mathrm{e}})\boldsymbol{\omega} = \boldsymbol{\omega}$. However, a formal proof is as follows.

Let $\tilde{\boldsymbol{\Xi}}^{\mathrm{e}}(\tau)$ represent the position relative to $\mathbf{X}^{\mathrm{C}}$ at time τ of the n^{e} nodes of the element, starting at $\tilde{\boldsymbol{\Xi}}^{\mathrm{e}}(0) = \boldsymbol{\Xi}^{\mathrm{e}}$ and undergoing rigid-body rotation about $\mathbf{X}^{\mathrm{C}}$ with constant angular velocity $\boldsymbol{\omega}$. The motion is described by the differential equation

$$\dot{\tilde{\boldsymbol{\Xi}}}^{\mathrm{e}}(\tau) = \mathrm{diag}(\mathrm{spin}(\boldsymbol{\omega}))\tilde{\boldsymbol{\Xi}}^{\mathrm{e}}(\tau) \tag{3.28}$$

The solution of this differential equation is $\tilde{\boldsymbol{\Xi}}^{\mathrm{e}}(\tau) = \mathrm{diag}(\bar{Q}(\tau))\tilde{\boldsymbol{\Xi}}^{\mathrm{e}}(0)$ where $\bar{Q}(\tau)$ and is a rotation matrix given by $\bar{Q}(\tau) = \exp(\mathrm{spin}(\boldsymbol{\omega})\tau)$, exp being the matrix exponential. $\bar{Q}$ satisfies $\dot{\bar{Q}}(\tau)\bar{Q}(\tau)^T = \mathrm{spin}(\boldsymbol{\omega})$ for all τ. Then:

$$\begin{aligned}
&\mathrm{spin}(G(\tilde{\boldsymbol{\Xi}}^{\mathrm{e}}(\tau))S(\tilde{\boldsymbol{\Xi}}^{\mathrm{e}}(\tau))\boldsymbol{\omega}) \\
=&(D\hat{R}(\tilde{\boldsymbol{\Xi}}^{\mathrm{e}}(\tau))S(\tilde{\boldsymbol{\Xi}}^{\mathrm{e}}(\tau))\boldsymbol{\omega})\hat{R}(\tilde{\boldsymbol{\Xi}}^{\mathrm{e}}(\tau)) \text{ by the definition of } G, \text{ equation (3.25)} \\
=&(D\hat{R}(\tilde{\boldsymbol{\Xi}}^{\mathrm{e}}(\tau))\,\mathrm{diag}(\mathrm{spin}(\boldsymbol{\omega}))\tilde{\boldsymbol{\Xi}}^{\mathrm{e}}(\tau))\hat{R}(\tilde{\boldsymbol{\Xi}}^{\mathrm{e}}(\tau)) \\
=&(D\hat{R}(\tilde{\boldsymbol{\Xi}}^{\mathrm{e}}(\tau))\dot{\tilde{\boldsymbol{\Xi}}}^{\mathrm{e}})\hat{R}(\tilde{\boldsymbol{\Xi}}^{\mathrm{e}}(\tau)) \text{ by equation (3.28)} \\
=&\left(\frac{d}{dt}\hat{R}(\tilde{\boldsymbol{\Xi}}^{\mathrm{e}}(\tau))\right)\hat{R}(\tilde{\boldsymbol{\Xi}}^{\mathrm{e}}(\tau))^T \\
=&\left(\frac{d}{dt}\hat{R}(\mathrm{diag}(\bar{Q}(\tau))\tilde{\boldsymbol{\Xi}}^{\mathrm{e}}(0))\right)\hat{R}(\mathrm{diag}(\bar{Q}(\tau))\tilde{\boldsymbol{\Xi}}^{\mathrm{e}}(0))^T \\
=&\left(\frac{d}{dt}\bar{Q}(\tau)\hat{R}(\tilde{\boldsymbol{\Xi}}^{\mathrm{e}}(0))\right)\left(\bar{Q}(\tau)\hat{R}(\tilde{\boldsymbol{\Xi}}^{\mathrm{e}}(0))\right)^T \text{ by the rotation invariance property (3.20)} \\
=&\dot{\bar{Q}}(\tau)\hat{R}(\tilde{\boldsymbol{\Xi}}^{\mathrm{e}}(0))\hat{R}(\tilde{\boldsymbol{\Xi}}^{\mathrm{e}}(0))^T\bar{Q}(\tau)^T \\
=&\dot{\bar{Q}}(\tau)\bar{Q}(\tau)^T \\
=&\,\mathrm{spin}(\boldsymbol{\omega})
\end{aligned}$$

Thus $G(\tilde{\boldsymbol{\Xi}}^{\mathrm{e}}(\tau))S(\tilde{\boldsymbol{\Xi}}^{\mathrm{e}}(\tau))\boldsymbol{\omega} = \boldsymbol{\omega}$ for all τ, in particular for $\tau = 0$. Hence $G(\boldsymbol{\Xi}^{\mathrm{e}})S(\boldsymbol{\Xi}^{\mathrm{e}})\boldsymbol{\omega} = \boldsymbol{\omega}$, and $P_R(\boldsymbol{\Xi}^{\mathrm{e}})$ is a projector.

(iii) *The product* $P_T P_R(\boldsymbol{\Xi}^e) = 0$: It can be verified by direct calculation that $P_T S(\boldsymbol{\Xi}^{\mathrm{e}}) = 0$. Thus $P_T P_R(\boldsymbol{\Xi}^{\mathrm{e}}) = P_T S(\boldsymbol{\Xi}^{\mathrm{e}})G(\boldsymbol{\Xi}^{\mathrm{e}}) = 0$.

(iv) *The product* $P_R(\boldsymbol{\Xi}^e)P_T = 0$: Each column of P_T is of the form $\mathrm{stack}(\mathbf{v})$ for $\mathbf{v} = (1,0,0)^T,\ (0,1,0)^T,\ (0,0,1)^T$. Therefore to show that $P_R(\boldsymbol{\Xi}^{\mathrm{e}})P_T = 0$, it is sufficient to

show that $G(\boldsymbol{\Xi}^{\mathrm{e}})\,\mathrm{stack}(\mathbf{v}) = 0$ for any $\mathbf{v}$.

$\mathrm{stack}(\mathbf{v})$ is the velocity of the nodes when the element is subject to a uniform rigid-body motion with velocity $\mathbf{v}$. Again from the interpretation of $G(\boldsymbol{\Xi}^{\mathrm{e}})$ as extracting the angular velocity, it can be supposed that $G(\boldsymbol{\Xi}^{\mathrm{e}})\,\mathrm{stack}(\mathbf{v}) = 0$. The following is the complete proof.

Let $\tilde{\boldsymbol{\Xi}}^{\mathrm{e}}(\tau)$ represent the position relative to $\mathbf{X}^{\mathrm{C}}$ at time τ of the n^{e} nodes of the element, starting at $\tilde{\boldsymbol{\Xi}}^{\mathrm{e}}(0) = \boldsymbol{\Xi}^{\mathrm{e}}$ and undergoing rigid-body motion with constant velocity $\mathbf{v}$. Then $\tilde{\boldsymbol{\Xi}}^{\mathrm{e}}(\tau) = \boldsymbol{\Xi}^{\mathrm{e}} + \mathrm{stack}(\mathbf{v})\tau$.

$$
\begin{aligned}
& G(\tilde{\boldsymbol{\Xi}}^{\mathrm{e}}(t))\,\mathrm{stack}(\mathbf{v}) \\
=& (D\hat{R}(\tilde{\boldsymbol{\Xi}}^{\mathrm{e}}(\tau))\,\mathrm{stack}(\mathbf{v}))\hat{R}(\tilde{\boldsymbol{\Xi}}^{\mathrm{e}}(\tau)) \text{ by the definition of } G, \text{ equation (3.25)} \\
=& (D\hat{R}(\tilde{\boldsymbol{\Xi}}^{\mathrm{e}}(\tau))\dot{\tilde{\boldsymbol{\Xi}}}^{\mathrm{e}})\hat{R}(\tilde{\boldsymbol{\Xi}}^{\mathrm{e}}(\tau)) \\
=& \left(\frac{d}{dt}\hat{R}(\tilde{\boldsymbol{\Xi}}^{\mathrm{e}}(\tau))\right)\hat{R}(\tilde{\boldsymbol{\Xi}}^{\mathrm{e}}(\tau))^{T} \\
=& \left(\frac{d}{dt}\hat{R}(\boldsymbol{\Xi}^{\mathrm{e}})\right)\hat{R}(\boldsymbol{\Xi}^{\mathrm{e}})^{T} \text{by the translation invariance property (3.21)} \\
=& 0
\end{aligned}
$$

Using property (iv), equation (3.27) can be written as

$$\dot{\mathbf{u}}^{\mathrm{e}}_{\mathrm{d}} = \mathcal{R}(\boldsymbol{\Xi}^{\mathrm{e}}(t))^{T}(I - P_T - P_R(\boldsymbol{\Xi}^{\mathrm{e}}(t)))\dot{\mathbf{U}}^{\mathrm{e}}$$

or defining $\mathcal{P}(\boldsymbol{\Xi}^{\mathrm{e}}) = I - P_T - P_R(\boldsymbol{\Xi}^{\mathrm{e}})$ as

$$\dot{\mathbf{u}}^{\mathrm{e}}_{\mathrm{d}} = \mathcal{R}(\boldsymbol{\Xi}^{\mathrm{e}}(t))^{T}\mathcal{P}(\boldsymbol{\Xi}^{\mathrm{e}}(t))\dot{\mathbf{U}}^{\mathrm{e}} \tag{3.29}$$

Furthermore, it can be checked using properties (i)–(iv) that $\mathcal{P}(\boldsymbol{\Xi}^{\mathrm{e}})^2 = \mathcal{P}(\boldsymbol{\Xi}^{\mathrm{e}})$, i.e., that $\mathcal{P}(\boldsymbol{\Xi}^{\mathrm{e}})$ is a projector. It can be seen in equation (3.29) that the corotated deformational velocity $\dot{\mathbf{u}}^{\mathrm{e}}_{\mathrm{d}}$ is obtained from the global velocity vector $\dot{\mathbf{U}}^{\mathrm{e}}$ by a project-and-rotate operation, first a projection $\mathcal{P}(\boldsymbol{\Xi}^{\mathrm{e}})$, and then a rotation $\mathcal{R}(\boldsymbol{\Xi}^{\mathrm{e}})^{T}$. Alternatively, a rotate-and-project approach is also possible [68]. Next, the specific strategy used in this work to construct the

corotated frame orientation, $R(\boldsymbol{\Xi}^{\mathrm{e}})$ is described.

It is noted that the kinematic description explained in chapter 2 is a special case for the 3D version. The major difference is that in 2D case, the rotation matrix R is parameterized by a scalar θ, which is the angle between the global and corotated frame. In 2D case, the spatial angular velocity ω, which is a psuedo-vector, is simplified to the derivative of scalar θ and as it is shown in Equation (2.14), $\dot{\theta}$ has a closed form.

3.3.2 Construction of the corotated frame

Different methods have been proposed in the literature for constructing the corotated frame R for quadrilateral shell elements (see for example [112, 101, 68]). Veubeke defined the orientation by minimizing the mean square of relative displacements [60]. Belytschko and Bindeman [27] and Moita and Crisfield [99] obtained it by computing the polar decomposition of the deformation gradient tensor at the element centroid. This approach was also followed by Farid-Combescure in the context of a solid-shell element in their recent paper [3].

In the present work, the corotated frame is constructed in the same manner as the local frame in section 3.2.1.1, however current coordinates $\boldsymbol{\Xi}^{\mathrm{e}}(t)$ are used in equation (3.1).

The partial derivatives $\frac{\partial}{\partial \boldsymbol{\Xi}^{\mathrm{e}}_j} R(\boldsymbol{\Xi}^{\mathrm{e}})$ can be obtained from equation (3.1) by noting that

$$D||\mathbf{v}|| = \frac{1}{||\mathbf{v}||}\mathbf{v}^T$$

for $\mathbf{v} \neq 0$, and using the chain rule. Then from equation (3.25), it follows that the j^{th} column of the matrix $G(\boldsymbol{\Xi}^{\mathrm{e}})$ is given by

$$\text{axial}\left(\left(\frac{\partial}{\partial \boldsymbol{\Xi}^{\mathrm{e}}_j} R(\boldsymbol{\Xi}^{\mathrm{e}})\right) R(\boldsymbol{\Xi}^{\mathrm{e}})^T\right) \tag{3.30}$$

3.3.3 Tangent stiffness matrix

The internal force vector with components referred to the global and local coordinate systems respectively is given by

$$\begin{aligned} \mathbf{f}^{\mathrm{e}} &= K_{\mathrm{l}}\mathbf{u}_{\mathrm{d}}^{\mathrm{e}} \\ \mathbf{F}^{\mathrm{e}} &= \mathcal{P}(\boldsymbol{\Xi}^{\mathrm{e}})^T\mathcal{R}(\boldsymbol{\Xi}^{\mathrm{e}})\mathbf{f}^{\mathrm{e}} \end{aligned} \tag{3.31}$$

The tangent stiffness matrix needed for Newton's method can be obtained by considering the rate of change of the internal force vector.

$$\begin{aligned} \dot{\mathbf{F}}^{\mathrm{e}} = &\mathcal{P}(\boldsymbol{\Xi}^{\mathrm{e}})^T\mathcal{R}(\boldsymbol{\Xi}^{\mathrm{e}})\dot{\mathbf{f}}^{\mathrm{e}} \\ &+ (I - P_T)^T\frac{d}{dt}\mathcal{R}(\boldsymbol{\Xi}^{\mathrm{e}})\mathbf{f}^{\mathrm{e}} - G(\boldsymbol{\Xi}^{\mathrm{e}})^T\frac{d}{dt}S(\boldsymbol{\Xi}^{\mathrm{e}})^T\mathcal{R}(\boldsymbol{\Xi}^{\mathrm{e}})\mathbf{f}^{\mathrm{e}} \\ &- G(\boldsymbol{\Xi}^{\mathrm{e}})^T S(\boldsymbol{\Xi}^{\mathrm{e}})^T\frac{d}{dt}\mathcal{R}(\boldsymbol{\Xi}^{\mathrm{e}})\mathbf{f}^{\mathrm{e}} \\ &- \frac{d}{dt}G(\boldsymbol{\Xi}^{\mathrm{e}})^T S(\boldsymbol{\Xi}^{\mathrm{e}})^T\mathcal{R}(\boldsymbol{\Xi}^{\mathrm{e}})\mathbf{f}^{\mathrm{e}} \end{aligned} \tag{3.32}$$

Each of these terms is considered in order. The first term,

$$\begin{aligned} &\mathcal{P}(\boldsymbol{\Xi}^{\mathrm{e}})^T\mathcal{R}(\boldsymbol{\Xi}^{\mathrm{e}})\dot{\mathbf{f}}^{\mathrm{e}} \\ =&\mathcal{P}(\boldsymbol{\Xi}^{\mathrm{e}})^T\mathcal{R}(\boldsymbol{\Xi}^{\mathrm{e}})K_{\mathrm{l}}\dot{\mathbf{u}}_{\mathrm{d}}^{\mathrm{e}} \\ =&\mathcal{P}(\boldsymbol{\Xi}^{\mathrm{e}})^T\mathcal{R}(\boldsymbol{\Xi}^{\mathrm{e}})K_{\mathrm{l}}\dot{\mathbf{u}}_{\mathrm{d}}^{\mathrm{e}}\mathcal{R}(\boldsymbol{\Xi}^{\mathrm{e}})^T\mathcal{P}(\boldsymbol{\Xi}^{\mathrm{e}})\dot{\mathbf{U}}^{\mathrm{e}} \\ =&K_{\mathrm{M}}\dot{\mathbf{U}}^{\mathrm{e}} \end{aligned}$$

gives rise to the "material" stiffness matrix K_{M}. The second and third terms combine as follows.

$$\begin{aligned}
&(I-P_T)^T\frac{d}{dt}\mathcal{R}(\boldsymbol{\Xi}^{\mathrm{e}})\mathbf{f}^{\mathrm{e}} - G(\boldsymbol{\Xi}^{\mathrm{e}})^T\frac{d}{dt}S(\boldsymbol{\Xi}^{\mathrm{e}})^T\mathcal{R}(\boldsymbol{\Xi}^{\mathrm{e}})\mathbf{f}^{\mathrm{e}}\\
=&(I-P_T)^T(D\mathcal{R}(\boldsymbol{\Xi}^{\mathrm{e}})\dot{\boldsymbol{\Xi}}^{\mathrm{e}})\mathcal{R}(\boldsymbol{\Xi}^{\mathrm{e}})^T\mathcal{R}(\boldsymbol{\Xi}^{\mathrm{e}})\mathbf{f}^{\mathrm{e}} - G(\boldsymbol{\Xi}^{\mathrm{e}})^TS(\dot{\boldsymbol{\Xi}}^{\mathrm{e}})^T\mathcal{R}(\boldsymbol{\Xi}^{\mathrm{e}})\mathbf{f}^{\mathrm{e}}\\
=&(I-P_T)^T\operatorname{diag}(\operatorname{spin}(G(\boldsymbol{\Xi}^{\mathrm{e}})\dot{\boldsymbol{\Xi}}^{\mathrm{e}}))\mathcal{R}(\boldsymbol{\Xi}^{\mathrm{e}})\mathbf{f}^{\mathrm{e}} - G(\boldsymbol{\Xi}^{\mathrm{e}})^TS(\dot{\boldsymbol{\Xi}}^{\mathrm{e}})^T\mathcal{R}(\boldsymbol{\Xi}^{\mathrm{e}})\mathbf{f}^{\mathrm{e}}\\
=&(I-P_T)^TS(\mathcal{R}(\boldsymbol{\Xi}^{\mathrm{e}})\mathbf{f}^{\mathrm{e}})G(\boldsymbol{\Xi}^{\mathrm{e}})\dot{\boldsymbol{\Xi}}^{\mathrm{e}} + G(\boldsymbol{\Xi}^{\mathrm{e}})^TS(\mathcal{R}(\boldsymbol{\Xi}^{\mathrm{e}})\mathbf{f}^{\mathrm{e}})^T\dot{\boldsymbol{\Xi}}^{\mathrm{e}}\\
=&(I-P_T)^TS(\mathcal{R}(\boldsymbol{\Xi}^{\mathrm{e}})\mathbf{f}^{\mathrm{e}})G(\boldsymbol{\Xi}^{\mathrm{e}})(I-P_T)\dot{\mathbf{U}}^{\mathrm{e}} + G(\boldsymbol{\Xi}^{\mathrm{e}})^TS(\mathcal{R}(\boldsymbol{\Xi}^{\mathrm{e}})\mathbf{f}^{\mathrm{e}})^T(I-P_T)\dot{\mathbf{U}}^{\mathrm{e}}\\
=&\left(S(\mathcal{R}(\boldsymbol{\Xi}^{\mathrm{e}})\mathbf{f}^{\mathrm{e}})G(\boldsymbol{\Xi}^{\mathrm{e}}) + (S(\mathcal{R}(\boldsymbol{\Xi}^{\mathrm{e}})\mathbf{f}^{\mathrm{e}})G(\boldsymbol{\Xi}^{\mathrm{e}}))^T\right)\dot{\mathbf{U}}^{\mathrm{e}} \quad \text{(from results (iii) and (iv) above)}\\
=&K_{\mathrm{G}}^{\mathrm{I}}\dot{\mathbf{U}}^{\mathrm{e}}
\end{aligned}$$

$K_{\mathrm{G}}^{\mathrm{I}}$ is one part of the geometric stiffness matrix. Clearly, $K_{\mathrm{G}}^{\mathrm{I}}$ is symmetric.

In considering the last two terms of (3.32), the arguments developed by Nour-Omid and Rankin [100] are used. For any 3-vectors $\mathbf{u}$ and $\mathbf{v}$, and rotation matrix R, it can be verified by direct calculation that

$$\begin{aligned}
\operatorname{spin}(R\mathbf{u}) &= R\operatorname{spin}(\mathbf{u})R^T\\
\mathbf{u}\times(R\mathbf{v}) &= R\left((R^T\mathbf{u})\times\mathbf{v}\right)
\end{aligned} \tag{3.33}$$

and[3]

$$\operatorname{spin}(\mathbf{u})\operatorname{spin}(\mathbf{v}) - \operatorname{spin}(\mathbf{v})\operatorname{spin}(\mathbf{u}) = \operatorname{spin}(\mathbf{u}\times\mathbf{v}) \tag{3.34}$$

Furthermore, for moment-equilibrium of an element (expressed in local coordinates),

$$\begin{aligned}
&0\\
=&\sum_{n=1}^{n^{\mathrm{e}}}(R(\boldsymbol{\Xi}^{\mathrm{e}})^T\boldsymbol{\Xi}^n)\times\mathbf{f}^n\\
=&R(\boldsymbol{\Xi}^{\mathrm{e}})^T\sum_{n=1}^{n^{\mathrm{e}}}\boldsymbol{\Xi}^n\times(R(\boldsymbol{\Xi}^{\mathrm{e}})\mathbf{f}^n)\\
=&R(\boldsymbol{\Xi}^{\mathrm{e}})^TS(\boldsymbol{\Xi}^{\mathrm{e}})^T\mathcal{R}(\boldsymbol{\Xi}^{\mathrm{e}})\mathbf{f}^{\mathrm{e}}
\end{aligned} \tag{3.35}$$

Thus it can also be concluded that $S(\boldsymbol{\Xi}^{\mathrm{e}})^T\mathcal{R}(\boldsymbol{\Xi}^{\mathrm{e}})\mathbf{f}^{\mathrm{e}} = 0$.

[3] for result (3.34), it is helpful to use index notation and the alternating tensor-kronecker delta identity

Now considering the fourth term of (3.32),

$$
\begin{aligned}
&- G(\boldsymbol{\Xi}^{\mathrm{e}})^T S(\boldsymbol{\Xi}^{\mathrm{e}})^T \frac{d}{dt}\mathcal{R}(\boldsymbol{\Xi}^{\mathrm{e}})\mathbf{f}^{\mathrm{e}} \\
=&- G(\boldsymbol{\Xi}^{\mathrm{e}})^T S(\boldsymbol{\Xi}^{\mathrm{e}})^T (D\mathcal{R}(\boldsymbol{\Xi}^{\mathrm{e}})\dot{\boldsymbol{\Xi}}^{\mathrm{e}})\mathcal{R}(\boldsymbol{\Xi}^{\mathrm{e}})^T\mathcal{R}(\boldsymbol{\Xi}^{\mathrm{e}})\mathbf{f}^{\mathrm{e}} \\
=&- G(\boldsymbol{\Xi}^{\mathrm{e}})^T S(\boldsymbol{\Xi}^{\mathrm{e}})^T \operatorname{diag}(\operatorname{spin}(G(\boldsymbol{\Xi}^{\mathrm{e}})\dot{\boldsymbol{\Xi}}^{\mathrm{e}}))\mathcal{R}(\boldsymbol{\Xi}^{\mathrm{e}})\mathbf{f}^{\mathrm{e}} \\
=&- G(\boldsymbol{\Xi}^{\mathrm{e}})^T S(\boldsymbol{\Xi}^{\mathrm{e}})^T S(\mathcal{R}(\boldsymbol{\Xi}^{\mathrm{e}})\mathbf{f}^{\mathrm{e}})G(\boldsymbol{\Xi}^{\mathrm{e}})\dot{\boldsymbol{\Xi}}^{\mathrm{e}} \\
=&- G(\boldsymbol{\Xi}^{\mathrm{e}})^T S(\boldsymbol{\Xi}^{\mathrm{e}})^T S(\mathcal{R}(\boldsymbol{\Xi}^{\mathrm{e}})\mathbf{f}^{\mathrm{e}})G(\boldsymbol{\Xi}^{\mathrm{e}})\dot{\mathbf{U}}^{\mathrm{e}} \\
=&K_{\mathrm{G}}^{\mathrm{II}}\dot{\mathbf{U}}^{\mathrm{e}}
\end{aligned}
$$

where $K_{\mathrm{G}}^{\mathrm{II}}$ is the second part of the stiffness matrix. While it is not immediately apparent that $K_{\mathrm{G}}^{\mathrm{II}}$ is symmetric, this fact can be concluded by verifying that the antisymmetric part of $K_{\mathrm{G}}^{\mathrm{II}}$ is zero at equilibrium.

$$
\begin{aligned}
&S(\boldsymbol{\Xi}^{\mathrm{e}})^T S(\mathcal{R}(\boldsymbol{\Xi}^{\mathrm{e}})\mathbf{f}^{\mathrm{e}}) - S(\mathcal{R}(\boldsymbol{\Xi}^{\mathrm{e}})\mathbf{f}^{\mathrm{e}})^T S(\boldsymbol{\Xi}^{\mathrm{e}}) \\
=&\sum_{n=1}^{n^{\mathrm{e}}} \operatorname{spin}(R(\boldsymbol{\Xi}^{\mathrm{e}})\mathbf{f}^n)\operatorname{spin}(\boldsymbol{\Xi}^n) - \operatorname{spin}(\boldsymbol{\Xi}^n)\operatorname{spin}(R(\boldsymbol{\Xi}^{\mathrm{e}})\mathbf{f}^n) \\
=&\sum_{n=1}^{n^{\mathrm{e}}} \operatorname{spin}\left((R(\boldsymbol{\Xi}^{\mathrm{e}})\mathbf{f}^n)\times\boldsymbol{\Xi}^n\right) \\
=&-\sum_{n=1}^{n^{\mathrm{e}}} \operatorname{spin}\left(R(\boldsymbol{\Xi}^{\mathrm{e}})\left((R(\boldsymbol{\Xi}^{\mathrm{e}})^T\boldsymbol{\Xi}^n)\times\mathbf{f}^n\right)\right) \\
=&-R(\boldsymbol{\Xi}^{\mathrm{e}})\left(\sum_{n=1}^{n^{\mathrm{e}}}(R(\boldsymbol{\Xi}^{\mathrm{e}})^T\boldsymbol{\Xi}^n)\times\mathbf{f}^n\right)R(\boldsymbol{\Xi}^{\mathrm{e}})^T \\
=&0
\end{aligned}
$$

By virtue of the fact that $S(\boldsymbol{\Xi}^{\mathrm{e}})^T\mathcal{R}(\boldsymbol{\Xi}^{\mathrm{e}})\mathbf{f}^{\mathrm{e}} = 0$ at equilibrium, the fifth term in (3.32) is also zero.

Thus the tangent stiffness matrix is given by $K = K_{\mathrm{M}} + K_{\mathrm{G}}^{\mathrm{I}} + K_{\mathrm{G}}^{\mathrm{II}}$, and is symmetric at equilibrium. It is noteworthy that following references [99, 100], the computation of the second derivative of $R(\boldsymbol{\Xi}^{\mathrm{e}})$ does not become necessary.

Chapter 4

Solid-shell element based on ANS and EAS concepts

4.1 Introduction

In this chapter, an eight-node solid-shell element based on ANS and EAS approaches is presented. ANS concept is implemented to account for the transverse shear and thickness strains, which has proven to circumvent the curvature thickness and transverse shear locking problems. EAS approach based on the Hu-washizu variational principle with six EAS degrees-of-freedom is applied. Five extra degrees-of-freedom are applied on the in-plane strains (e_{xx},e_{yy} and γ_{xy}) to improve the element response for in-plane loadings and one on the thickness strain so as to alleviate the Poisson's thickness locking. Following the work done in chapter 3, all nodal coordinates are transformed to a local coordinate to make the finite element independent of node numbering. Formulation yields exact solutions for both the membrane and bending patch tests. Following Schwarze's reduced-integration formulation in [119], in this chapter, a full-integration formulation is presented which has an improved response to in-plane loads.

4.2 Review of EAS concept

This concept was first introduced by Simo and Rifai [130]. The method is based on Hu-Washizu variational principle in terms of stress, displacement and enhanced strain fields. A review of this concept along with a comparison to ANDES scheme is presented below:

4.2.1 EAS weak form

The Tonti diagram shown in Figure 4.1, illustrates the weak form of the three-field variational principle.

The EAS formulation is described within the following steps:

(1) Writing the weak form using Figure 4.1 yields:

$$\begin{aligned}\int_V \left(e^{\mathbf{u}} - e\right) \delta\sigma dV + \int_V \left(\sigma^e - \sigma\right) \delta e dV + \int_{s_t} \left(\sigma.n - t^p\right) \delta\mathbf{u} dS \\ - \int_V \left(D^*\sigma + b\right) \delta\mathbf{u} dV + \int_{s_u} \left(\mathbf{u} - \mathbf{u}^p\right) n\delta\sigma dS = 0\end{aligned} \tag{4.1}$$

(2) Doing the integration by parts on the fourth term of (4.1) and doing some simplifications produces:

$$\begin{aligned}\delta\int_V \left[\sigma\left(e^{\mathbf{u}} - e\right)\right] dV + \delta\int_V \frac{1}{2} eEe dV - \delta\int_V \mathbf{u} b dV - \delta\int_{s_t} \mathbf{u} t^p dS \\ - \delta\int_{s_u} \left(\mathbf{u} - \mathbf{u}^p\right) \sigma.n dS = 0\end{aligned} \tag{4.2}$$

Assumed strain and stress fields: The Following relations exist for the assumed stress and strain fields:

$$\begin{aligned} e &= e^{\mathrm{C}} + (e^{\mathrm{enh}})^{\mathrm{C}} = B_{iso}\mathbf{u} + B^{\mathrm{enh}}\alpha \\ \sigma &= G_\sigma \Sigma \end{aligned} \tag{4.3}$$

where α is the vector of enhaced degrees-of-freedom, B_{iso} is obtained by taking the derivatives of the tri-linear shape functions with respect to the degrees-of-freedom and superscript $\square^{\mathrm{C}}$ denotes the Cartesian coordinates. B^{enh} is a matrix of prescribed functions with linearly independent columns, which define the enhanced strain interpolation, G_σ is a matrix of functions whose columns and rows are linearly independent and Σ is the vector of element stress parameters.

(3) Substituting (4.3) into (4.2) gives:

$$\begin{aligned}-\delta\int_V \sigma^T (e^{\mathrm{enh}})^{\mathrm{C}} dV + \delta\int_V \left(e^{\mathrm{C}} + (e^{\mathrm{enh}})^{\mathrm{C}}\right)^T E \left(e^{\mathrm{C}} + (e^{\mathrm{enh}})^{\mathrm{C}}\right) dV \\ - \delta\int_V u^T f dV = 0\end{aligned} \tag{4.4}$$

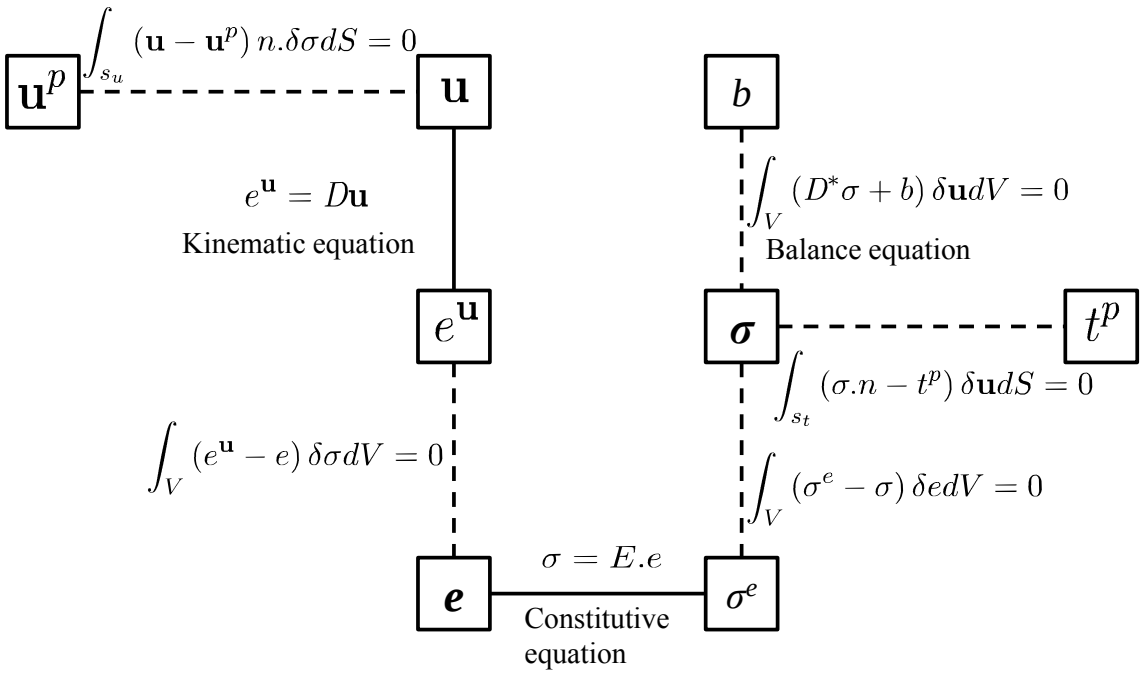

Figure 4.1: Tonti diagram representing the three-field variational principle that is the basis of the EAS approach. Solid lines represent relations that apply pointwise, and dashed lines those are enforced in weak form. D denotes the strain-displacement operator, and D^* its adjoint.

(4) Requiring that the first term of (4.4), and the sum of the second and third terms be separately zero yields the following equations.[1]

$$\begin{aligned} \delta \int_V \sigma^T (e^{\mathrm{enh}})^{\mathrm{C}} dV = 0 \\ \delta \int_V \left(e^{\mathrm{C}} + (e^{\mathrm{enh}})^{\mathrm{C}}\right)^T E \left(e^{\mathrm{C}} + (e^{\mathrm{enh}})^{\mathrm{C}}\right) dV - \delta \int_V \mathbf{u}^T f dV = 0 \end{aligned} \tag{4.5}$$

(5) substituting $e^{\mathrm{C}} = B_{iso}\mathbf{u}$ and $(e^{\mathrm{enh}})^{\mathrm{C}} = B^{\mathrm{enh}}\alpha$ in equation (4.5) gives:

$$\begin{aligned} &\begin{bmatrix} \int_V B_{iso}^T E B_{iso} dV & \int_V B_{iso}^T E B^{\mathrm{enh}} dV & 0 \\ \int_V B_{iso}^T E B^{\mathrm{enh}} dV & \int_V (B^{\mathrm{enh}})^T E B^{\mathrm{enh}} dV & 0 \\ \int_V (B^{\mathrm{enh}})^T E B_{iso} dV & \int_V (B^{\mathrm{enh}})^T E B^{\mathrm{enh}} dV & -\int_V (B^{\mathrm{enh}})^T G_\sigma dV \end{bmatrix} \begin{pmatrix} \mathbf{u} \\ \alpha \\ \Sigma \end{pmatrix} \\ &= \begin{bmatrix} K_{11} & K_{12} & 0 \\ K_{21} & K_{22} & 0 \\ K_{31} & K_{32} & K_{33} \end{bmatrix} \begin{pmatrix} \mathbf{u} \\ \alpha \\ \Sigma \end{pmatrix} = \begin{pmatrix} f \\ 0 \\ 0 \end{pmatrix} \end{aligned} \tag{4.6}$$

The third row of (4.6) comes from the the second term of equation (4.1) to recover the stress in EAS approach. After doing the static condensation, the followings are obtained:

$$\begin{aligned} \alpha &= K_{22}^{-1} K_{12}^T \mathbf{u} = T\mathbf{u} \\ K_{element} &= K_{11} - K_{12} K_{22}^{-1} K_{21} \end{aligned} \tag{4.7}$$

In order that the EAS element passes the Patch test, two conditions are required to be satisfied as follows:

condition 1: The enhanced strain interpolation and the standard strain interpolation must be independent.

condition 2: The assumed discrete stress field must include at least piece-wise constant functions after enforcing the orthogonality condition.

[1] The orthogonality of independent stress (σ) to the enhanced strain($(e^{\mathrm{enh}})^{\mathrm{C}}$) eliminates the stress field from the finite element equations.

4.2.2 Parallel between EAS and ANDES

The followings are analogous issues between ANDES and EAS element:

(1) In EAS approach, the independent stress should be orthogonal to the incompatible strains, while in ANDES, the strain-derived stress is orthogonal to the incompatible strain.

(2) In EAS the stress is a master field and the orthogonality condition eliminates the stress from the FEM calculations while in ANDES method, the stress is a slave variable which is derived from the independent strain through the constitutive relation.

(3) In EAS method, the requirement for passing the patch test is fulfilled by the two conditions mentioned in previous subsection,while in ANDES element, passing of the patch test requirement is guaranteed by decomposing the strains into basic and higher order modes and enforcing the energy orthogonality of the higher order terms to the basic ones.

4.3 Linear Element formulation

4.3.1 Global to local coordinates transformation (R)

In order to keep the finite element independent of the nodal numbering, all calculations will be done in the local frame. This process is done similar to 3.2.1.1.

4.3.2 Stiffness matrix computation

The derivation of the strain-displacement operator based on assumed-strain and EAS concepts is summarized in Figure 4.2. This is elaborated in the following. The Cartesian position vectors ($\mathbf{x}$) and displacement vectors ($\mathbf{u}$) are approximated using tri-linear shape functions. The natural (contravariant) base, descrbed in 3, is chosen to approximate the displacement and (covariant) compatible strains. The assumed natural out-of-plane strains are computed

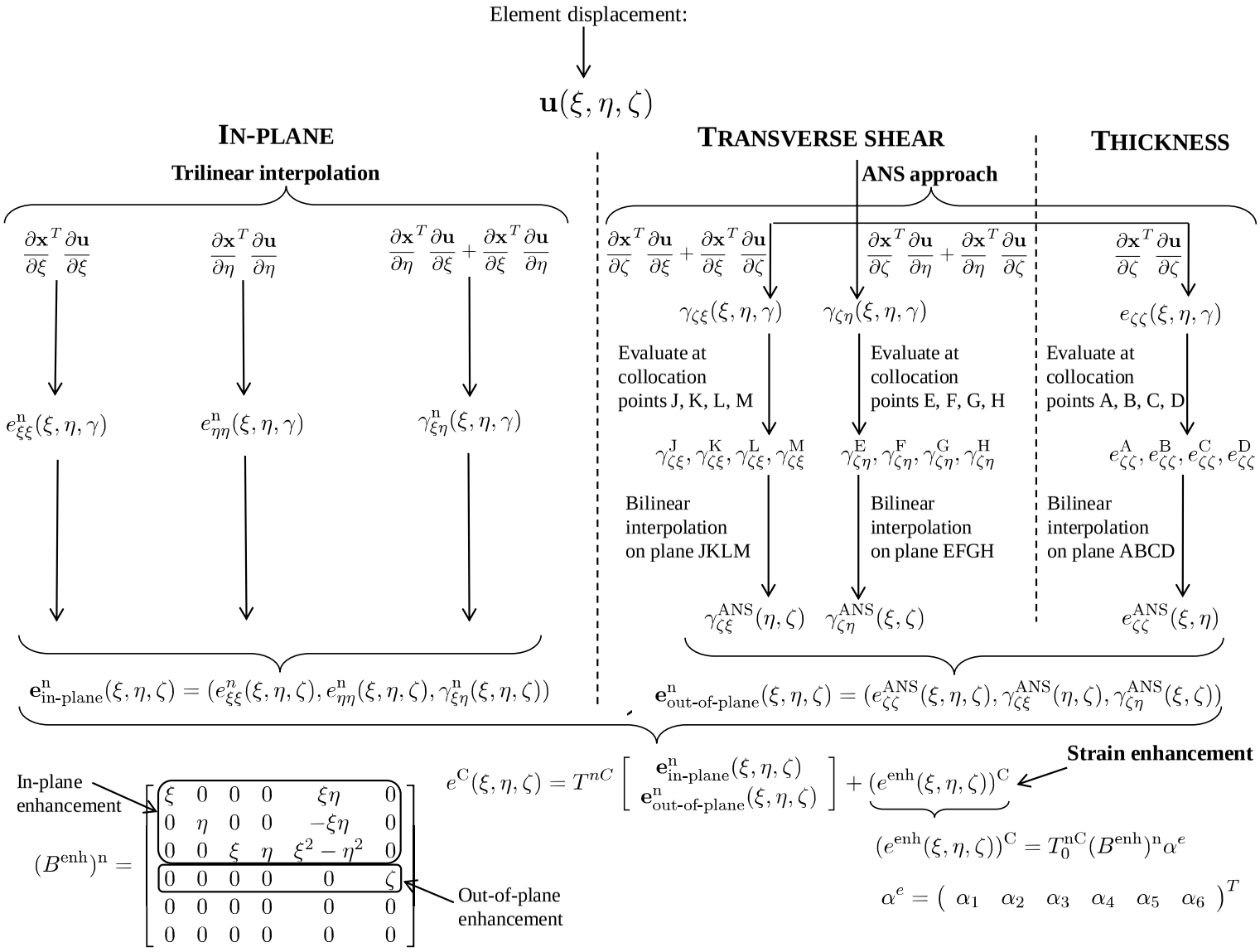

Figure 4.2: Derivation of strain-displacement operator based on assumed-strain and EAS approaches

similar to the approach explained in 3.2.2.2.

The natural in-plane strains are computed as follows:

$$\begin{aligned} e^{\mathrm{n}}_{\xi\xi}(\xi,\eta,\gamma) &= \frac{\partial \mathbf{x}}{\partial \xi}^T \frac{\partial \mathbf{u}}{\partial \xi} \\ e^{\mathrm{n}}_{\eta\eta}(\xi,\eta,\gamma) &= \frac{\partial \mathbf{x}}{\partial \eta}^T \frac{\partial \mathbf{u}}{\partial \eta} \\ \gamma^{\mathrm{n}}_{\xi\eta}(\xi,\eta,\gamma) &= \frac{\partial \mathbf{x}}{\partial \eta}^T \frac{\partial \mathbf{u}}{\partial \xi} + \frac{\partial \mathbf{x}}{\partial \xi}^T \frac{\partial \mathbf{u}}{\partial \eta} \end{aligned} \tag{4.8}$$

where the superscript $\square^{\mathrm{n}}$ corresponds to the natural coordinates.

Stacking up the natural in-plane strains (from Equation (4.8)) and natural out-of-plane strains (from 3.2.2.2), the strain-displacement relation for the element is obtained as follows:

$$(e^{ANS}(\xi,\eta,\zeta))^{\mathrm{C}} = T^{nC} \begin{bmatrix} \mathbf{e}^{\mathrm{n}}_{\text{in-plane}}(\xi,\eta,\zeta) \\ \mathbf{e}^{\mathrm{n}}_{\text{out-of-plane}}(\xi,\eta,\zeta) \end{bmatrix} = (B^{ANS}(\xi,\eta,\zeta))^{\mathrm{C}}\mathbf{u} \tag{4.9}$$

where T^{nC} is the transformation matrix defined in (3.7).

Strain enhancement: In order to alleviate the thickness locking, the assumed natural thickness strain $e^{\mathrm{ANS}}_{\zeta\zeta}$ is enhanced by one extra degree-of-freedom. Five extra degrees-of-freedom are used to the improve the in-plane response of the element. Thus the total strain

field for the element is given by

$$e^{\mathrm{C}}_{elem} = \left[\begin{array}{cc} (B^{ANS}(\xi,\eta,\zeta))^{\mathrm{C}} & (B^{\mathrm{enh}}(\zeta))^{\mathrm{C}} \end{array} \right] \left[\begin{array}{c} \mathbf{u}^e \\ \alpha^e \end{array} \right] = \mathbf{B}_{elem} \left[\begin{array}{c} \mathbf{u}^e \\ \alpha^e \end{array} \right]$$

$$\text{with} \quad (B^{\mathrm{enh}}(\xi,\eta,\zeta))^{\mathrm{C}} = T_0^{\mathrm{nC}} (B^{\mathrm{enh}}(\xi,\eta,\zeta))^n$$

$$\text{and} \quad (B^{\mathrm{enh}}(\xi,\eta,\zeta))^n = \left[\begin{array}{cccccc} \xi & 0 & 0 & 0 & \xi\eta & 0 \\ 0 & \eta & 0 & 0 & -\xi\eta & 0 \\ 0 & 0 & \xi & \eta & \xi^2 - \eta^2 & 0 \\ 0 & 0 & 0 & 0 & 0 & \zeta \\ 0 & 0 & 0 & 0 & 0 & 0 \\ 0 & 0 & 0 & 0 & 0 & 0 \end{array} \right] \tag{4.10}$$

where $\alpha^{(e)}$ is the vector containing the six extra degrees-of-freedom. The last six columns of $\mathbf{B}_{elem}$, which is a 6×31 matrix, corresponds to the enhanced-strain degrees-of-freedom. T_0^{nC} is the transformation matrix of Equation (3.7) evaluated at $\xi = \eta = \zeta = 0$. It is noted that the enhanced strain is constant in the shell plane.

The first three rows of $(B^{\mathrm{enh}}(\xi,\eta,\zeta))^n$, which correspond to the in-plane response, are picked from Simo's EAS qudrilateral element in [130]. Following Simo's work, the formulation is stable since the columns of $(B^{\mathrm{enh}}(\xi,\eta,\zeta))^n$ are linearly independent and the formulation passes the constant strain patch test since the following relation is satisfied:

$$\int_{\square} (B^{\mathrm{enh}}(\xi,\eta,\zeta))^n d\xi = 0 \tag{4.11}$$

Equation (4.11) guarantees that the subspace of approxiamtion contains piece-wise constant stress fields which insures the satisfaction of constant strain patch test [130].

The element stiffness matrix in local coordinates, K_{l}, is obtained by computing $\int_V \mathbf{B}^T_{elem} E \mathbf{B}_{elem} dV$ and eliminating the enhanced-strain degree-of-freedom by static condensation.

4.3.3 Local to Global stiffness matrix

In this part the local stiffness matrix ($\mathbf{K}_l$) is transformed to the global stiffness matrix by:

$$\mathbf{K}_G^e = R\mathbf{K}_l^e R^T \tag{4.12}$$

4.4 Conclusion

In this chapter, a solid-shell element based on ANS and EAS with six enahnaced degrees-of-freedom is presented. In order to circumvent the transverse shear locking and curvature locking in thickness direction, the ANS concept has been used.

EAS concept with six extra degrees-of-freedom has been used in the element; One to alleviate the Poisson's thickness locking problem and five to improve the in-plane response of the element.

In the numerical examples chapter, the linear element formulation has been assessed by a number of famous benchmarks, proposed for shell-like finite elements. The element passes both membrane and bending patch tests. Moreover, the element's performance has been tested for mesh distortion, warped mesh arrangement, single and doubly curved structures. The response of the element to various well-known benchmarks are compared to the ANDES solid-shell formulation explained in 3.

In summery, the numerical examples proved that the proposed solid-shell formulation has a satisfactory performance for shell problems including linear-elastic materials. In numerical examples chapter, only the linear elastic problems have been addressed.

The proposed element can be extended to address the geometric and material nonlinearities using any type of kinematic descriptions such as Total Lagrangian, Updated Lagrangian or Corotational kinematic.

Chapter 5

Nonlinear solution algorithm

5.1 Background

Haugen [68] has collected a detailed explanation of the solution algorithms in his thesis and this chapter is an excerpt of his report with some minor changes. The early solution algorithms for nonlinear problems were based on the purely incremental methods considering the load control. In those methods the disadvantage of drifting away from the equilibrium path (which is step-size dependent) requires a very fine step-size for accurate analysis.

Due to the mentioned shortcomings the development of incremental/iterative methods including equilibrium-correcting iterations came into the play. The corrector step has the advantage that the drift error is removed and the computed equilibrium path becomes independent of the increment step-size as long as the iterative step converges.

Geometrically non-linear structures usually undergo a maximum load level in which they are incapable of withstanding further load increases until an abrupt change in geometry occurs. A load control approach can detect a limit point but generally fails to traverse it. Traversal is desirable since it checks whether the structure has the load carrying capabilities after the localized instabilities [68].

Several methods for traversing the equilibrium path beyond limit points have been addressed in literature, such as the displacement control techniques first introduced by Argyris [10], the method of artificial springs [122] and the method based on controlling the load increment with the "current stiffness parameter" and suppressing iterations around limit points [30].

During the past three decades significant improvements have been made by allowing loads and displacements to be varied together in each increment. The most practically important examples of these methods are the arc-length methods originally proposed by Riks and Wempner [116] and later refined by many authors (as examples: Bathe et al [20, 16], Crisfield [48] and Riks [117]. Each of these algorithms are suitable for some specific problems. But in general, the arc-length type algorithms are most robust tools in terms of the variety of problems they can handle.

In this research, the Arc length method including the corrector step is used to solve the nonlinear problem. Orthogonal-trajectory method proposed by Fried [62] is used for the corrector phase.

5.2 Review of the Arc length algorithm

In arc length control method there are $N+1$ equations to be solved, N corresponding to the number of degrees-of-freedom and 1 related to the loading parameter λ. The augmented displacement vector is written as:

$$\Delta\tilde{\mathbf{u}} = \begin{bmatrix} \Delta\mathbf{u} \\ \Delta\lambda \end{bmatrix} \tag{5.1}$$

Δ accounts for the increments for the predictor step. The $(N+1)^{th}$ equation corresponds to the equation for the arc length [48].

For the corrector step the augmented displacement vector is as:

$$\delta\tilde{\mathbf{u}} = \begin{bmatrix} \delta\mathbf{u} \\ \delta\lambda \end{bmatrix} \tag{5.2}$$

where δ stands for the changes for the corrector phase.

5.2.1 Arc length algorithm

In order to avoid solving the $N+1$ simoultaneous equations, the algorithm summarized in Table 5.1 is used to solve the nonlinear problem [68].

where q is the incremental load vector, W_q is the incremental velocity, $r(\mathbf{U}, \lambda)$ is the force residual vector and K is the tangent stiffness matrix. It is noteworthy that since the solid-shell element carries only translational degrees-of-freedom the displacement vector is updated in an algebraic fashion.

Predictor phase with arc length Δs

Set $V_0 = K(\mathbf{U})^{-1} q(\lambda)$

For $n = 1$ *to number of increments*

Solve for W_q, $\quad W_q = K^{-1} q(\lambda)$

Set $\quad z = \sqrt{1 + W_q^T W_q}$

If $W_q^T V_0 > 0 \quad \Longrightarrow \quad \Delta\lambda = \frac{\Delta s}{z}$

Else $\quad \Longrightarrow \quad \Delta\lambda = -\frac{\Delta s}{z}$

Set $\quad V_0 = \Delta\lambda W_q$

Update $\quad \lambda = \lambda + \Delta\lambda \quad$ and $\quad \mathbf{U} = \mathbf{U} + \Delta\lambda W_q$

Corrector phase

For $i = 1$ *to max iteration number for correction*

Set $W_q = K(\mathbf{U})^{-1} q(\lambda)$

Set $W_r = -K(\mathbf{U})^{-1} r(\mathbf{U}, \lambda)$

Set $\delta\lambda = -\frac{W_q^T W_r}{1 + W_q^T W_q}$ (considering the orthogonal trajectory iterations [62])

Update $\quad \lambda = \lambda + \delta\lambda \quad$ and $\quad \mathbf{U} = \mathbf{U} + (W_r + \delta\lambda W_q)$

Until $\| r(\mathbf{U}, \lambda) \| < \epsilon$, $\quad$ where ϵ is the force residual convergence criterion

End

End

Table 5.1: Arc length algorithm

Chapter 6

Numerical examples

6.1 2D Quadrilateral element

In this subsection, seven numerical examples are presented. The first four examples illustrate the performance of the ANDES quadrilateral element in linear elastic problems. In the fifth example, the accuracy of the corotational kinematic description is shown using a model with linear elastic material behavior. Both elastoplastic (material nonlinear) and geometrically nonlinear behavior are considered in the sixth and seventh examples. For linear problems, results are compared with well-known benchmarks, and for nonlinear problems with solutions from ABAQUS [1]. In geometrically nonlinear problems, the ABAQUS solutions are based on the Total Lagrangian (TL) kinematic description.

6.1.1 Example 1: Constant strain patch test

The ANDES element is first evaluated in the context of a constant strain/stress patch test as shown in Fig 6.1. The material behavior is modeled as isotropic linear elastic with Young's modulus $E = 1000.0\text{N/mm}^2$ and Poisson's ratio $\nu = 0.25$ and the patch thickness is 1.0m. As can be seen in Table 6.1, the numerical results obtained using the ANDES element are in exact agreement with the analytical solutions, indicating that the element passes the patch test. Also shown in Table 6.1 are results obtained using three other elements: CPS4 (4-node isoparametric element of ABAQUS [1]), AGQ6-I and AGQ6-II (elements derived using quadrilateral area coordinate method [152]).

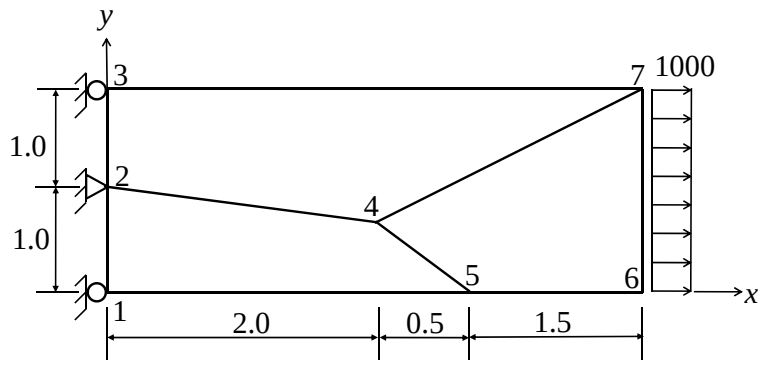

Figure 6.1: Example 1 — Patch test

Table 6.1: Example 1 — Patch test results for ANDES Quad element

DOFs	v_2	v_3	u_4	v_4	u_5	v_5	u_6	v_6	u_7	v_7
CPS4	-0.2500	-0.5000	2.0000	-0.1250	2.5000	0.0000	4.0000	0.0000	4.0000	-0.5000
AGQ6-I	-0.2787	-0.4291	2.0758	-0.4211	2.4946	-0.9491	5.4819	-0.8051	4.9589	-1.6375
AGQ6-II	-0.3010	-0.5017	1.7560	-0.8383	2.0800	-1.4505	5.0614	-2.1764	5.6885	-3.3179
ANDES	**-0.2500**	**-0.5000**	**2.0000**	**-0.1250**	**2.5000**	**0.0000**	**4.0000**	**0.0000**	**4.0000**	**-0.5000**
Exact	-0.2500	-0.5000	2.0000	-0.1250	2.5000	0.0000	4.0000	0.0000	4.0000	-0.5000

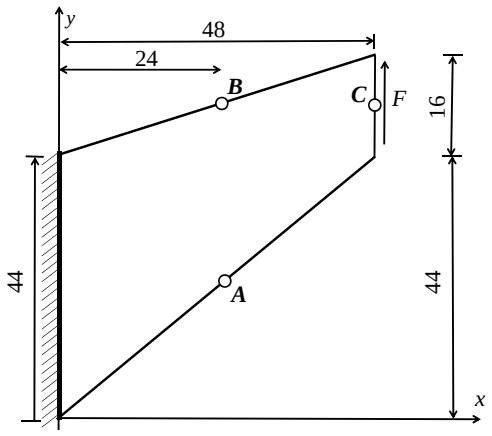

Figure 6.2: Example 2 — Cook's skew beam problem

The fact that the ANDES element passes the patch test comes as no surprise since this is set as **a priori** requirement in the construction of the element. We recall from chapter 2 that this is accomplished by decomposing the basic modes from higher order ones, and enforcing that the higher order modes be energy orthogonal to the basic modes. We also note that other elements such as AGQ6-I and AGQ6-II that have been shown to have good performance under distortion ([152], see also Example 3 below) do not pass the patch test.

6.1.2 Example 2: Cook's skew beam problem

In this example, convergence with mesh refinement is explored using a skew cantilever model proposed by Cook et. al. [45] (Figure 6.2). The material behavior is modeled as isotropic linear elastic with Young's modulus $E = 1.0$ and Poisson's ratio $\nu = 1/3$. The beam is fixed at the left end, and subjected to a shear force $F = 1/16$ distributed uniformly over the depth at the right end.

The computed vertical displacement of node C (v_{C}), the maximum principal stress at node A ($\sigma_{\mathrm{A,max}}$), and the minimum principal stress at point B ($\sigma_{\mathrm{B,min}}$) are listed in Table 6.2. In this table, the results obtained using the ANDES element are compared with those using other elements: CPS4 (4-node isoparametric element of ABAQUS [1]), P-S (hybrid element [109]), Q6 (4-node isoparametric element with internal parameters [151]), QE-2

Table 6.2: Example 2 — Convergence results for Cook's skew beam problem

	v_C				$\sigma_{A,max}$				$\sigma_{B,min}$			
Mesh size	2×2	4×4	8×8	16×16	2×2	4×4	8×8	16×16	2×2	4×4	8×8	16×16
CPS4	11.80	18.29	22.08	23.43	0.1217	0.1873	0.2242	0.2311	-0.0960	-0.1524	-0.1869	-0.1966
P-S	21.13	23.02	–	23.88	0.1854	0.2241	–	0.2364	–	–	–	–
Q6	22.94	23.48	23.80	23.91	0.2029	0.2258	0.2334	0.2361	-0.1734	-0.1915	-0.1997	-0.2028
QE-2	21.35	23.04	–	23.88	0.1956	0.2261	–	0.2364	–	–	–	–
$\bar{B}$-Q4E	21.35	23.04	–	23.88	0.1956	0.2261	–	0.2364	–	–	–	–
AGQ6-I	23.07	23.68	23.87	23.93	0.2023	0.2275	0.2351	0.2365	-0.1758	-0.1972	-0.2016	-0.2033
AGQ6-II	25.92	24.37	24.04	23.97	0.2169	0.2286	0.2352	0.2365	-0.1999	-0.2014	-0.2027	-0.2035
ANDES	**21.46**	**22.84**	**23.64**	**23.89**	**0.1866**	**0.2268**	**0.2366**	**0.2375**	**-0.1591**	**-0.1926**	**-0.2023**	**-0.2034**
Reference			23.94				0.2361				-0.2025	

(assumed strain element [111]), $\bar{B}$-Q4E (assumed strain element [111]), AGQ6-I and AGQ6-II (elements derived using quadrilateral area coordinate method [152]). A reference solution is also obtained using the CPS8 element of ABAQUS (higher order eight node quadrilateral element) using 64×64 mesh. The results show that the rate of convergence obtained using the ANDES element is comparable to other high-performance elements.

6.1.3 Example 3: Cantilever beam with imposed tip lateral displacement

A cantilever beam of length 10.0m, depth 0.5m and thickness 1m is considered. The material behavior is modeled as isotropic linear elastic with Young's modulus $E = 200,000\text{N/mm}^2$ and Poisson's ratio $\nu = 0.3$. A vertical displacement of 0.2m is imposed at the tip. Figures 6.4(a) and 6.4(b) show meshes with different element aspect ratios and extents of distortion. In Figure 6.4(c), the strain energies from the finite element solutions are compared with the strain energy from the analytical solution based on Euler-Bernoulli beam theory. The plot shows that the solutions obtained with the ANDES element converge quickly with mesh refinement, even with large aspect ratios and distortion. On the other hand, as is well known, the corresponding solutions obtained using the displacement-based CPS4 element converge much more slowly eventhough CPS4 is among those elements which pass the patch test. A result closer to the analytical solution may be obtained using the ANDES element with more elements in the depth direction.

Figure 6.3: Example 3 — Cantilever beam with imposed tip lateral displacement

(a) Mesh with high aspect ratio

(b) Randomly distorted mesh

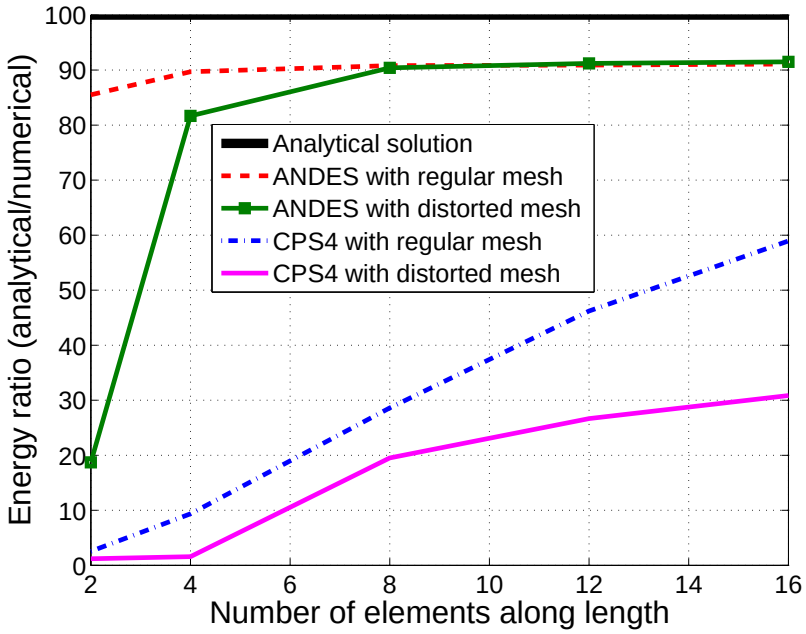

(c) EnergyRatio

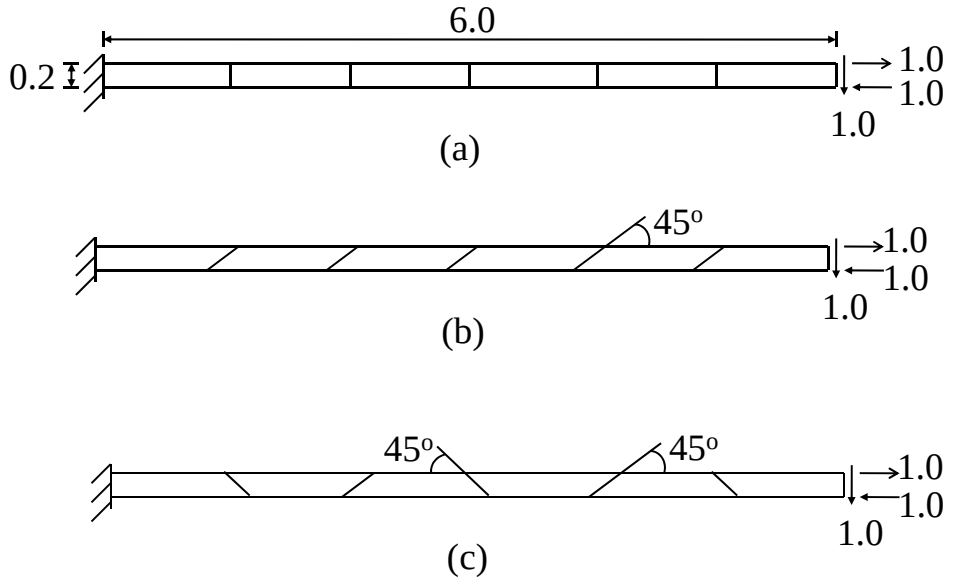

Figure 6.4: Example 4 — MacNeal's thin beam

6.1.4 Example 4: MacNeal's cantilever beam with distorted mesh

This example is a benchmark proposed by MacNeal and Harder [92] to check the sensitivity of the 4-node quadrilateral plane element to mesh distortion. As can be seen in Figure 6.4, three types of mesh arrangements are investigated: (a) rectangular elements with high aspect ratio, (b) elements with high aspect ratio together with distortion in the form of a parallelogram, and (c) elements with high aspect ratio together with distortion in the form of a trapezium. Two load cases are considered: pure bending and shear force at the end. The material behavior is modeled as isotropic linear elastic with Young's modulus $E = 10^7 \mathrm{N/mm}^2$ and Poisson's ratio $\nu = 0.3$. The depth of the beam is $d = 0.1\mathrm{m}$.

Numerical solutions obtained using different elements are presented in Table 6.3. Displacements have been normalized with respect to those from the exact analytical solution. It is seen that results using the ANDES element, especially in cases (b) and (c), deviate substantially from analytical results for the mesh arrangements in Figure 6.4 suggested in reference [92]. This example shows that the ANDES element is sensitive to mesh distortion

Table 6.3: Example 4 — Tip deflection for MacNeal's beam problem normalized with respect to the exact analytical solution

Elements	Shear (P)			Moment (M)		
	Mesh(a)	Mesh(b)	Mesh(c)	Mesh(a)	Mesh(b)	Mesh(c)
CPS4	0.093	0.035	0.003	0.093	0.031	0.022
P-S	0.993	0.798	0.221	1.000	0.852	0.167
ANSYS	0.979	0.624	0.047	–	–	–
Q6	0.993	0.677	0.106	1.000	0.759	0.093
AGQ6-I	0.993	0.994	0.994	1.000	1.000	1.000
AGQ6-II	0.993	0.994	0.994	1.000	1.000	1.000
ANDES	**0.907**	**0.575**	**0.500**	**0.910**	**0.666**	**0.046**

in in-plane bending. From Table 6.3, it is seen that the AGQ6-I and AGQ6-II elements perform well in MacNeal's beam test, but as noted earlier, do not pass the patch test. On the other hand, the ANDES element passes the patch test, but does not work satisfactorily in in-plane bending. This result is consistent with the finding by MacNeal [91] that a 4-node quadrilateral element with two degrees of freedom per node either fails to pass the constant strain/stress patch test, or locks in in-plane bending in case of distorted mesh.

6.1.5 Example 5: Axially loaded cantilever beam — geometric nonlinearity

In this example, the goal is to explore the accuracy of the corotational kinematic description. A cantilever beam of length 5.0m, depth 0.1m, and thickness 1.0m is considered. The geometry is perturbed to reflect an initial imperfection. A displacement is imposed at the tip in the axial direction. The material is again modeled as isotropic linear elastic with the same properties as in Example 1. First, a very small initial imperfection of 0.01m is considered at the tip, to represent Euler buckling closely. Next, a larger imperfection of 0.2m is considered. Analysis cases including different element types, discretizations and solution algorithms are summarized in Table 6.4. The cases that use the displacement-based algorithm and total Lagrangian kinematics are performed using ABAQUS. The solutions obtained using a higher order displacement-based element (CPS8) and total Lagrangian kinematic descrption are considered the reference. The standard displacement-based 4-node

quadrilateral (CPS4) element is included in the study so that the CR and TL kinematic descriptions can be compared with all other parameters held fixed.

For the small imperfection of 0.01m, numerical results are shown in Figure 6.5(b). It can be seen that the solutions obtained using the ANDES element and the CPS8 element are very close to the analytical Euler buckling load, $\pi^2 EI/L^2 = 6579.74$kN. Furthermore, the solutions obtained using the ABAQUS CPS4 element with TL kinematic description and the displacement element with CR kinematic descriptions, while far away from the analytical solution, are identical to each other. This indicates the agreement between the TL and CR kinematic descriptions. For the larger imperfection of 0.2m, results are shown in Figures 6.6 and 6.7. In both the coarse and fine meshes, the CPS4 element TL and CR solutions agree. With the fine mesh, the ANDES element CR solution agrees with the CPS8 TL reference solution. It can also be observed that the ANDES coarse mesh solution is more accurate than the CPS4 counterpart. This example illustrates the adequacy of the CR description for this type of problem.

6.1.6 Example 6: Axially loaded cantilever — combined elastoplasticity and geometric nonlinearity

The goal in this example is to examine the optimization algorithm for elastoplasticity, in addition to the CR kinematic description. The cantilever beam of Example 2 with the larger imperfection of 0.2m is again considered. The material is now modeled as elastic-ideal plastic with von Mises yield criterion. The elastic material properties are the same as in Example 2, and the uniaxial yield stress, $\sigma_y = 250\text{N/mm}^2$. The finite element discretizations are shown in Figures 6.6(a) and 6.7(a), and the different analysis cases are summarized in Table 6.5.

Numerical results are shown in Figures 6.8 and 6.9. The analysis cases using the CPS4 element on one hand with TL kinematic description and displacement-based algorithm, and on the other hand with CR kinematic description and the optimization algorithm produce identical results. This demonstrates the correctness of the CR description and the optimiza-

Table 6.4: Example 5 — Summary of analysis cases

(a) Analysis cases with small imperfection (0.01m)

Case	1(a)	1(b)	1(c)	1(d)
Imperfection (m)	0.01	0.01	0.01	0.01
Elem along length	100	100	100	100
Elem along depth	2	2	2	2
Element type	ANDES	CPS8	CPS4	CPS4
Kinematics[3]	CR	TL	CR	TL
Algorithm	Opt[1]	Disp[2]	Opt	Disp

[1] Displacement-based solution algorithm
[2] Optimization algorithm described in chapter 2
[3] Analysis cases using Disp and TL are performed using ABAQUS

(b) Analysis cases with larger imperfection (0.02m)

Case	2(a)	2(b)	2(c)	2(d)	3(a)	3(b)	3(c)	3(d)
Imperfection (m)	0.2	0.2	0.2	0.2	0.2	0.2	0.2	0.2
Elem along length	50	50	50	50	200	200	200	200
Elem along depth	1	1	1	1	4	4	4	4
Element type	ANDES	CPS8	CPS4	CPS4	ANDES	CPS8	CPS4	CPS4
Kinematics	CR	TL	CR	TL	CR	TL	CR	TL
Algorithm	Opt	Disp	Opt	Disp	Opt	Disp	Opt	Disp

Table 6.5: Example 6 — Summary of analysis cases

Case	4(a)	4(b)	4(c)	4(d)	5(a)	5(b)	5(c)	5(d)
Imperfection (m)	0.2	0.2	0.2	0.2	0.2	0.2	0.2	0.2
Elem along length	50	50	50	50	200	200	200	200
Elem along depth	1	1	1	1	4	4	4	4
Element type	ANDES	CPS8	CPS4	CPS4	ANDES	CPS8	CPS4	CPS4
Kinematics	CR	TL	CR	TL	CR	TL	CR	TL
Algorithm	Opt	Disp	Opt	Disp	Opt	Disp	Opt	Disp

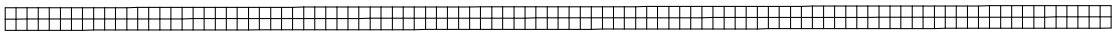

(a) 100 elements × 2 elements mesh

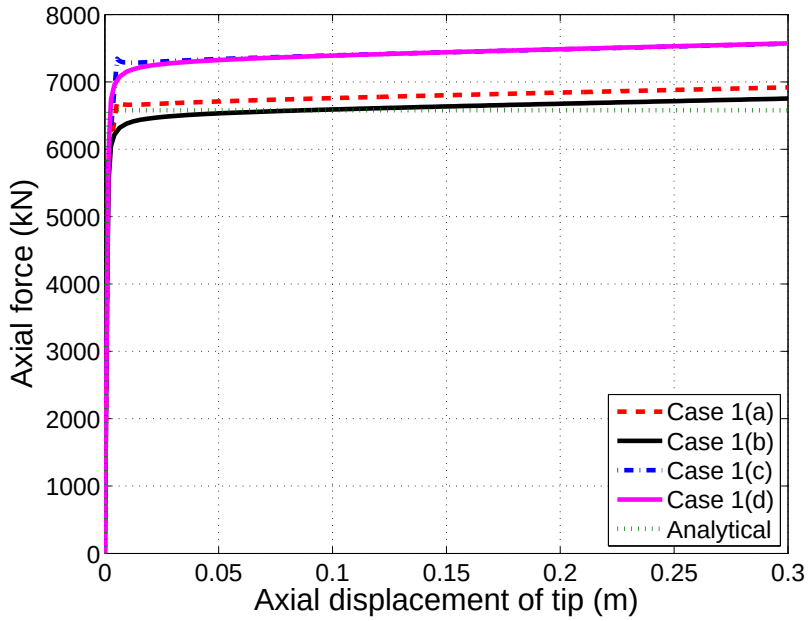

(b) Axial force-displacement plot

Figure 6.5: Example 5 — Axially loaded cantilever with 0.01m imperfection (Euler buckling)

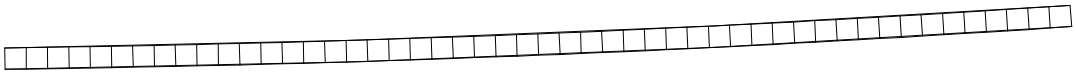

(a) 50 elements × 1 element mesh

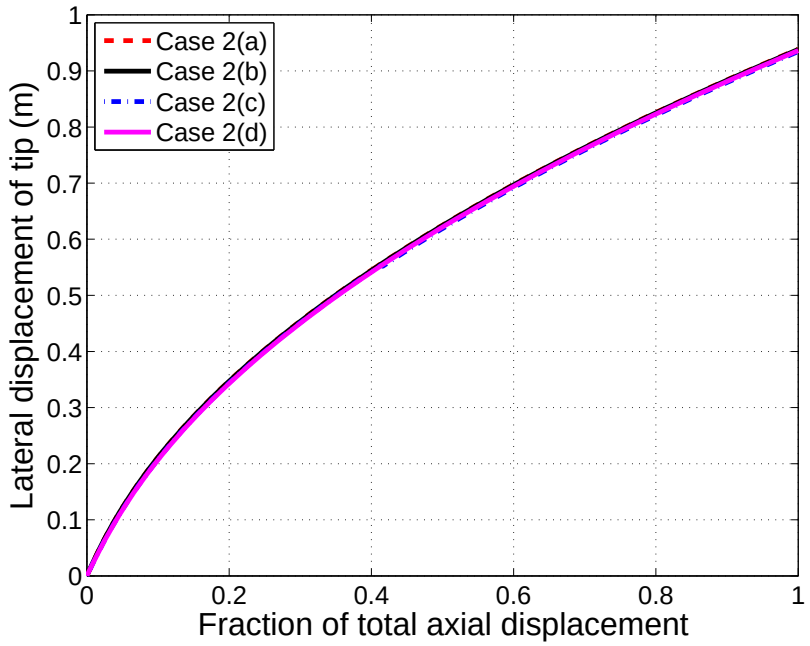

(b) Tip displacement for 50 × 1 mesh

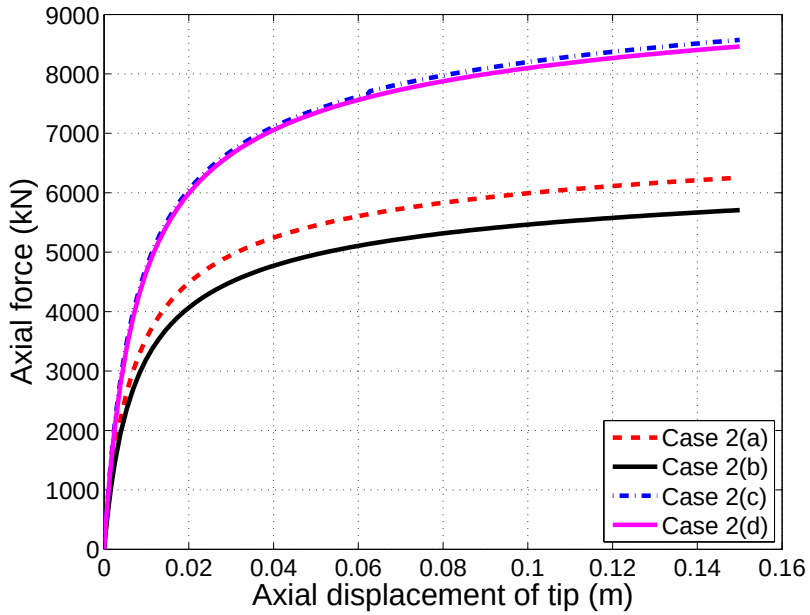

(c) Axial force-displacement plot for 50 × 1 mesh

Figure 6.6: Example 5 (geometric nonlinearity) — Coarse mesh results for axially loaded cantilever with 0.2m imperfection

(a) 200 elements × 4 elements mesh

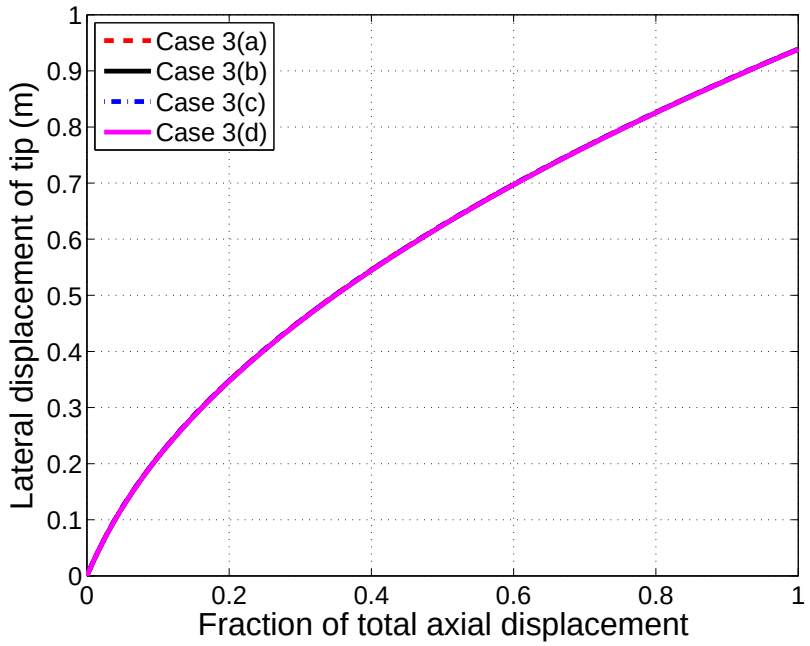

(b) Tip displacement for 200 × 4 mesh

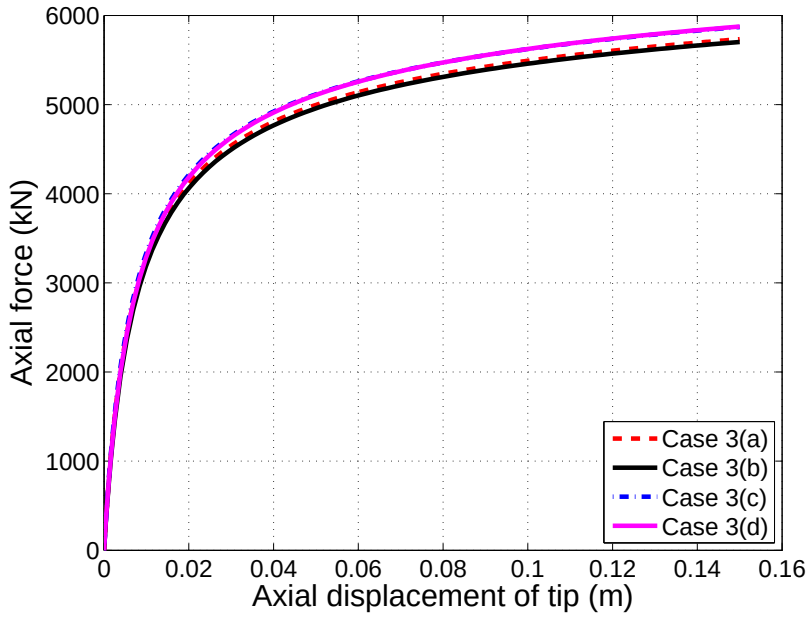

(c) Axial force-displacement plot for 200 × 4 mesh

Figure 6.7: Example 5 (geometric nonlinearity) — Fine mesh results for axially loaded cantilever with 0.2m imperfection

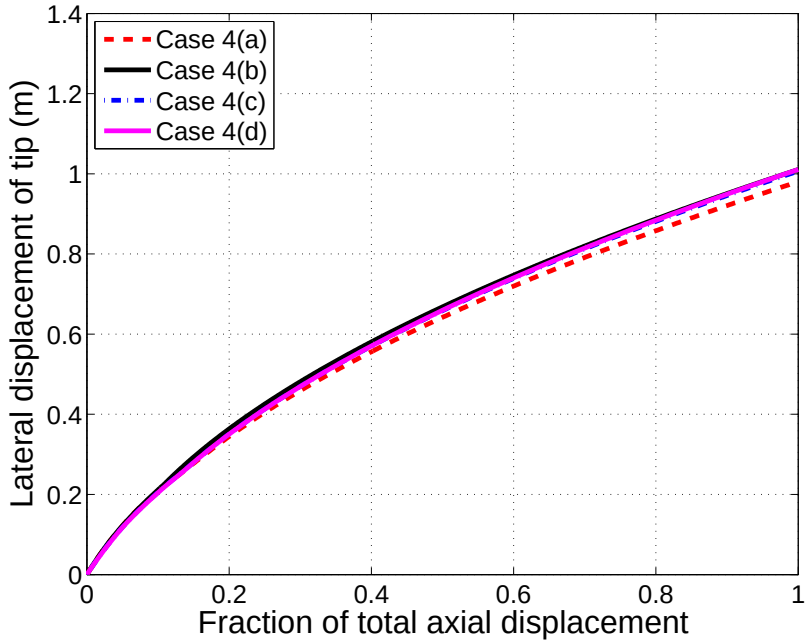

(a) Tip displacement for 50×1 mesh

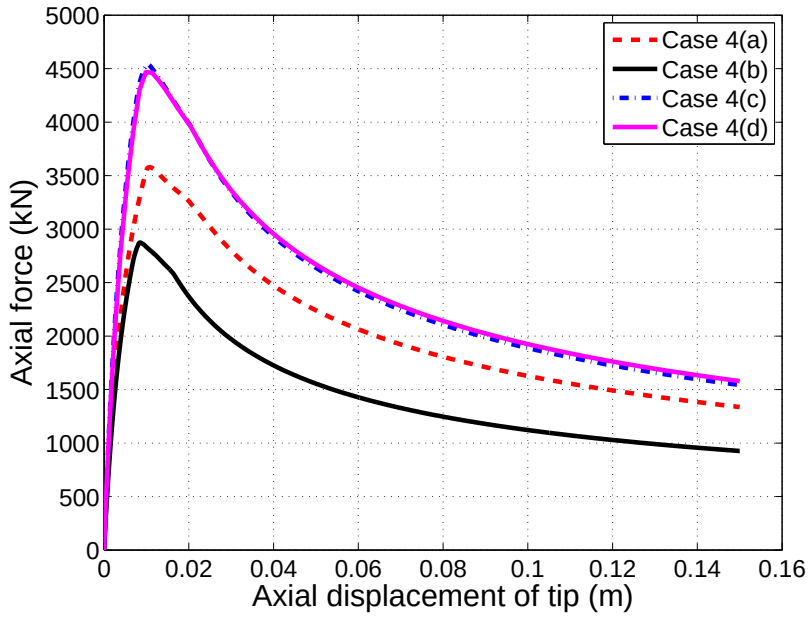

(b) Axial force-displacement plot for 50×1 mesh

Figure 6.8: Example 6 (combined elastoplasticity and geometric nonlinearity) — Coarse mesh results for axially loaded cantilever with 0.2m imperfection

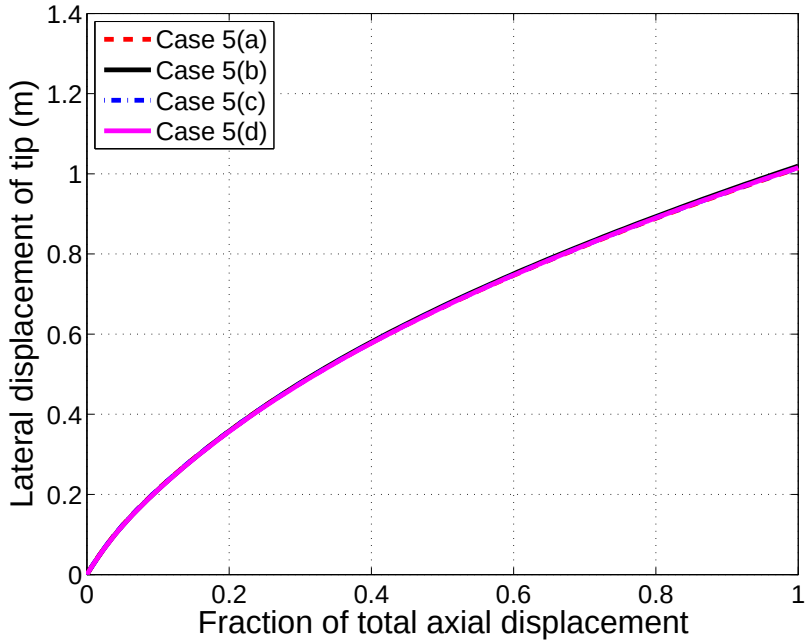

(a) Tip displacement for 200×4 mesh

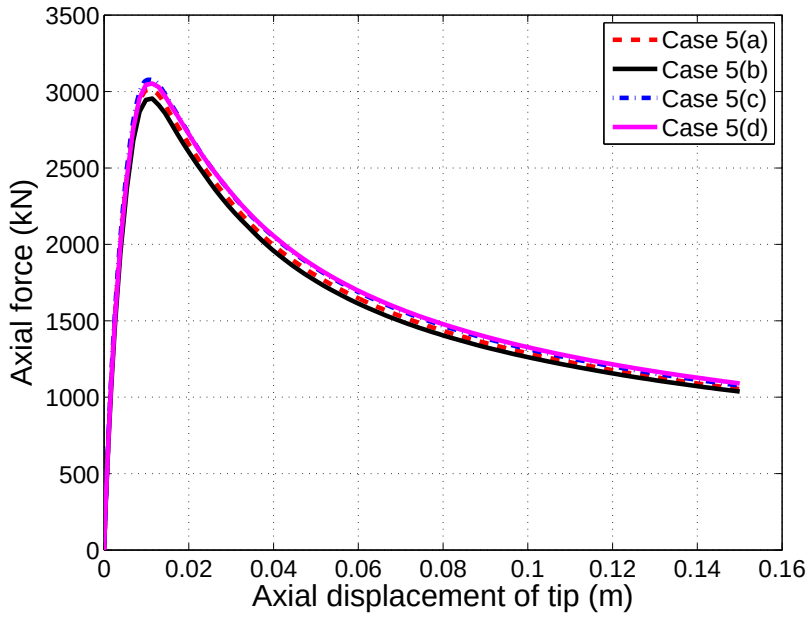

(b) Axial force-displacement plot for 200×4 mesh

Figure 6.9: Example 6 (combined elastoplasticity and geometric nonlinearity) — Fine mesh results for axially loaded cantilever with 0.2m imperfection

tion algorithm. With the finer mesh, the solution obtained using the (low order) ANDES element with CR kinematics and the optimization algorithm is very close to the reference solution with the (higher order) CPS8 element with TL kinematics and a displacement-based algorithm. Due to the explicit update of the geometry (equation (2.19)), it is found that smaller increments are necessary near the peak force.

6.1.7 Example 7: Elastoplastic bending of a thin circular arch

In this example, a very thin circular arch of mean radius 10.1m and thickness 0.2m is considered. The material properties are the same as in Example 3. The model is subjected to tip displacements of -1.0m each in horizontal and vertical directions. The purpose of this example is to show the limitation of CR kinematics when the structure experiences finite deformation. The finite element mesh and the numerical results are shown in figure 6.10. It is observed that both kinematic descriptions and both solution algorithms give close results up to the vertical displacement of 0.5m. After this, the reaction-displacement curves diverge. This is due to the fact that large strain develop in the plastic zone in the post-buckling behavior. (The kink in figure 6.10(c)) The softening behavior shown in figure 6.10(b) is due to nonlinear geometric effect. The maximum value of displacement of the interior edge is $u_x = -1.41$m and $u_y = 0.3$m.

6.2 ANS-ANDES-EAS Solid-shell element

In this section, numerical benchmarks are analyzed to investigate the performance of the first proposed solid-shell element formulation (based on ANS,ANDES and EAS concepts) in both geometrically linear and nonlinear cases. Results are compared with those from other formulations in the literature (Table 6.7). Since some cited formulations have been normalized to different reference values, some of the results from the literature are re-normalized in this work.

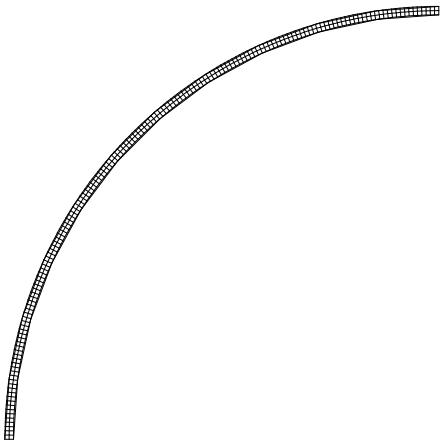

(a) Finite element mesh

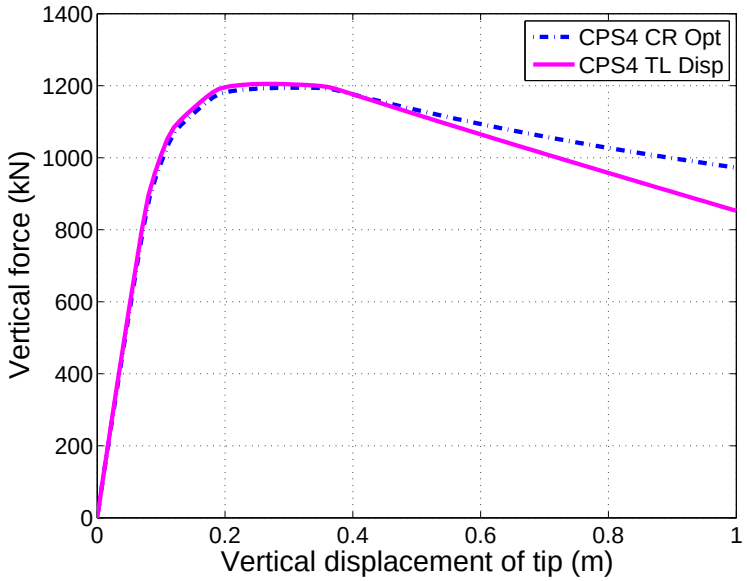

(b) Force vs. vertical displacement

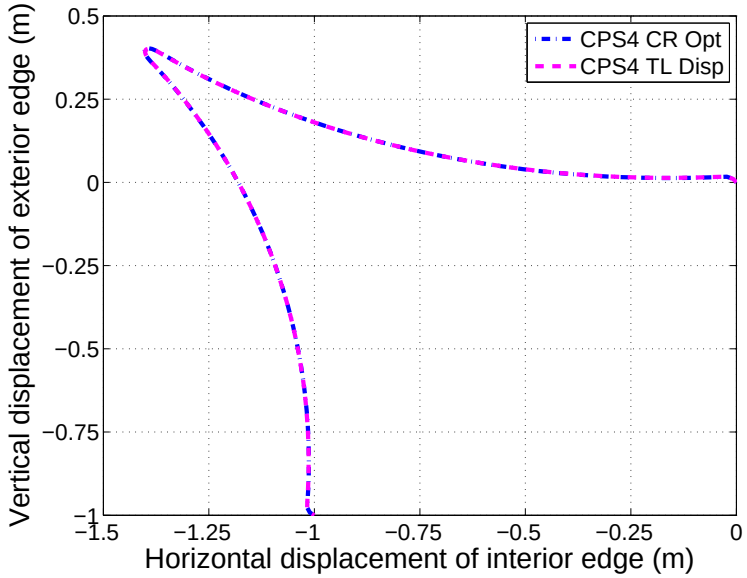

(c) Horizontal vs vertical displacement of the interior edge in the last increment

Figure 6.10: Example 7 — Elastoplastic bending of a thin circular arch

Table 6.6: References used to compare solutions in numerical examples

Abbreviation	Reference	Description
Full-integration solid and solid-shell elements		
Kli06	Klinkel et. al. [148]	mixed ANS solid-shell (HSEE).
Kim05	Kim et. al. [82]	ANS solid-shell with plane stress assumption for thickness strains (XSolid85).
Alv03	Alves de Sousa et. al. [6]	eight-node EAS solid-shell with twelve enhanced variables (HCis12).
Are03	Areias et. al. [9]	EAS solid element with penalty stabilization.
Sze00	Sze et. al. [142]	Hybrid stress ANS solid-shell ($ANS_{\gamma\epsilon}$ and $ANS_{\gamma\epsilon}$-HS).
Kas00	Kasper et. al. [80]	Mixed Enhanced strain element with nine enhanced variables (H1/ME9).
Reduced-integration solid and solid-shell elements		
Schw09	Schwarze and Reese [119, 120]	ANS/EAS solid shell with one EAS variable and using the Taylor expansion of the inverse Jacobian with respect to the element center (Q1ST).
Abed09	Abed and Combescure [3]	Assumed strain solid shell with physical stabilization (SHB8PS).
Car08	Cardoso et. al. [41]	ANS/EAS solid-shell with one EAS variable (MRESS).
Ree07	Reese[115]	EAS Solid-shell (Q1SPs).
Alv05	Alves de Sousa et. al. [5]	EAS/SRI solid-shell with one EAS variable and SRI technique for transverse shear locking (RESS).
SC8R	ABAQUS continuum solid [1]	Reduced integration continuum solid element of ABAQUS.

Table 6.7: References used to compare solutions in numerical examples (Continued)

Abbreviation	Reference	Description
Full- and reduced-integration conventional shell elements		
CYSE	Cardoso et. al. [40]	one-point quadrature shell element with stabilization of spurious energy modes.
Gru05	Gruttmann and Wagner [65]	ANS mixed stress element with reduced integration.
iCYSE-E4	Cardoso et. al. [38]	Four-node reduced integration shell element with four enhancing variables for membrane strains.
Car02	Cardoso et. al. [39]	ANS element with reduced integration.
ANS_{γ}-EAS	Bischoff and Ram [35]	Full-integration EAS shell, which takes the thickness stretch into account.
ANDES3	Militello and Felippa [98]	Full-integration triangular shell element with drilling degrees of freedom based on ANDES approach.
ANDES4	Haugen and Felippa[68]	Full-integration quadrilateral shell element with drilling degrees of freedom based on ANDES approach.
Parisch91	Parisch [103]	Full-integration ANS element.
Simo89	Simo and Fox [126]	Full-integration mixed ANS Stress element.
Stander89	Stander et. al. [137]	Full-integration quadrilateral ANS element.
Bat85	Bathe and Dvorkin [17]	Full-integration quadrilateral ANS element.
S4R	ABAQUS shell element[1]	Four-node reduced-integration shell element with hourglass stabilization.

Geometrically linear elastic solid-shell:

In this section the numerical examples of several well-known benchmarks for linear elastic materials are presented. The numerical examples for geomterically linear element and the challenging features of each are presented in Table 6.8.

6.2.1 Example 8: Patch tests

The patch test is a standard approach for evaluating the completeness of an element formulation [18, 74]. Each element is subject to specific nodal displacements that analytically correspond to a state of constant strain within the element. If the finite element produces exactly the same strain state as the analytical, the patch test is passed. It is explained by Taylor *et. al* in [144] that the patch test is a condition to assess the convergence of the finite element approximations, which is equivalent to consistency condition. This test is more significant in evaluating the convergence of elements employing nonstandard features (as examples: selective integrations, incompatible interpolations or EAS elements) [153]. MacNeal and Harder [92] proposed the membrane and bending patch tests for 3D elements (solid, shell). The membrane patch test has a higher significance since it assesses the completness and convergence of the element assemblage. But in the context of the shell and solid-shell elements, the bending patch test is also of great importance to evaluate the bending behavior of the formulation with only one element across the thickness. This issue is directly related to the number of elements and the calculation costs.

Referring to Macneal and Harder [92], a solid element of length $L = 0.24$mm, width $B = 0.12$mm and thickness $t = 0.001$mm shown in Figure 6.11 is meshed with five distorted elements.

Membrane patch test: A displacement state is applied on the structure that leads to a constant in-plane strain distribution. The material behavior is modeled as isotropic linear elastic with material properties as E= 10^6 N/mm^2 and $\nu = 0.25$. The displcaments of the exterior nodes are prescribed by linear functions:

Table 6.8: Numerical examples for the geometrically linear element:

Numerical example	**Challenging feature**
Membrane patch test	Evaluating the completeness of the finite element formulation.
Bending patch test	Ability of the element to reproduce a constant bending stress state.
Pinched cylinder with end diaphragms	Performance of the element for inextensional bending and complex membrane modes.
Scordelis-Lo roof	The membrane and bending behavior of the element formulation.
Hemispherical shell with 18^o hole	The ability of the element to represent inextensional membrane and bending modes.
Full hemispherical shell	The ability of the element to represent inextensional membrane and bending modes when the bending is about the diagonal plane.
Twisted beam	Performance of the element in case of warping geometry.
Clamped square plate	The element sensitivity to distorted mesh in out-of-plane bending problems.
Cook's skew plate	Membrane behavior of the element in inplane bending problems.

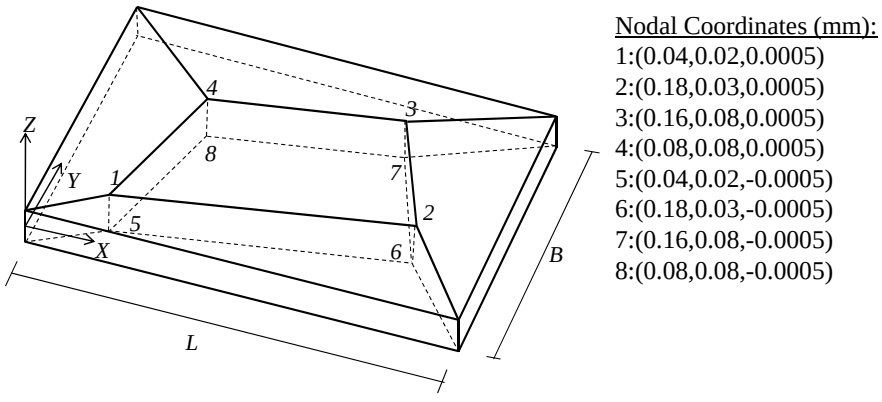

Figure 6.11: Example 8 — Patch test geometry

Table 6.9: Example 8 — Membrane Patch test, The finite element solution results

Node	U_X(mm)	U_Y(mm)
1	5.000e-5	4.000e-5
2	1.950e-4	1.200e-4
3	2.000e-4	1.600e-4
4	1.200e-4	1.200e-4

$$U_X = 10^{-3}\left(X + \frac{Y}{2}\right),\ U_Y = 10^{-3}\left(Y + \frac{X}{2}\right) \tag{6.1}$$

and the $U_Z = 0$ is prescribed for the bottom layer of nodes. Assuming the above displacements at exterior nodes, a constant strain distribution leading to a plane stress state is obtained. The displacements of the nodes are shown on Table 6.9. The results agree exactly with the solution of equation (6.1) and the stresses at Gauss points are:

$$\sigma_{XX} = \sigma_{YY} = 1333.33\text{N/mm}^2,\ \sigma_{XY} = 400.0\text{N/mm}^2 \tag{6.2}$$

which agrees with the analytical solution. All other stresses are zero in this plane stress problem. Hence, the membrane patch test is passed.

Bending patch test: In this test the patch shown in Figure 6.11 is tested to reproduce a constant bending stress state. The displacements of exterior nodes are:

$$U_X = \mp t\frac{10^{-3}}{2}\left(X + \frac{Y}{2}\right), U_Y = \mp t\frac{10^{-3}}{2}\left(Y + \frac{X}{2}\right), U_Z = \frac{10^{-3}}{2}\left(X^2 + XY + Y^2\right) \tag{6.3}$$

which shows a linear strain distribution in thickness direction. The displacement of the internal nodes are shown in Table 6.10. The numerical results produce the analytical solutions exactly. In order to analyze the stresses at top and bottom surfaces, the values at Gauss points are exterpolated across the thickness. The resulting stresses at top and bottom

Table 6.10: Example 8 — Bending Patch test, The finite element solution results

Node	U_X(mm)	U_Y(mm)	U_Z(mm)
1	-2.500e-8	-2.000e-8	1.400e-6
2	-9.750e-8	-6.000e-8	1.935e-5
3	-1.000e-7	-8.000e-8	2.240e-5
4	-6.000e-8	-6.000e-8	9.600e-6

surfaces are as follows:

$$\sigma_{XX} = \sigma_{YY} = \pm 0.6667\text{N/mm}^2, \sigma_{XY} = \pm 0.200\text{N/mm}^2 \tag{6.4}$$

which conforms with the analytical solution. Hence the bending patch test is also passed. This example shows that the ANDES approach has an excellent performance to account for the membrane response of the solid-shell formulation.

6.2.2 Example 9: Pinched cylinder with end diaphragms

This test is one of the three "obstacle course" problems proposed by Belytschko for shell elements [25]. The test assesses the performance of the element for inextensional bending and complex membrane modes. This is one of the most demanding tests for the solid-shell formulation since it involves both the membrane and bending responses of the element. Another aspect of this test is that the solid-shell formulation is checked for trapezoidal locking that could occur when modeling curved shells.

Two mesh types are investigated in this example — a regular mesh and a distorted mesh. The distorted mesh also causes the mid-surface to be warped.

The cylinder is pinched by two diametrically opposite point loads with the magnitude of $P = 1.0$N. The material behavior is modeled as isotropic linear elastic with material properties as: Young's modulus $E = 3 \times 10^6\text{N/mm}^2$, Poisson's ratio $\nu = 0.3$. The geometry of the model is defined as: radius, $R = 300$mm, length $L = 600$mm and thickness $t = 3.0$mm. Owing to symmetry, only one-eighth of the cylinder is modeled. The analytical solution for

Table 6.11: pinched cylinder(distorted mesh),Normalized displacement of the point under the load

Distortion angle	$\theta = 0^o$	$\theta = 10^o$	$\theta = 20^o$	$\theta = 30^o$	$\theta = 40^o$
Normalized displacement(r)	0.970	0.963	0.926	0.925	0.924

the vertical displacement under the point load is $U_Y = -1.8248 \times 10^{-5}$mm [25].

–Regular mesh

In this model, the mesh arrangement is as shown in Figure 6.12(a). In Figure 6.12(c), the vertical displacements under the point load are normalized to the analytical solution and compared with some cited solid-shell (MRESS, H1/ME9, RESS, HCiS12, ANS$_{\gamma\epsilon}$, ANS$_{\gamma\epsilon}$-HS) and shell(ANS$_{\gamma}$-EAS) formulations.

As it can be seen in the figure, all the elements show poor convergence for coarse meshes. Comparing with other existing solid-shell and shell elements, the current element has a better rate of convergence followed by MRESS, which is an ANS element.

–Distorted mesh

In this model,the mesh arrangement is selected as 20×20. The mesh is given an increasing distortion angle θ as shown in Fig 6.12(b). As θ increases, the mid-surfaces of the elements are no longer flat and the element is with warped mid-surface. This induced warping, which increases with the increase in θ, changes the normalized displacement of the node under the load from $r = 0.97$ for $\theta = 0.0$(regular mesh) to $r = 0.924$ for $\theta = 40.0$ (very distorted mesh) as can be seen in table 6.2.2.

In the pinched cylinder test the distorted mesh arrangement causes the membrane locking problem, but using the ANDES scheme for the membrane response of the element alleviates the membrane locking and the results are very slightly sensitive to the mesh distortion.

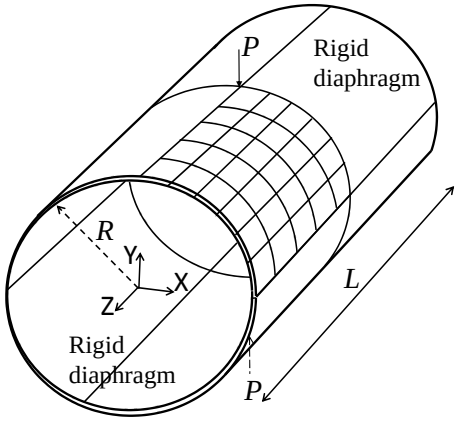

(a) Regular mesh

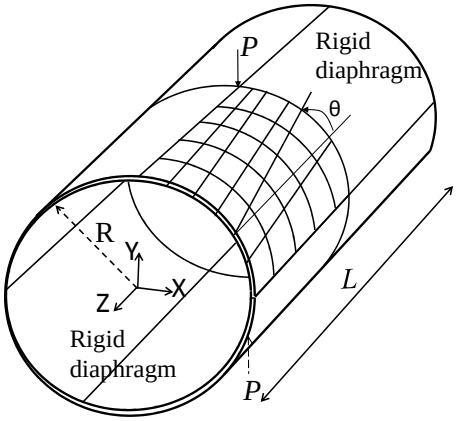

(b) Distorted mesh

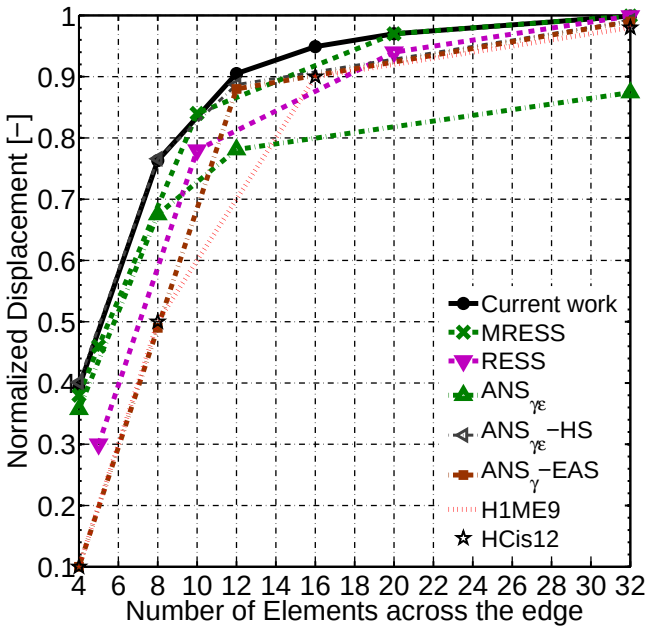

(c) Convergence study considering regular mesh

Figure 6.12: Example 9 — Pinched Cylinder with end diaphragms

6.2.3 Example10: Scordelis-Lo Roof

This benchmark is another obstacle course problem for single curved shell elements originally proposed by Scordelis and Lo [121]. The goal of this test is to assess the membrane and bending behavior of the shell element formulation. As shown in Figure 6.13,the

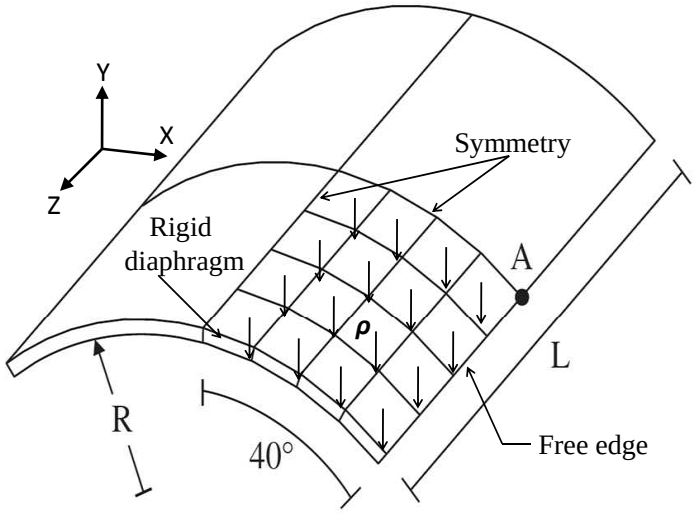

Figure 6.13: Example 10 — Scordelis-Lo roof,geometry

roof is mounted on two rigid diaphragms at two curved edges and loaded under its own weight. The material behavior is modeled as isotropic linear elastic with material properties as: Young's modulus $E = 4.32 \times 10^8$ N/mm^2, Poisson's ratio $\nu = 0.0$. The geometry of the model is defined as: radius, $R = 25.0$mm, length $L = 50$mm and thickness $t = 0.25$mm. The volume force is $\rho = 360$ N/mm^3 and owing to symmetry, only a quarter of the cylinder is modeled.

The boundary conditions of the rigid diaphragms are defined by $U_X = U_Y = 0$. The analytical solution for the vertical displacement of point **A** under the volume load is $U_Y = -0.3024$mm. The vertical displacements of point **A** are normalized to the reference analytical value and presented in Table 6.12 along with the results for some existing solid-shell formulations (Q1STs, RESS, XSolid85, Are03 and ANS$_{\gamma\epsilon}$).

The convergence is satisfactory and occurs from above. Unlike the pinched cylinder

Table 6.12: Example 10 — Scordelis-Lo roof,Normalized displacement of point **A**

n_e	**Current work**	Schw09 (Q1STs)	Alv05 (RESS)	Kim05 (XSolid85)	Are03	Sze00 (ANS$_{\gamma\epsilon}$)
4×4	**1.047**	0.997	0.995	0.960	1.029	0.938
8×8	**1.011**	0.994	0.986	0.984	1.001	0.962
16×16	**0.996**	1.000	0.993	0.999	0.992	-
32×32	**0.997**	1.003	0.996	-	0.991	-

test, in this problem, the free edge deflection is dominated by the membrane-bending coupling along the Z direction (bending about the X axis) and the elements are not tapered in that direction.

6.2.4 Exaple 11: Hemispherical shell with 18^o hole

This is the third obstacle course problem for doubly-curved shells, which assesses the ability of the element to represent inextensional membrane and bending modes. The geometry of the model is shown in Figure 6.14. The radius of the curved shell is $R = 10.0$mm and the thickness is $t = 0.04$mm. Due to symmetry, only a quadrant of the hemisphere is modeled. The equator represents a free edge and the XZ and YZ planes are the symmetry planes. The structure is subjected to two pairs of diametrically opposite loads along the X and Y axes respectively. A hole is designed by angle $\theta = 18^o$ with respect to the Z axis to simplify the mesh generation. The load value is $F = 1.0$N. The material behavior is modeled as isotropic linear elastic with material properties as: Young's modulus $E = 6.825\times10^7$ N/mm^2 and Poisson's ratio $\nu = 0.3$.

The displacements of node **A** are normalized to the reference value $U_X = 0.0940$mm [92] and presented in Table 6.13 along with some other existing solid-shell formulations(Q1STs, Q1SPs, XSolid85, Are03, H1/ME9, ANS$_{\gamma\epsilon}$-HS). Comparing the convergence ratio of different formulations, it can be deduced that the ANS approach is more effective in circumventing the shear locking problem in thin shells rather than the EAS method. The proposed element formulation has the best convergence among the existing solid-shell elements.

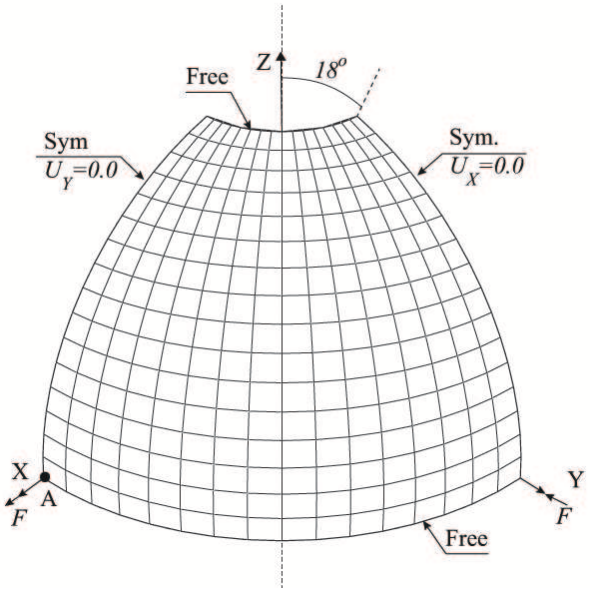

Figure 6.14: Example 11 — Hemisphere with 18° hole, geometry

Table 6.13: Example 11 — Hemispherical shell with 18^o hole,Normalized displacement of point **A**

n_e	**Current work**	Schw09 (Q1STs)	Ree07 (Q1SPs)	Kim05 (XSolid85)	Are03	Kas00 (H1/ME9)	Sze00 (ANS$_{\gamma\epsilon}$-HS)
4×4	**1.018**	1.043	0.062	1.058	0.040	0.039	1.062
8×8	**0.997**	1.002	0.723	1.005	0.756	0.732	1.006
16×16	**0.986**	0.993	0.919	-	0.991	0.989	-
32×32	**0.990**	0.994	0.969	-	0.999	0.998	-

6.2.5 Example 12: Full hemispherical shell (linear elastic)

In this example, the previous test is investigated without the 18^o hole as shown in Figure 6.15. This is a more demanding test on the formulation because the element is bending about the diagonal plane. In Table 6.14, the displacements of point **A** are normalized to the reference value $U_X = 0.0924$mm [92] along with some other existing solid-shell (Q1STs, Q1SPs, XSolid85, Are03) and shell (Gru05 and Car02) formulations.

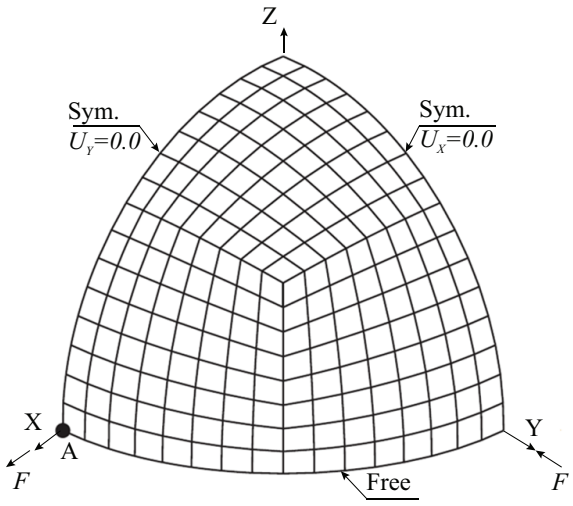

Figure 6.15: Example 12 — Full Hemisphere problem, geometry

The results show that the proposed element has the best convergence rate among the cited solid-shell elements but Car02 shell element exhibits slightly better result for the coarse mesh arrangement.

6.2.6 Example 13: Twisted Beam

The twisted beam benchmark proposed by MacNeal and Harder is to assess the warping performance of the element [92]. The twisted beam has length $L = 12$mm, width $W = 1.1$mm and thickness $t = 0.32$mm as shown in Figure 6.16(a). Another version of the twisted beam problem was proposed by Simo in reference [126] with thickness of $t = 0.05$mm, which is a

Table 6.14: Example 12 — Full hemispherical shell, Normalized displacement of point A

n_e	**Current work**	Schw09 (Q1STs)	Ree07 (Q1SPs)	Kim05 (XSolid85)	Gru05	Are03	Car02
4	**0.663**	0.418	0.104	-	0.573	0.029	0.680
8	**0.962**	0.956	0.630	1.079	0.971	0.583	0.980
16	**0.997**	0.996	0.907	1.014	1.002	0.978	0.990
32	**1.002**	0.999	0.970	1.000	1.000	0.999	-

more-demanding problem involving a very thin twisted beam as shown in Figure 6.16(b). In both problems, considering two different load cases, the structure is subjected to in-plane and out-of-plane loads at the tip with the magnitude $F = 1.0$N. The material behavior is modeled as isotropic linear elastic with material properties as: Young's modulus $E = 29.0 \times 10^6$ N/mm^2, Poisson's ratio $\nu = 0.22$.

The tip displacements in loading direction are normalized to the reference analytical values and presented in Tables 6.15 through 6.18 along with the results for some existing solid-shell (Q1STs, MRESS, RESS, ANS$_{\gamma\epsilon}$, ANS$_{\gamma\epsilon}$-HS) and shell (Simo89) formulations.

Numerical results show the excellent performance of all quoted formulations for both thick and thin beams. The current solid-shell formulation has an excellent performance for too warped thin beam.

Table 6.15: Example 13 — Twisted thin beam (reference solution for in-plane load = 1.387mm)

n_e	**Current work**	Schw09 (Q1STs)	Car08 (MRESS)	Alv05 (RESS)	Simo89
6×1	**1.005**	1.002	-	-	0.993
12×2	**1.001**	0.998	0.965	0.998	1.000
24×4	**1.000**	0.999	1.000	1.000	1.001
48×8	**1.000**	1.000	1.001	1.000	1.002

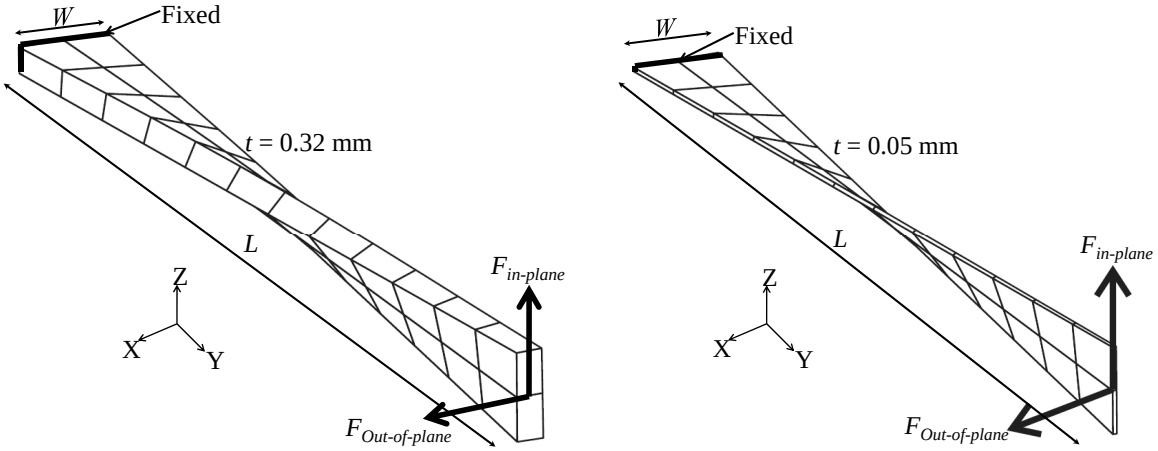

(a) t=0.32mm (b) t=0.05mm

Figure 6.16: Example 13 — Twisted Beam, Geometry.

Table 6.16: Example 13 — Twisted thin beam (reference solution for out-of-plane load = 0.343mm)

n_e	**Current work**	Schw09 (Q1STs)	Car08 (MRESS)	Alv05 (RESS)	Simo89
6×1	**0.953**	0.942	-	-	0.951
12×2	**0.988**	0.983	0.958	0.985	0.986
24×4	**0.995**	0.995	0.995	0.996	0.997
48×8	**1.000**	0.999	0.999	0.998	1.000

Table 6.17: Example 13 — Twisted thick beam (reference solution for in-plane load = 0.005424mm)

n_e	**Current work**	Car08 (MRESS)	Alv05 (RESS)	Sze00 ($ANS_{\gamma\epsilon}$)	Sze00 ($ANS_{\gamma\epsilon}$)-HS
6×1	**0.996**	-	-	0.934	0.998
12×2	**0.997**	1.002	0.994	0.945	1.001
24×4	**0.999**	1.000	0.996	-	-
48×8	**1.000**	1.000	0.997	-	-

Table 6.18: Example 13 — Twisted thick beam (reference solution for out-of-plane load = 0.001754mm)

n_e	**Current work**	Car08 (MRESS)	Alv05 (RESS)	Sze00 (ANS$_{\gamma\epsilon}$)	Sze00 (ANS$_{\gamma\epsilon}$)-HS
6×1	**0.946**	-	-	0.780	0.957
12×2	**0.987**	1.022	0.935	0.887	0.990
24×4	**0.995**	1.006	0.979	-	-
48×8	**0.999**	1.002	0.992	-	-

6.2.7 Exaple 14: Clamped square plate

This test is to assess the element sensitivity to distorted mesh. The geometry is shown in Figure 6.17(a). The side length is $L = 100$mm and the thickness is $t = 1$mm. The material behavior is modeled as isotropic linear elastic with material properties as: Young's modulus $E = 1.0 \times 10^4$ N/mm^2, Poisson's ratio $\nu = 0.30$. A concentrated force with magnitude $F = 16.3527$N is applied at the center of the plate in the negative Z direction. Owing to symmetry, only a quarter of the plate is modeled. Point **A** is moved by e ($0 \leqslant e \leqslant 12$mm) as depicted in the figure 6.17(a). In this example, the model is discretized by 2×2 elements. The analytical solution corresponding to the explained geometry and applied load is provided in [146] as:

$$U_z = 0.00560 F L^2 \frac{12(1-\nu^2)}{E t^3} = -1.000\text{mm} \tag{6.5}$$

The center displacements are normalized with respective to the analytical solution and are plotted versus the **e** values along with some existing solid-shell (Q1STs and HSEE) and shell (Bat85) formulations in Figure 6.17(b). As it is seen in the figure, all elements have satisfactory response for highly distorted meshes and that is due to the fact that the quoted elements use the ANS approach to circumvent the shear locking problem. It is noticeable that among the reported elements, the element proposed in reference [119] behaves slightly better for very distorted mesh arrangement.

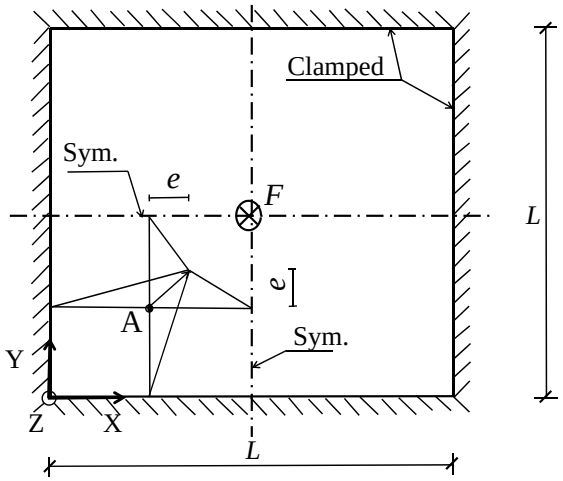

(a) Geometry

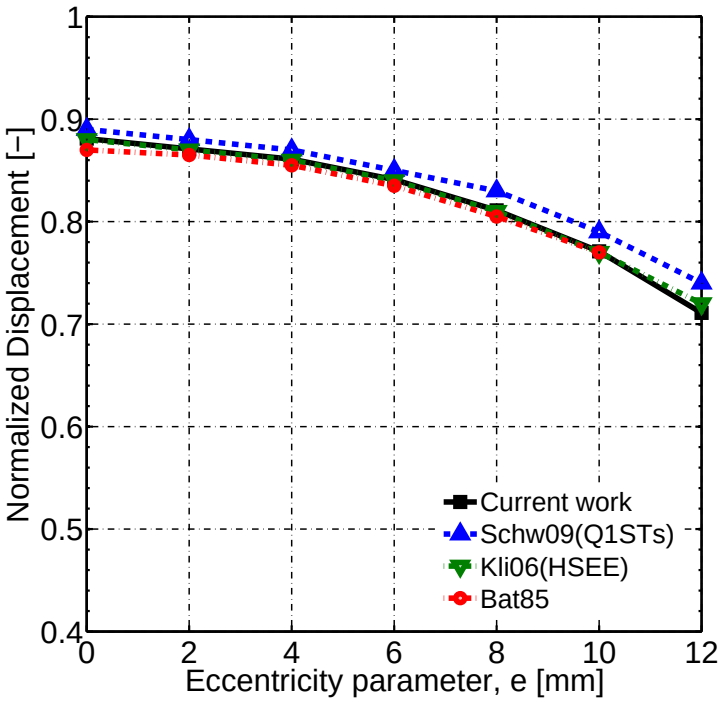

(b) Sensitivity study on distorted mesh

Figure 6.17: Example 14 — Clamped Square Plate

6.2.8 Example 15: Cook's skew plate

This test was first proposed by Cook [45] and applied on shell formulation by Simo in reference [126]. The goal is to assess the membrane behavior of the element. As it is shown in Figure 6.18(a), the trapezoidal beam is clamped at one end and subjected to distributed shear force F= 1/16 at the tip. The material behavior is modeled as isotropic linear elastic with material properties as E= 1.0 and $\nu = 1/3$. The thickness of the model is th= 1.0.

The analytical solution for this problem is $U_y^A = 23.91$. In Figure 6.18(b), the vertical displacements of point **A** are presented along with some existing solid-shell (MRESS and RESS) and shell (CYSE, iCYSE-E4) formulations. For coarse mesh arrangement the current work has better performance than other cited solid-shell formulations, but iCYSE-E4 shell formulation with four enhanced strain variables [40] has better convergence rate even though it does not pass the membrane patch test.

Geometrically nonlinear elastic Solid-shell:

In this subsection some geometrically nonlinear problems are investigated. The **arc length** method originally proposed by Riks [116] with **orthogonal trajectory iterations** [62] for the correction phase is used as the solution algorithm. In all the numerical examples, the unsymmetric stiffness matrices are chosen except the last example in which both symmetrized and unsymmetric stiffness matrices are investigated to compare the results and also the convergence tolerance for the Euclidean norm of the force residual vector is 1.0×10^{-7}. The numerical examples for geometrically nonlinear element and the challenging features of each are presented in Table 6.19.

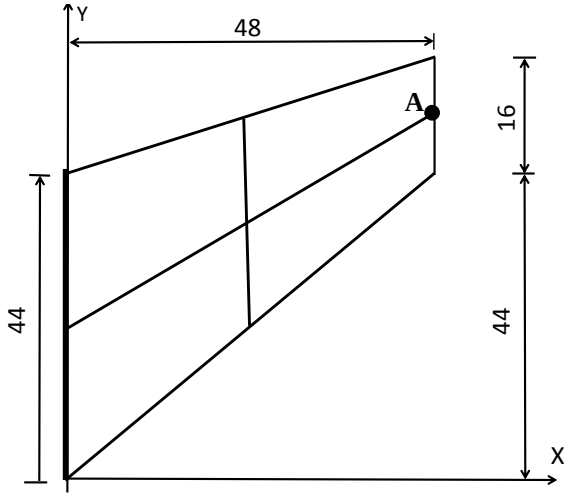

(a) Geometry

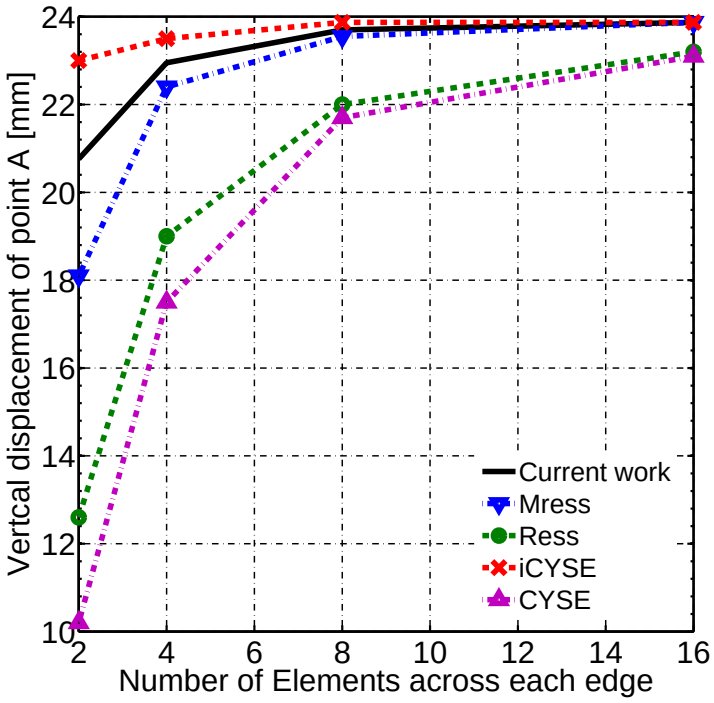

(b) Convergence study

Figure 6.18: Example 15 — Cook's skew plate

Table 6.19: Numerical examples for the geometrically nonlinear element:

Numerical example	**Challenging feature**
Buckling analysis of square plate compressed in one direction	The abality of the formulation in capturing the buckling load and the post-buckling regime.
Pinching of a clamped cylinder	Geometric nonlinear behavior of the element against inextensional bending.
Stretching of a cylinder with free ends	Geometric nonlinear behavior of the element against bending and membrane modes.
Clamped-hinged deep circular arch subjected to a concentrated load	Geometric nonlinear response of the element against nonsymmetric buckling.
Twisted beam under out-of-plane loading	Nonlinear performance of the element in case of warped geometry.
Slit annular plate subjected to lifting line force	Performance of the thin solid-shell structures under finite rotations.
Hinged cylindrical shell under concentrated load	Performance of the formulation in capturing the back-snap response.

6.2.9 Example 16: Buckling analysis of square plate compressed in one direction

In this example, the goal is to compute the buckling and post-buckling behavior of a plate subjected to in-plane uniaxial compression. The plate dimensions are $508 \times 508 \times 3.175$mm as shown in Figure 6.19(a). The material behavior is modeled as isotropic linear elastic with Young's modulus $E = 2.062 \times 10^5 \text{N/mm}^2$ and Poisson's ratio $\nu = 0.30$. The plate is simply supported at all edges but the in-plane deformations are not constrained. Due to symmetry only a quarter of the plate is modeled.

The plate is compressed in its middle plane by uniform load N_X along edge $X = 0$ and $X = L$. The reference solution for the analytical critical value of the compressive force per unit length is given by Timoshenko in [145] as:

$$(N_X)_{cr} = \frac{\pi^2 D}{L^2}\left(m + \frac{1}{m}\right)^2 \text{ where } D = \frac{Et^3}{12(1-\nu^2)} \tag{6.6}$$

m is the number of half-waves in the compressive direction and is one for the first buckling mode. In Table 6.20, the numerical results are normalized to the analytical solution, which is $(N_X)_{cr} = 92.455$ N/mm and are compared with some existing shell formulations (ANDES3 and ANDES4).

It is noted that the corotational kinematic description has been applied on cited elements in Table 6.20 to take the geometric nonlinearity into account as explained in [68]. In order to capture the buckling load, point **A** is perturbed by a load in Z direction with magnitude of 0.0003% of the critical load value.

It is observed that the triangular ANDES3 is slightly better than the proposed element for the coarse mesh because meshes of N×N elements contains twice as many triangular elements as quadrilateral elements, but the proposed solid-shell element converges faster than the quadrilateral ANDES4 element.

Post-buckling analysis is also performed to evaluate the stiffness properties of the square

Table 6.20: Example 16 — Buckling load for square plate subjected to compression,Normalized critical loads

Element type	Number of elements			
	4×4	8×8	16×16	32×32
Curent work	**1.022**	**1.003**	**1.000**	**1.000**
ANDES3	1.008	1.002	1.000	1.000
ANDES4	1.043	1.011	1.002	1.001

plate after the bifurcation is encountered. Mesh arrangement of 8×8 is chosen to discretize one quarter of the plate. In Figure 6.19(c), the incremental load is normalized to the reference critical load and plotted versus the displacement of point **A** in Z direction. The results are compared with the ANDES4 of reference [68]. It is observed that the structure exhibits a stable post-buckling response and is able to undergo increased load after the bifurcation. The deformed shape of the finite element mesh for the first buckling mode is shown in Figure 6.19(b).

6.2.10 Example 17: Pinching of a clamped cylinder

In this test a cantilevered cylinder is subjected to two opposite loads at its open end. Owing to symmetry, only a quarter of the structure is modeled as shown in Figure 6.20(a). The radius of the structure is $R = 1.016$mm, the length is $L = 3.048$mm and the thickness is $t = 0.03$mm. This is a demanding test for the solid-shell elements since they suffer from trapezoidal locking in modeling the curved structures. The material behavior is modeled as isotropic linear elastic with Young's modulus $E = 2.0685 \times 10^7$ N/mm^2 and Poisson's ratio $\nu = 0.30$.

The total Load $P = \lambda P_0$ (load multiplier λ and $P_0 = 1600$N) is applied in 20 equal increments and the tip displacement is controlled up to a total displacement of 1.6 times the radius of the cylinder. On average 6 to 12 iterations are required at each corrector step. It is noted that in this problem, the largest physically possible displacements of the points under the load is equal to the radius of the shell.

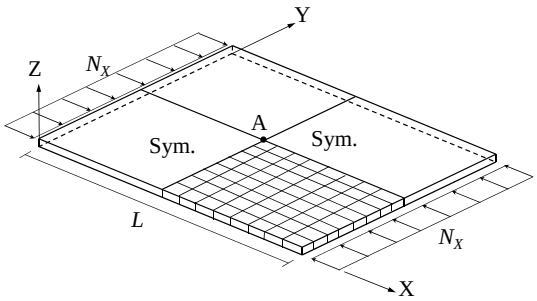

(a) Geometry

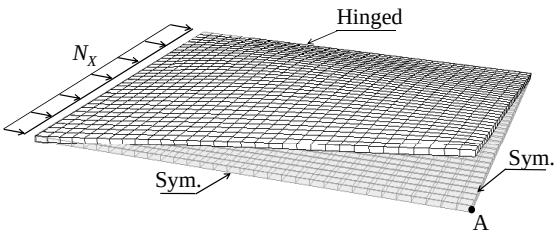

(b) Deformed shape

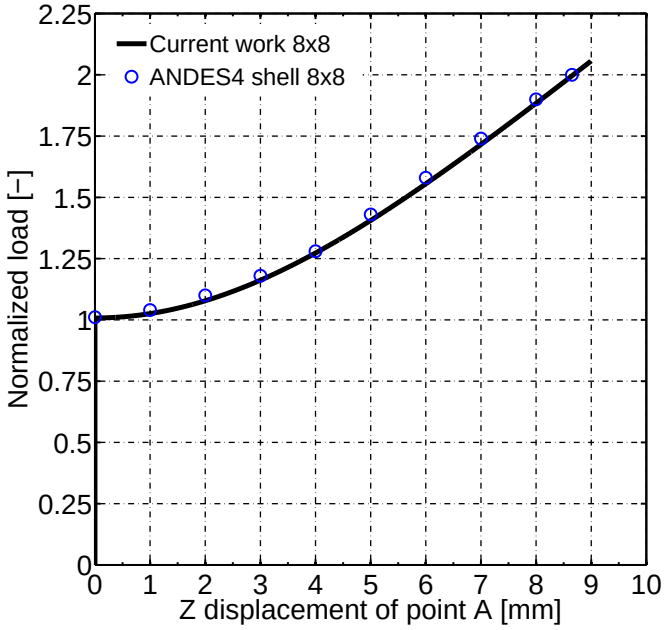

(c) Z displacement of Point A versus the normalized load

Figure 6.19: Example 16 — Buckling analysis of square plate compressed in one direction

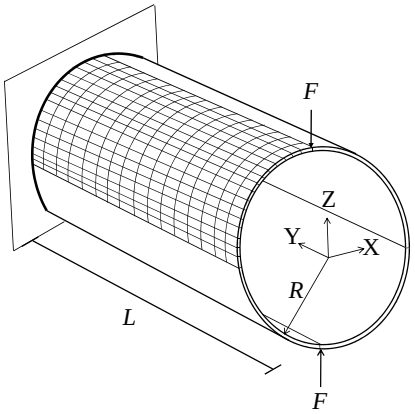

(a) Geometry

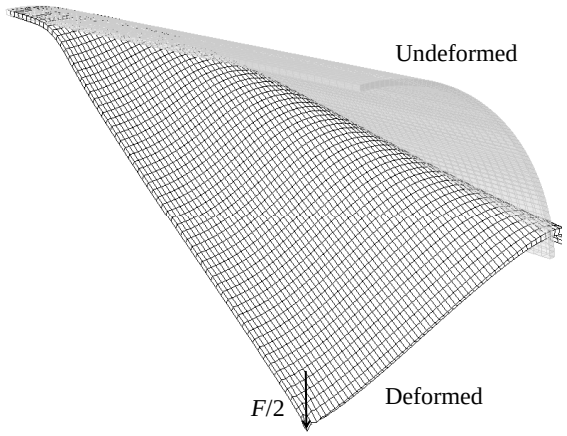

(b) Deformed shape

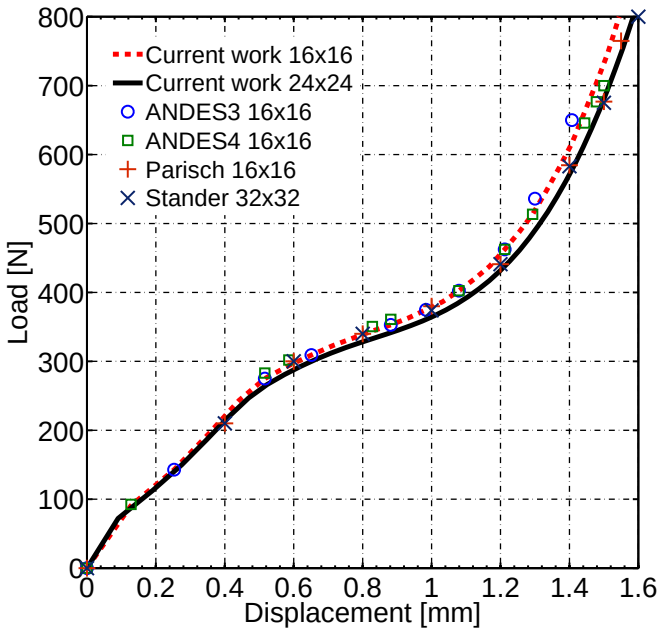

(c) Load-displacement curves for point under the load

Figure 6.20: Example 17 — Pinching of a clamped cylinder

The results of current work are compared to some existing shell formulations(ANDES3, ANDES4, Stander89, Parisch91) in Figure 6.20(c). The results show that the ANDES3 with 16 elements diverges before the analysis finishes, they also show that the solid-shell produces slightly stiffer solution than other shell formulations for 16 elements and this is due to the trapezoidal locking that exists in developing the solid-shell formulation. A regular 24×24 mesh arrangement shows a very good agreement with the published solutions, especially with those from Stander **et. al.** with regular 32×32 meshes.

The deformed finite element mesh at the maximum load value is shown in Figure 6.20(b).

6.2.11 Example 18: Stretching of a cylinder with free ends

In this test, an open cylinder with free ends is subjected to two diametrically opposite forces at the half-length. Due to symmetry only one octant of the cylinder is modeled as shown in Figure 6.21(a). The radius of the structure is $R = 4.935$mm, the length is $L = 10.35$mm and the thickness is $t = 0.094$mm. The material behavior is modeled as isotropic linear elastic with Young's modulus $E = 10.5 \times 10^6$ N/mm^2 and Poisson's ratio $\nu = 0.3125$. Both single loads are $F = 40.0$KN. Due to the specific boundary conditions the structure undergoes large rotations, involving both membrane and bending responses. Some authors have investigated this problem on solid-shell and shell elements with different mesh arrangements (8×12, 16×24, 20×30, 24×36). As examples, see references [120, 3, 140] for solid-shell and [141, 67] for shells. All cited references have addressed large deformation.

In the current work, meshes of 8×12, 16×24 are used to model one octant of the cylinder. The displacements U_Z^A, U_X^B and U_X^C are plotted in Figure 6.21(c). SC8R element of ABAQUS with 64×64 elements, which is a 3D continuum element, is used as the reference solutions. The reason of this selection is the 3D geometry of SC8R, which is analogous to the solid-shell of the current work.

The results in Figure 6.21(c) show that the response has two regimes: a) a primary stage dominated by bending effects and characterized by large rotations. At this stage, the struc-

Table 6.21: Example 18 — Stretching of a cylinder, Iterations for the first 10 increments

No of Increments	No. of Iterations									
7	5	6	6	8	8	11	14	-	-	-
60	3	3	3	3	3	3	3	4	4	3

ture is stretched uniformly until the load reaches the value of $F = 21.0$KN. b) secondary phase dominated by membrane effects characterized by large deformational displacements. At this phase a snap through takes place and the structures exhibits an abrupt increase of the displacements. Using coarse mesh (8×12), the snap through occurs at the same load level as the reference solution and the displacement of point **A** at load $F = 40.0$KN is 0.950 of the reference displacement, which proves that ANDES is performing satisfactorily to alleviate the membrane locking. Using a mesh arrangement of 16×24, the displacement of point **A** at load level $F = 40.0$KN is 0.994 of the reference solution. As reported in reference [140], the computed Green strains at the maximum load level are in order of 10%, which fall in the context of large deformations.

Using the present formulation, the accurate results are achieved by only 7 equal increments, nonetheless, in order to display smooth curves, 60 equal increments are applied for plotting. The number of corrector iterations for the first ten increments are presented in Table 6.21. The deformed finite element mesh at the maximum load value is shown in Figure 6.21(b).

6.2.12 Example 19: Clamped-hinged deep circular arch subjected to a concentrated load

In this problem a deep circular arch undergoes a point load at its apex as is shown in Figure 6.22(a). The radius of the arch is $R = 100$mm, the thickness is $t = 1$mm and the width is $w = 24$mm. The structure is hinged at one end and fixed at the other end, this allows for non-symmetric buckling. The material behavior is modeled as isotropic linear

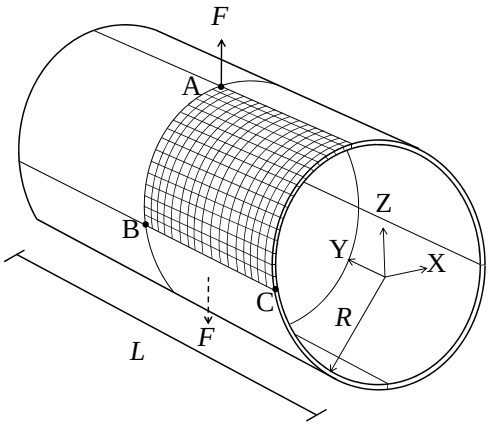

(a) Geometry

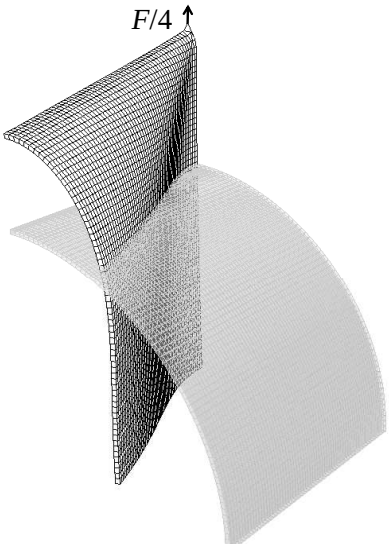

(b) Deformed shape

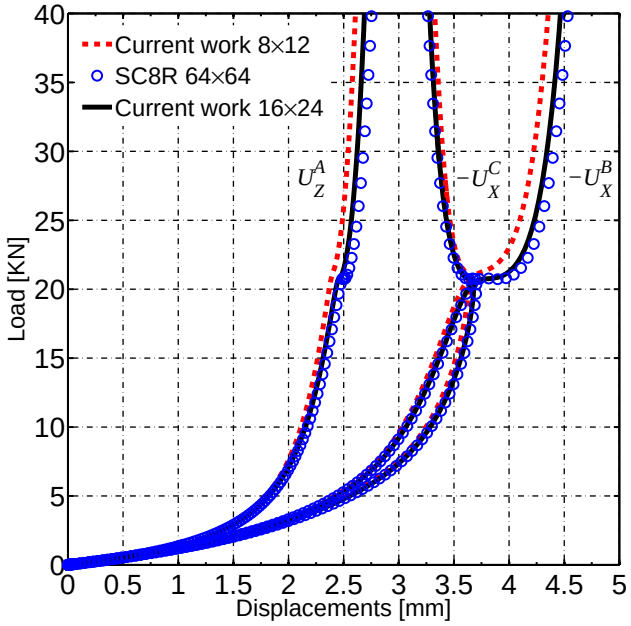

(c) Load-displacement curves for points A,B and C

Figure 6.21: Example 18 — Stretching of a cylinder with free ends

elastic with Young's modulus $E = 0.5 \times 10^5$ N/mm^2 and Poisson's ratio $\nu = 0.0$. The total load value applied on the apex is $F = 1000$N. This example has been addressed in references [3, 83]. Due to the lack of symmetry, the entire structure is modeled with mesh of 40×1 following the cited references. In Figure 6.22(c), the horizontal (U_X) and vertical (U_Y) displacements of the point under the load is plotted versus the incremental load and the results are compared with SHB8PS in reference [3]. For this problem, 50 equal increments are used to produce the response curve. The schematic deformed shape of the arch is shown in Figure 6.22(b).

The response of current solid-shell element with corotational kinematics conforms with that of cited element with Updated-Lagrangian kinematic description, however, the plot shows that the post-buckling regime starts slightly later than the cited element (at load value of F= 990N compared to F= 950N for SHB8PC in [3]).

6.2.13 Example 20: Twisted beam under out-of-plane loading

In this test, the performance of the nonlinear formulation is assessed in case of warped geometry. The geometric and material parameters as well as the boundary conditions are the same as example 5.1.6. The geometry is shown in Figure 6.16(b). An out-of-plane load with magnitude of $F = 60$N is applied at the free end of the beam (point **A**). The version of this problem with $t = 0.032$mm has been investigated in the literature ([3, 136]). In this example, the twisted beam with thickness $t = 0.05$mm is investigated since the convergence study of the linear formulation is presented for the beam with the same thickness.

Different mesh arrangements have been used by authors such as 12×2, 24×4 and 48×4. Here, a 24×4 mesh is considered. The SC8R of ABAQUS with mesh of 96×8 is chosen as the reference solution. The maximum load is applied in 15 equal increments.

The displacements U_X, U_Y and U_Z of the point **A** are plotted versus the load in Figure 6.23(b) along with the reference solution. The solid-shell with intermediate mesh refinement, considering the CR kinematics, has an excellent agreement with the reference solution

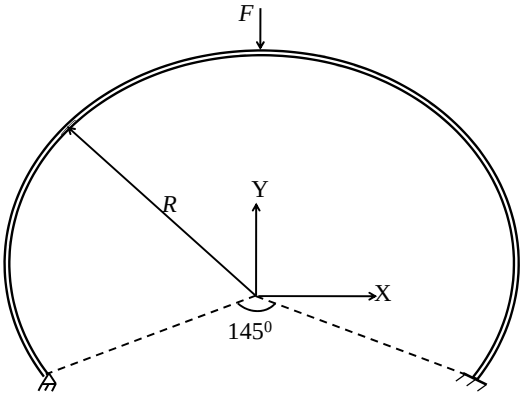

(a) Geometry

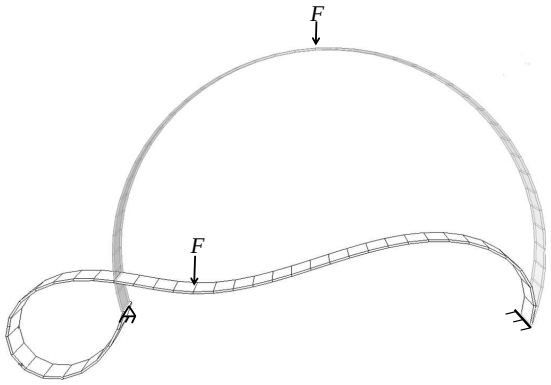

(b) Deformed shape

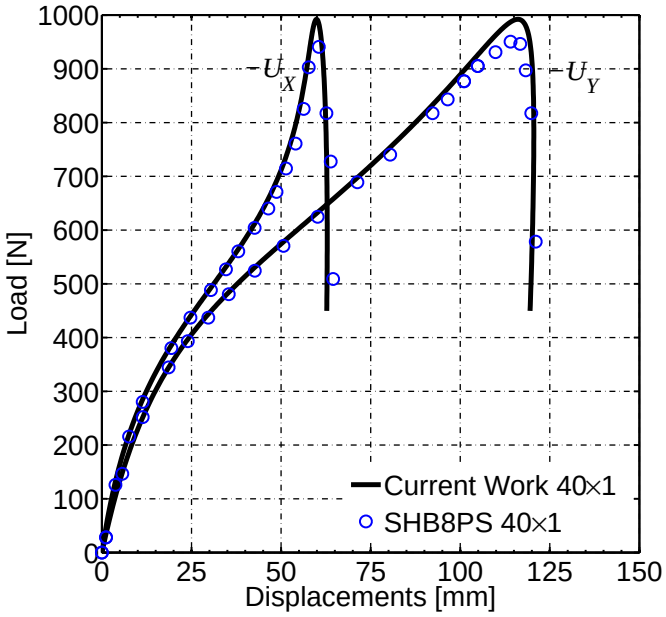

(c) Load-displacement curves for point under the load

Figure 6.22: Example 19 — Clamped-hinged deep circular arch subjected to a concentrated load

(SC8R) considering UL kinematics with a fine mesh arrangement. The deformed shape of the twisted beam is shown in Figure 6.23(a).

It is noted that, in case of a coarse mesh arrangement (6×1), the structure becomes stiff and the results diverge from the reference solution for large displacements, even though the linear problem shows an excellent agreement with the analytical solution for coarse mesh. This locking problem in gemotrically nonlinear example is due to the fact that when the solid-shell element is too warped, the corotational frame is not optimum, i.e. considering a frame that travels with the mid-surface is not an optimum frame.

6.2.14 Example 21: Slit annular plate subjected to lifting line force

This test is another benchmark to assess the performance of the thin shell structures under finite rotations. It was first proposed in [13, 14] and then adopted by many other authors [3, 141, 136]. The internal and external radii of the structure are $R_i = 6$mm and $R_e = 10$mm respectively. The shell thickness is $t = 0.03$mm. The material behavior is modeled as isotropic linear elastic with Young's modulus $E = 21 \times 10^6$ N/mm^2 and Poisson's ratio $\nu = 0.0$.

The undeformed geometry of the structure is shown in Figure 6.24(a). The circular ring has a slit cut along the radial direction A-B, where a vertical lifting line force $F = 0.8$N/mm is applied on one edge of the slit, and the other edge is fully clamped. Different mesh arrangements have been used in literature such as 6×48, 8×64 and 10×80 with only one element across the thickness. In reference [141] this problem has been investigated with two meshes of 6×30 and 10×80 using S4R shell element, hence, this reference is selected to compare the results. Following reference [3], in the current work, the intermediate mesh of 8×64 is used. 20 equal increments are used to plot the response curve, however, the same results are achieved by only 10 increments.

The vertical displacements of points **A** and **B** are plotted versus the load multiplier λ in Figure 6.24(c) along with the results for the reference solution. The results of solid-shell

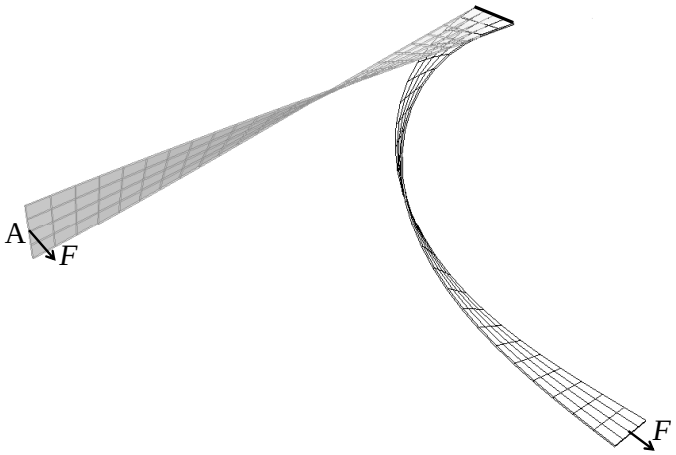

(a) Deformed shape

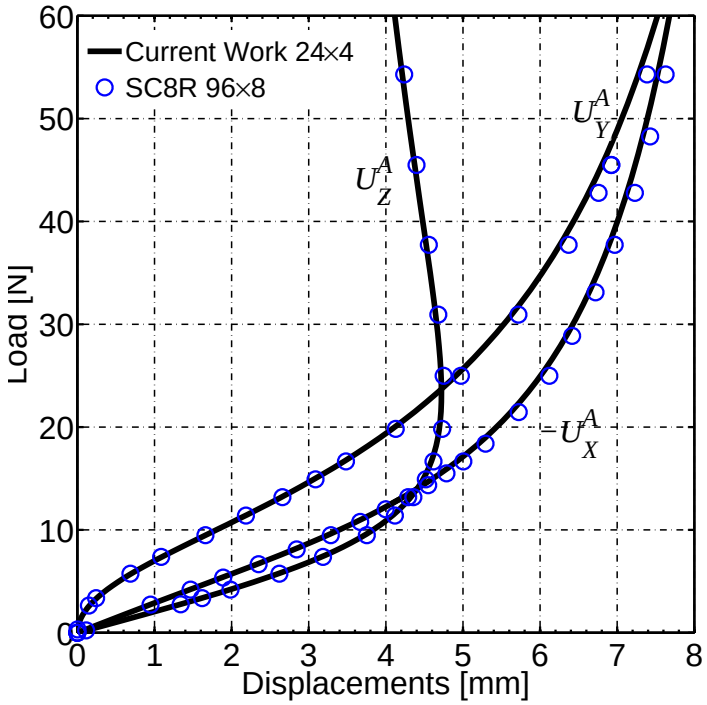

(b) Load-displacement curves for point **A**

Figure 6.23: Example 20 — Twisted Beam under out-of-plane loading (Geometrically non-linear problem)

formulation with CR kinematics conform with the reference solution of ABAQUS with UL kinematic description. The deformed shape of the ring is also shown in Figure 6.24(b), which shows the large displacement and rotation of the free edge.

6.2.15 Example 22: Hinged cylindrical shell under concentrated load

The hinged cylindrical shell subjected to a concentrated load is another common test to assess the path following algorithm. The geometric data are as: Radius $R = 2540$mm, the length $L = 508$mm and the angle $\theta = 0.1$rad. Due to symmetry only a quarter of the structure is modeled as shown in Figure 6.25(a).

Two versions of the problem are investigated in the literature. References [9, 4, 41] analyzed a thin shell with the thickness of $t = 6.35$mm and reference [86] considered a thick shell with the thickness of $t = 12.70$mm. Some authors investigated both cases [120, 82, 141, 130]. In this work the thin shell is taken into account, which is a more challenging problem.

The material behavior is modeled as isotropic linear elastic with Young's modulus $E = 3102.75$ N/mm^2 and Poisson's ratio $\nu = 0.3$. The total load applied on point **A** reaches the value of $F = 800$N.

In reference [141], this problem has been investigated with S4R shell of ABAQUS with meshes of 16×16 and 24×24 elements. The coarsest mesh that has been used for this example in literature is 4×4 as could be found in references [119, 130]. In this work, the model is discretized by the same mesh arrangement. The results are compared with S4R with 64×64 elements (reference solution) and Q1STs with 4×4 elements. Following the cited references for solid-shells, in order to simulate the hinged support, the thickness is discretized with two elements, which allows to fix the nodes of the mid-plane at the edge (U_X=U_Y=U_Z=0).

The vertical displacements of points **A** and **B** versus the incremental load is plotted in Figure 6.25(c). The current solid-shell is slightly more flexible than the reference solution after the snap-back occurs, however, in general, the results have good agreements with the reference solutions. The maximum load is reached by 15 equal increments, however, to produce the results in Figure 6.25(c), 50 increments are used. In this example both symmetrized and

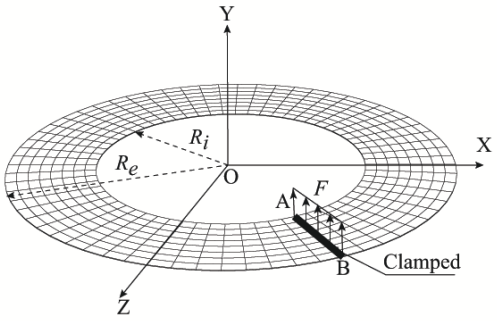

(a) Geometry

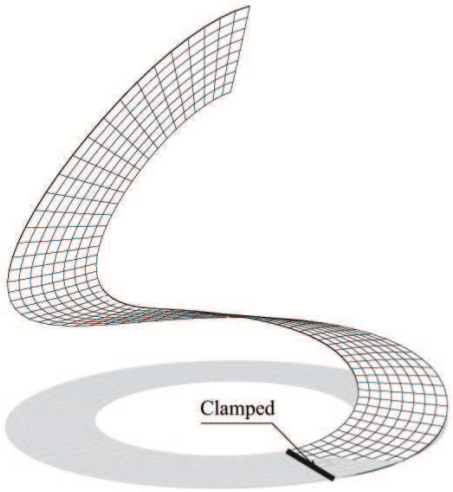

(b) Deformed shape

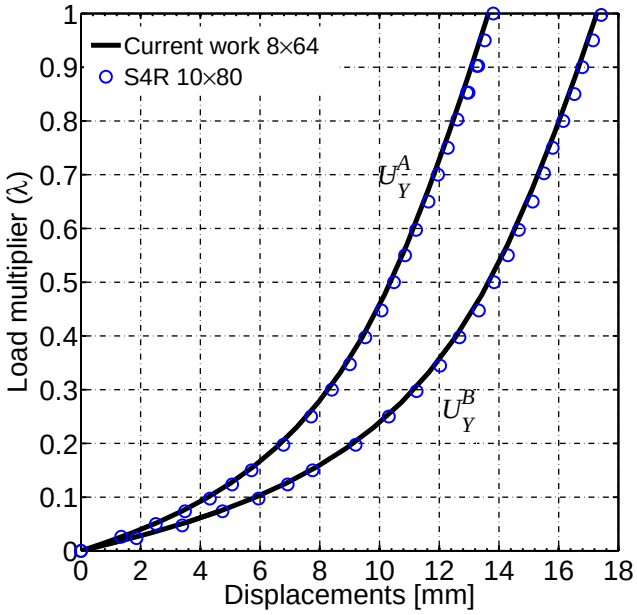

(c) λ-displacement curves for points A and B

Figure 6.24: Example 21 — Slit annular plate subjected to lifting line force

Table 6.22: Example 22 — Hinged cylinder problem case 2 layers, Euclidean norm of the force residual vector for corrector iterations, unsymmetric stiffness matrix (Arc length=15)

Unsymmetric			Increments		
Iteration	1	4	7	11	15
1	23216.743	9761.246	14231.813	18395.300	15945.004
2	77.696	545.538	121.114	568.035	33.166
3	7.113	69.277	17.690	368.732	0.726
4	1.862×10^{-4}	0.266	5.152×10^{-3}	3.243	7.241×10^{-7}
5	1.823×10^{-8}	2.586×10^{-5}	3.368×10^{-8}	3.896×10^{-3}	4.213×10^{-10}
6		2.424×10^{-8}		3.180×10^{-8}	

unsymmetric stiffness matrices are taken into account and the results are compared. Considering 15 increments, the convergence of the Euclidean norm of the force residual vector are listed in Tables 6.22 and 6.23 for unsymmetric and symmetrized stiffness matrices respectively. It is observed in these tables that the results are identical for both symmetrized and unsymmetric stiffness matrices and whether or not the stiffness matrix is symmetric does not affect the convergence of the solution.

Following the work of Legay and Combesure [86] who investigated the sensitivity of the results to the boundary conditions for the thick shell (t= 12.70mm), in this work, the lower side edge of the thin shell (t= 6.35mm) is hinged to investigate the sensitivity of the results to the boundary conditionas as shown in Figure 6.25(b). The model is discretized by 4×4×1 elements. In Figure 6.25(d), the displacements of point **A** versus the incremental load is plotted along with the results for SC8R of ABAQUS with the mesh of 32×32×1 (as reference solution). The snap-back response vanishes and the structure undergoes larger deformations comparing to when the mid-plane is hinged. In general, the results of current work reasonably conforms with the reference solution.

6.3 ANS-EAS Solid-shell element

In this section, the performance of the second proposed geometrically linear solid-shell element formulation is assessed against some of the well-known benchmarks and the results

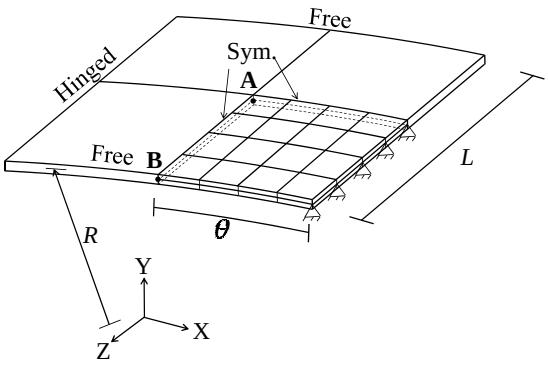

(a) Geometry, case two layers

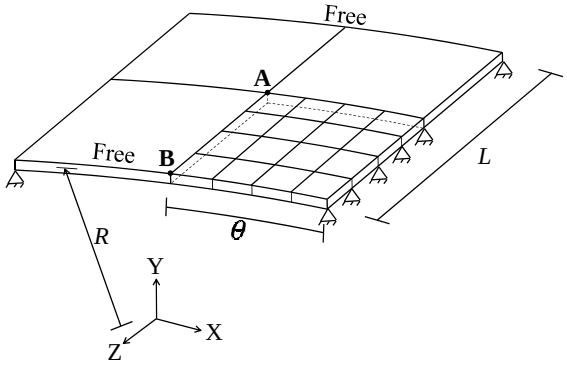

(b) Geometry, case one layer

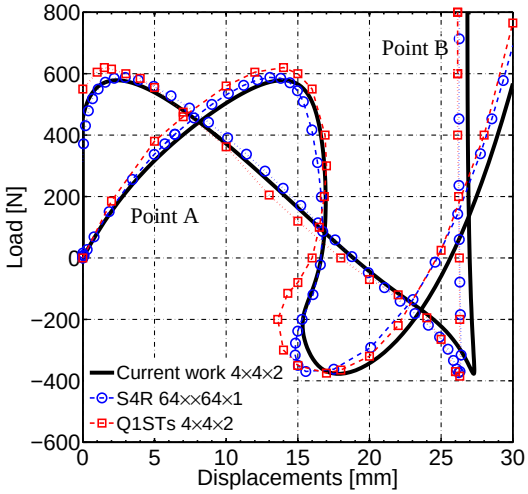

(c) vertical displacements of points A and B, case two layers

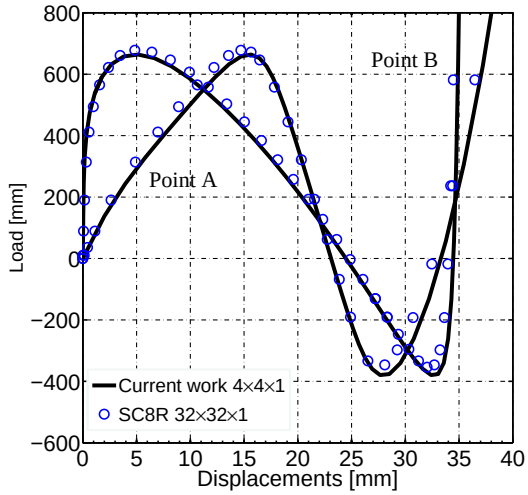

(d) vertical displacements of point A, case one layer

Figure 6.25: Example 22 — Hinged cylinder problem (thin shell)

Table 6.23: Example 22 — Hinged cylinder problem case 2 layers, Euclidean norm of the force residual vector for corrector iterations, symmetric stiffness matrix (Arc length=15)

Symmetric			Increments		
Iteration	1	4	7	11	15
1	23216.743	9761.058	14231.762	18395.189	15944.914
2	77.695	545.185	121.084	568.091	33.176
3	7.113	69.245	17.685	368.787	0.726
4	1.869×10^{-4}	0.266	5.138×10^{-3}	3.243	7.621×10^{-7}
5	2.408×10^{-8}	2.630×10^{-5}	5.471×10^{-8}	3.905×10^{-3}	5.128×10^{-10}
6		2.317×10^{-8}		4.077×10^{-8}	

are compared to those of the first proposed formulation. It is noted that in many numerical examples presened before, both elements produce similar results, thus only the examples for which the two formulations yield different results are presented here.

6.3.1 Example 23: Pinched cylinder with end diaphragms

Table 6.24 represents the convergence of both solid-shell formulations with regular mesh arrangements as shown in example 6.2.2.

Sensitivity to mesh distortion: Using the same mesh arrangment as 6.2.2, the sensitivity of the results to the mesh distortion is presented in Table 6.25.

It is seen that the first solid-shell element is less sensitive to mesh distortion and converges slightly faster than the second proposed formulation.

Table 6.24: Example 23 — Pinched cylinder with end diaphragms, normalized displacement of point under the load.

Element			n_e			
Type	4×4	8×8	12×12	16×6	20×20	32×32
ANS-ANDES-EAS	0.393	0.763	0.905	0.949	0.970	0.999
ANS-EAS	0.360	0.698	0.898	0.938	0.965	0.998

Table 6.25: Example 23 —pinched cylinder(distorted mesh), Normalized displacement of the point under the load

Element Type	Angle $\theta = 0^o$	$\theta = 10^o$	$\theta = 20^o$	$\theta = 30^o$	$\theta = 40^o$
ANS-ANDES-EAS	0.970	0.963	0.926	0.925	0.924
ANS-EAS	0.965	0.962	0.924	0.925	0.915

6.3.2 Example 24: Cook's skew beam problem

Table 6.26 illustrates the convergence of both solid-shell formulations for cook's skew plate problem as described in 6.2.8.

It is observed tht the second solid-shell formulation converges to the analytical solution faster than the first proposed formulation.

6.3.3 Example 25: Clamped square plate

Table 6.27 illustrates the sensitivty of the results to mesh distortion for clamped square plate examlpe as described in 6.2.7.

It can be seen that the first proposed solid-shell formulation is less sensitive to the mesh distortion.

Other numerical examples for geometric linear problems were also tested on the second proposed formulation, but the results are not presented here since they are similar to those of the first solid-shell formulation.

Table 6.26: Example 24 — Cook's skew beam problem, vertical displacement of point **A**.

Element Type	n_e 2×2	4×4	8×8	16×6
ANS-ANDES-EAS	21.46	22.84	23.64	23.89
ANS-EAS	22.84	23.43	23.79	23.91

Table 6.27: Example 25 — Clamped square plate, Normalized displacement of point **A**.

Element Type	e 0	2	4	6	8	10	12
ANS-ANDES-EAS	0.881	0.871	0.861	0.841	0.811	0.771	0.711
ANS-EAS	0.857	0.854	0.844	0.826	0.797	0.754	0.688

Chapter 7

Conclusions

7.1 Summary of the work

In chapter 2, a computational approach has been described for combined material and geometrically nonlinear analysis by the Finite Element Method. Its main advantage is reuse: once a finite element has been developed with good performance in linear analysis, extension to material and geometrically nonlinear problems is simplified. Extension to geometrically nonlinear problems is enabled by a corotational kinematic description, and that to material nonlinear problems by an optimization-based solution algorithm. The corotational formulations allows elements that perform well in geometrically linear problems to be extended to nonlinear problems in an element independent manner. The optimization-based approach removes the need for the implementation of a model-specific return mapping scheme. In this work plane stress problems in the large displacement-small strain regime are considered, as is the case in elasto-plastic buckling problems.

The ANDES linear quadrilateral element, chosen here as the linear element passes the uniform strain patch test and shows excellent convergence characteristics in other well-known benchmark problems. Furthermore, numerical results obtained using the linear ANDES element are consistent with the proof by MacNeal [91] that a 4-node quadrilateral element with two degrees of freedom per node either fails to pass the constant strain/stress patch test, or locks in in-plane bending in case of distorted mesh. In nonlinear problems, the low order element developed here has comparable performance to a higher order displacement element

with total Lagrangian kinematics.

In chapter 3, an eight-node solid-shell formulation based on ANS, ANDES and EAS concepts is presented. The in-plane response is separated from the out-of-plane response. This separation gives the freedom of selecting any type of membrane quadrilateral element for the in-plane response. The element geometry is transformed into a local frame to make the finite elements independent of the node numbering.

ANDES concept is used to model the in-plane response. Since the ANDES scheme is applied on the warped mid-surface, rigid body modes produce nonzero in-plane strains. The projection method has been used to depollute the in-plane stiffness matrix and make the internal forces self equilibrating.

In order to circumvent the transverse shear locking and curvature locking in thickness direction, the ANS concept has been used. ANS concept has proven to be more effective in alleviating the shear locking problem than other methods introduced in literature, such as EAS.

EAS concept with only one extra degree of freedom has been used to alleviate the volumetric and Poisson thickness locking problems at the element level.

In chapter 4, an eight-node solid-shell element based on ANS and EAS approaches is presented. ANS concept is implemented to account for the transverse shear and thickness strains, which has proven to circumvent the curvature thickness and transverse shear locking problems. EAS approach based on the Hu-washizu variational principle with six EAS degrees-of-freedom is applied. Five extra Degrees-of-freedom are applied on the in-plane strains (e_{xx},e_{yy} and γ_{xy}) to improve the element response for in-plane loadings and one on the thickness strain so as to alleviate the Poisson's thickness locking. In the numerical examples chapter, both linear element formulations have been assessed by a number of famous benchmarks proposed for shell-like finite elements. Both element formulations pass the patch test. Moreover, both elements' performances have been tested for mesh distortion, warped

mesh arrangement, single and doubly curved structures. It was evident from the pinched cylinder example with end diaphragms that the thickness tapered element has poor convergence rate for inextensional bending problems, however, the pinched cylinder example shows that both linear element formulations have higher convergence rates compared to other cited shell and solid-shell formulations.

EICR approach, which was also used in 2D formulation, is used to take the geometric nonlinearity into account. Rigid body rotations are filtered out by projectors. The corotated frame is defined such that it is independent of whether the mid-surface is warped or not. It is noted that the proposed nonlinear formulation has all the requirements of the CR formulation such as: equilibrium, consistency, invariance, symmetrizability and element independence as explained in the text.

The nonlinear element has been subjected to different benchmarks involving geometric nonlinear effects, bifurcation-type, snap-through and snap-back instabilities. The numerical results prove that in the context of small strains, considering similar mesh arrangements, the present formulation with CR kinematic description works as well as the other nonlinear elements with UL or TL kinematic descriptions in terms of the rate of convergence to the reference solutions.

7.2 Directions for further research

7.2.1 Computational approach for the combined material and geometrically nonlinear analysis

The explicit update of the geometry in equation (2.19) results in the need for small time increments near the peak. For instance, in the buckling problem 6.1.5, since the geometry is updated explicitly, there is a jump in the force-displacement curve at the buckling threshold,

when the time increments are large. Improving this issue is a topic for further research. ANDES element, which is an instance of the Templates, introduced by Professor Felippa, passes the constant-strain patch test, but still requires to be improved in terms of sensitivity to mesh distortion when it is subjected to in-plane shear loads (MacNeal's thin beam problem).

7.2.2 Solid-shell formulation

The two presented solid-shell elements, which are suitable for problems with small strains, could be extended to address large deformations. There are two possibilities as to extend them to problems with large deformations as below:

- Keeping the linear element libraries and extend the EICR approach to large deformations following the work of Rankin [114].
- Extending the element formulations to large deformations using TL or UL kinematic descriptions, which have been addressed by some authors in different ways.

The first method, mentioned above, has the advantage of using the linear element library as explained for the small strain case. This method could be applied to both proposed linear formulations described in chapters 3 and 4. The second method is more suitable for the second proposed element formulation of chapter 4.

Extension of both presented solid-shell formulations to materially nonlinear behavior such as elasto-plasticity, fracture mechanics, multi-scale and multi-physics problems, are also possible and the subjects for further research.

Bibliography

[1] ABAQUS. ABAQUS theory and manuals, 2010.

[2] F. Abed-Meraim and A. Combescure. SHB8PS-a new adaptative, assumed-strain continuum mechanics shell element for impact analysis. Computers and Structures, 80(9-10):791–803, 2002.

[3] Farid Abed-Meraim and Alain Combescure. An improved assumed strain solid-shell element formulation with physical stabilization for geometric non-linear applications and elastic-plastic stability analysis. International Journal for Numerical Methods in Engineering, 80(13):1640–1686, 2009.

[4] R. J. Alves de Sousa, R. P. R. Cardosa, R. A. Fontes Valente, J. W. Yoon, J. J. Grácio, and R. M. Natal Jorge. A new one-point quadrature enhanced assumed strain (EAS) solid-shell element with multiple integration points along thickness - part II: Nonlinear applications. International Journal for Numerical Methods in Engineering, 67(2):160–88, 2006.

[5] R. J. Alves de Sousa, R. P. R. Cardoso, R. A. Fontes Valente, J. W. Yoon, J. J. Grácio, and R. M. Natal Jorge. A new one-point quadrature enhanced assumed strain (EAS) solid-shell element with multiple integration points along thickness: Part 1-Geometrically linear applications. International Journal for Numerical Methods in Engineering, 62(7):952–77, 2005.

[6] R. J. Alves de Sousa, R. M. Natal Jorge, R. A. Fontes Valente, and J. M. A. Ćesar de Sá. A new volumetric and shear locking-free 3D enhanced strain element. Engineering Computations, 20(7):896–925, 2003.

[7] R. J. Alves de Sousa, J. W. Yoon, R. P. R. Cardoso, R. A. Fontes Valente, and J. J. Grácio. On the use of a reduced enhanced solid-shell (RESS) element for sheet forming simulations. International Journal of Plasticity, 23(3):490–515, 2007.

[8] U. Andelfinger and E. Ramm. EAS-elements for two-dimensional, three-dimensional, plate and shell structures and their equivalence to HR-elements. International Journal for Numerical Methods in Engineering, 36(8):1311–1337, 1993.

[9] P. M. A. Areias, J. M. A. Ćesar de Sá, C. A. Conceicão António, and A. A. Fernandes. Analysis of 3D problems using a new enhanced strain hexahedral element. International Journal for Numerical Methods in Engineering, 58(11):1637–82, 2003.

[10] J. H. Argyris. Continua and discontinua. Proceedings of the first conference on matrix mathods in structural mechanics, Ohio, US, 1965. Air force institute of technology. AFFDL-TR-66-80.

[11] J. H. Argyris, H. Balmer, J. St Doltsinis, P. C. Dunne, M. Haase, M. Kleiber, G. A. Malejannakis, H. P. Mlejnek, M. Muller, and D. W. Scharpf. Finite element method — the natural approach. Computer Methods in Applied Mechanics and Engineering, 17-18:1–106, 1979.

[12] F. Armerot and A. Perez-Foguet. On the formulation of closest-point projection algorithms in elastoplasticity. I. The variational structure. International Journal for Numerical Methods in Engineering, 53(2):297–329, 2002.

[13] Y. Basar and Y. Ding. Finite-rotation elements for the non-linear analysis of thin shell structures. International Journal of Solids and Structures, 26(1):83–97, 1990.

[14] Y. Basar and Y. Ding. Finite-rotation shell elements for the analysis of finite-rotation shell problems. volume 34 of Int. J. Numer. Methods Eng. (UK), pages 165–9, UK, 1992.

[15] K. J. Bathe. The inf-sup condition and its evaluation for mixed finite element methods. Computers and Structures, 79(2):243–52, 2001.

[16] K. J. Bathe and E. N. Dvorkin. On the automatic solution of nonlinear finite element equations. volume 17 of Comput. Struct. (UK), pages 871–9, UK, 1983.

[17] K. J. Bathe and E. N. Dvorkin. A four-node plate bending element based on Mindlin/Reissner plate theory and a mixed interpolation. International Journal for Numerical Methods in Engineering, 21(2):367–83, 1985.

[18] K. J. Bathe and E. L. Wilson. Numerical methods in finite element analysis. Prentice-Hall, Englewood Cliffs, N.J., 1976.

[19] Klaus-Jrgen Bathe. Finite element procedures. Prentice Hall, Englewood Cliffs, N.J., 1996.

[20] Klaus Juergen Bathe and Arthur P. Cimento. Some practical procedures for the solution of nonlinear finite element equations. Computer Methods in Applied Mechanics and Engineering, 22(1):59–85, 1980.

[21] J. M. Battini. A modified corotational framework for triangular shell elements. Computer Methods in Applied Mechanics and Engineering, 196(13-16):1905–14, 2007.

[22] J. M. Battini. A non-linear corotational 4-node plane element. Mechanics Research Communications, 35(6):408–13, 2008.

[23] T. Belytschko and B. J. Hsieh. Non-linear transient finite element analysis with convected co-ordinates. International Journal for Numerical Methods in Engineering, 7(3):255–71, 1973.

[24] T. Belytschko, J. I. Lin, and C. S. Tsay. Explicit algorithms for the nonlinear dynamics of shells. Computer Methods in Applied Mechanics and Engineering, 42(2):225–51, 1984.

[25] T. Belytschko and W. K. Liu. Test problems and anomalies in shell finite elements. Reliability of Methods for Engineering Analysis. Proceedings of the International Conference, pages 393–406, Swansea, UK, 1986. Pineridge Press.

[26] T. Belytschko, W. K. Liu, and Brian Moran. Nonlinear Finite Elements for Continua and Structures. John Wiley and Sons, 2007.

[27] Ted Belytschko and Lee P. Bindeman. Assumed strain stabilization of the eight node hexahedral element. Computer Methods in Applied Mechanics and Engineering, 105(2):225–260, 1993.

[28] P. G. Bergan. Finite elements based on energy orthogonal functions. International Journal for Numerical Methods in Engineering, 15(10):1541–1555, 1980.

[29] P. G. Bergan and L Hansen. A new approach for deriving 'good' finite elements. In J. R. Whiteman, editor, The mathematics of finite elements and applications, volume II, pages 483–497. Academic Press, London, 1976.

[30] P. G. Bergan, G. Horrigmoe, B. Krakeland, and T. H. Soreide. Solution techniques for non-linear finite element problems. International Journal for Numerical Methods in Engineering, 12(11):1677–96, 1978.

[31] P. G. Bergan and M. K. Nygard. Finite elements with increased freedom in choosing shape functions. International Journal for Numerical Methods in Engineering, 20(4):643–663, 1984.

[32] P. Betsch, F. Gruttmann, and E. Stein. A 4-node finite shell element for the implementation of general hyperelastic 3D-elasticity at finite strains. Computer Methods in Applied Mechanics and Engineering, 130(1-2):57–79, 1996.

[33] P. Betsch and E. Stein. An assumed strain approach avoiding artificial thickness straining for a non-linear 4-node shell element. Communications in Numerical Methods in Engineering, 11(11):899–909, 1995.

[34] M. Bischoff and E. Ramm. Shear deformable shell elements for large strains and rotations. International Journal for Numerical Methods in Engineering, 40(23):4427–49, 1997.

[35] M. Bischoff and E. Ramm. Shear deformable shell elements for large strains and rotations. International Journal for Numerical Methods in Engineering, 40(23):4427–49, 1997.

[36] J. F. Bonnans. Numerical optimization : Theoretical and practical aspects. Springer, Berlin ; New York, 2nd edition, 2006.

[37] R. P. R. Cardoso and Jeong-Whan Yoon. One point quadrature shell element with through-thickness stretch. Computer Methods in Applied Mechanics and Engineering, 194(9-11):1161–99, 2005.

[38] R. P. R. Cardoso, Jeong-Whan Yoon, and R. A. Fontes Valente. A new approach to reduce membrane and transverse shear locking for one-point quadrature shell elements: Linear formulation. International Journal for Numerical Methods in Engineering, 66(2):214–49, 2005.

[39] R. P. R. Cardoso, Jeong-Whan Yoon, J. J. Grácio, F. Barlat, and J. M. A. Ćesar de Sá. Development of a one point quadrature shell element for nonlinear applications with contact and anisotropy. Computer Methods in Applied Mechanics and Engineering, 191(45):5177–206, 2002.

[40] Rui P. R. Cardoso and Jeong-Whan Yoon. One point quadrature shell elements: A study on convergence and patch tests. Computational Mechanics, 40(5):871–883, 2007.

[41] Rui P. R. Cardoso, Jeong-Whan Yoon, M. Mahardika, S. Choudhry, R. J. Alves de Sousa, and R. A. Fontes Valente. Enhanced assumed strain (EAS) and assumed natural strain (ANS) methods for one-point quadrature solid-shell elements. International Journal for Numerical Methods in Engineering, 75(2):156–187, 2008.

[42] J. M. A. Ćesar de Sá, R. M. Natal Jorge, R. A. Fontes Valente, and P. M. Almeida Areias. Development of shear locking-free shell elements using an enhanced assumed strain formulation. International Journal for Numerical Methods in Engineering, 53(7):1721–50, 2002.

[43] A. Chatterjee. An introduction to the proper orthogonal decomposition. Current Science, 78(7):808–17, 2000.

[44] Norman Connacher, M. McElroy, Hansen, and D. Stanley. SAMECS structural analysis system (user's document, http://trove.nla.gov.au/work/24516893), 1969.

[45] RD Cook, DS. Malkus, and ME. Plesha. Concepts and applications of finite element analysis. John Wiley and Sons, New York, 3rd edition, 1989.

[46] Nelvio Dal Cortivo, Carlos A. Felippa, Henri Bavestrello, and William T. M. Silva. Plastic buckling and collapse of thin shell structures, using layered plastic modeling and co-rotational ANDES finite elements. Computer Methods in Applied Mechanics and Engineering, 198(5-8):785–798, 2009.

[47] J. K. Coultate, C. H. J. Fox, S. McWilliam, and A. R. Malvern. Application of optimal and robust design methods to a MEMS accelerometer. Sensors and Actuators: A. Physical, 142(1):88–96, 2008.

[48] M. A. Crisfield. A fast incremental/iterative solution procedure that handles 'snap-through'. Computers and Structures, 13(1-3):55–62, 1981.

[49] M. A. Crisfield and G. F. Moita. A co-rotational formulation for 2-D continua including incompatible modes. International Journal for Numerical Methods in Engineering, 39(15):2619–33, 1996.

[50] Eduardo N. Dvorkin and Klaus-Juergen Bathe. Continuum mechanics based four-node shell element for general non-linear analysis. Engineering Computations, 1(1):77–88, 1984.

[51] R. Febres, P. Inglessis, and J. Florez-Lopez. Modeling of local buckling in tubular steel frames subjected to cyclic loading. Computers and Structures, 81(22-23):2237–47, 2003.

[52] C. A. Felippa. Survey of parametrized variational principles and applications to computational mechanics. Technical report, 1993.

[53] C. A. Felippa. Supernatural QUAD4: A template formulation. Computer Methods in Applied Mechanics and Engineering, 195(41-43):5316–42, 2006.

[54] C. A. Felippa. Three dimensional linear elastostatics (course notes), 2011. available at `http://www.colorado.edu/engineering/CAS/courses.d/AFEM.d/AFEM.Ch05.d/AFEM.Ch05.pdf`.

[55] C. A. Felippa. The SS8 solid shell element, a Fortran implementation, March 2002.

[56] C. A. Felippa and K. C. Park. Fitting strains and displacements by minimizing dislocation energy. International Conference on Computational Structures Technology - Proceedings, pages 49–50, Prague, Czech republic, 2002. Civil Comp Limited.

[57] Carlos A. Felippa and Bjorn Haugen. A unified formulation of small-strain corotational finite elements: I. Theory. Computer Methods in Applied Mechanics and Engineering, 194(21-24 SPEC. ISS.):2285–2335, 2005.

[58] Carlos A. Felippa and Carmelo Militello. Membrane triangles with corner drilling freedoms - II. The ANDES element. Finite elements in analysis and design, 12(3-4):189–201, 1992.

[59] R. A. Fontes Valente, R. J. Alves De Sousa, and R. M. Natal Jorge. An enhanced strain 3D element for large deformation elastoplastic thin-shell applications. Computational Mechanics, 34(1):38–52, 2004.

[60] B. Fraeijs de Veubeke. The dynamics of flexible bodies. International Journal of Engineering Science, 14(10):895–913, 1976.

[61] B. M. Fraeijs de Veubeke. Displacement and equilibrium models, in stress analysis. Int. J. Numer. Meth. Engrg, 52:287342, 2001.

[62] Isaac Fried. Orthogonal trajectory accession to the nonlinear equilibrium curve. Computer Methods in Applied Mechanics and Engineering, 47(3):283–297, 1984.

[63] M. Ghassemieh and A. R. Kukreti. Algorithm for the analysis of problems with combined material and geometric nonlinearities. Computers and Structures, 35(5):579–591, 1990.

[64] R. Glowinski and Patrick Le Tallec. Augmented Lagrangian and operator-splitting methods in nonlinear mechanics. Society for Industrial and Applied Mathematics, Philadelphia, 1989.

[65] F. Gruttmann and W. Wagner. A linear quadrilateral shell element with fast stiffness computation. Computer Methods in Applied Mechanics and Engineering, 194(39-41):4279–300, 2005.

[66] Bernard Halphen and Son Nguyen Quoc. On generalized standard materials sur les materiaux standards generalises. Journal de Mecanique, 14(1):39–63, 1975.

[67] S. C. Han, K. D. Kim, and W. Kanok-Nukulchai. An element-based 9-node resultant shell element for large deformation analysis of laminated composite plates and shells. Structural Engineering and Mechanics, 18(6):807–29, 2004.

[68] Bjorn Haugen. Buckling and Stability problems for thin shell Structures using High Performance Finite Elements. PhD thesis, Colorado At Boulder, 1994.

[69] R. Hauptmann and K. Schweizerhof. Systematic development of 'solid-shell' element formulations for linear and non-linear analyses employing only displacement degrees of freedom. International Journal for Numerical Methods in Engineering, 42(1):49–69, 1998.

[70] R. Hauptmann, K. Schweizerhof, and S. Doll. Extension of the solid-shell concept for application to large elastic and large elastoplastic deformations. International Journal for Numerical Methods in Engineering, 49(9):1121–41, 2000.

[71] L. R. Herrmann. Elasticity equations for nearly incompressible materials by a variational theorem. AIAA J., 3:18961900, 1965.

[72] T. J. R. Hughes and T. E. Tezduyar. Finite elements based upon Mindlin plate theory with particular reference to the four-node bilinear isoparametric element. Transactions of the ASME. Journal of Applied Mechanics, 48(3):587–96, 1981.

[73] Thomas J. R. Hughes. Generalization of selective integration procedures to anisotropic and nonlinear media. International Journal for Numerical Methods in Engineering, 15(9):1413–1418, 1980.

[74] Thomas J. R. Hughes. The Finite Element Method : Linear static and dynamic finite element analysis. Dover Publications, Mineola, NY, 2000.

[75] Luis F. Ibarra, Ricardo A. Medina, and Helmut Krawinkler. Hysteretic models that incorporate strength and stiffness deterioration. Earthquake Engineering and Structural Dynamics, 34(12):1489–1511, 2005.

[76] A. Ibrahimbegovic, B. Brank, and J. Korelc. Nonlinear shell problem formulation accounting for through-the-thickness stretching and its finite element implementation. pages 33–62, Stirling, UK, 2002. Saxe-Coburg Publications.

[77] B. M. Irons. Engineering applications of numerical integration in stiffness methods. AIAA Journal, 4(11):2035, 1966.

[78] L. Jiang and M. W. Chernuka. Simple four-noded corotational shell element for arbitrarily large rotations. Computers and Structures, 53(5):1123–1132, 1994.

[79] Stephen J. Wright Jorge Nocedal. Numerical optimization. Springer, New York, 2nd edition, 2006.

[80] E. P. Kasper and R. L. Taylor. A mixed-enhanced strain method. I. Geometrically linear problems. Computers and Structures, 75(3):237–50, 2000.

[81] G. Kerschen, J. C. Golinval, A. F. Vakakis, and L. A. Bergman. The method of proper orthogonal decomposition for dynamical characterization and order reduction of mechanical systems: An overview. Nonlinear Dynamics, 41(1-3):147–169, 2005.

[82] K. D. Kim, G. Z. Liu, and S. C. Han. A resultant 8-node solid-shell element for geometrically nonlinear analysis. Computational Mechanics, 35(5):315–331, 2005.

[83] S. Klinkel and W. Wagner. Geometrical non-linear brick element based on the EAS-method. International Journal for Numerical Methods in Engineering, 40(24):4529–4545, 1997.

[84] K. Krabbenhoft, A. V. Lyamin, S. W. Sloan, and P. Wriggers. An interior-point algorithm for elastoplasticity. International Journal for Numerical Methods in Engineering, 69(3):592–626, 2007.

[85] S. Lall, P. Krysl, and J. E. Marsden. Structure-preserving model reduction for mechanical systems. Physica D, 184(1-4):304–18, 2003.

[86] A. Legay and A. Combescure. Elastoplastic stability analysis of shells using the physically stabilized finite element SHB8PS. International Journal for Numerical Methods in Engineering, 57(9):1299–322, 2003.

[87] N. S. Less and K. J. Bathe. Effects of element distortions on the performance of isoparametric elements. International Journal for Numerical Methods in Engineering, 36:3553–3576, 1993.

[88] Yuqiu Long, Juxuan Li, Zhifei Long, and Song Cen. Area co-ordinates used in quadrilateral elements. Communications in Numerical Methods in Engineering, 15(8):533–545, 1999.

[89] H. Lu, K. Ito, K. Kazama, and S. Namura. Development of a new quadratic shell element considering the normal stress in the thickness direction for simulating sheet metal forming. Journal of Materials Processing Technology, 171(3):341–7, 2006.

[90] R. H. Macneal. Derivation of element stiffness matrices by assumed strain distributions. volume 70 of Nucl. Eng. Des. (Netherlands), pages 3–12, Netherlands, 1982.

[91] R. H. MacNeal. A theorem regarding the locking of tapered four-noded membrane elements. International Journal for Numerical Methods in Engineering, 24(9):1793–9, 1987.

[92] Richard H. MacNeal and Robert L. Harder. Proposed standard set of problems to test finite element accuracy. Finite Elements in Analysis and Design, 1(1):3–20, 1985.

[93] G. Maier. A matrix structural theory of piecewise linear elastoplasticity with interacting yield planes. Meccanica, 5(1):54, 1970.

[94] P. V. Marcal and I. P. King. Elastic-plastic analysis of two-dimensional stress systems by finite element method. International Journal of Mechanical Sciences, 9(3):143–155, 1967.

[95] The Mathworks. Matlab optimization toolbox (user's mannual, http://www.mathworks.com/products/optimization) ver. 7.9.0.529 r2009b,, 2009.

[96] A. Mendelson, S. S. Manson, and R. Reprt. Practical solution of plastic deformation problems in elastic-plastic range. Technical report, National Aeronautics and Space Administration (NASA), 1959.

[97] C. Miehe. A theoretical and computational model for isotropic elastoplastic stress analysis in shells at large strains. Computer Methods in Applied Mechanics and Engineering, 155(3-4):193–233, 1998.

[98] C. Militello and C. A. Felippa. First ANDES elements: 9-DOF plate bending triangles, (Final report, december 1989). Technical report, 1991.

[99] G. F. Moita and M. A. Crisfield. A finite element formulation for 3-D continua using the co-rotational technique. International Journal for Numerical Methods in Engineering, 39(22):3775–92, 1996.

[100] B. Nour-Omid and C. C. Rankin. Finite rotation analysis and consistent linearization using projectors. Computer Methods in Applied Mechanics and Engineering, 93:353–384, 1991.

[101] M.K. Nygard. The free formulation for nonlinear finite elements with application to shells. PhD thesis, Norwegian institute of technology, 1986.

[102] D. Pantuso and K. J. Bathe. A four-node quadrilateral mixed-interpolated element for solids and fluids. Mathematical Models and Methods in Applied Sciences, 5(8):1113–28, 1995.

[103] H. Parisch. An investigation of a finite rotation four node assumed strain shell element. International Journal for Numerical Methods in Engineering, 31:127–150, 1991.

[104] H. Parisch. A continuum-based shell theory for non-linear applications. International Journal for Numerical Methods in Engineering, 38(11):1855–83, 1995.

[105] K. C. Park and G. M. Stanley. A curved C0 shell element based on assumed natural-coordinate strains. Transactions of the ASME. Journal of Applied Mechanics, 53(2):278–90, 1986.

[106] A. Perez-Foguett and F. Armero. On the formulation of closest-point projection algorithms in elastoplasticity. II.Globally convergent schemes. International Journal for Numerical Methods in Engineering, 53(2):331–74, 2002.

[107] T. H. H. Pian. Derivation of element stiffness matrices by assumed stress distributions. AIAA J., 2:13331336, 1964.

[108] T. H. H. Pian. Element stiffness-matrices for boundary compatibility and for prescribed boundary stresses. Technical report, 1965.

[109] T. H. H. Pian and K. Sumihara. Rational approach for assumed stress finite elements. International Journal for Numerical Methods in Engineering, 20(9):1685–95, 1984.

[110] T. H. H. Pian and Tong. Basis of finite element methods for solid continua. Int. J. Numer. Meth. Engrg, 1:329, 1969.

[111] R. Piltner and R. L. Taylor. A systematic construction of b-bar functions for linear and non-linear mixed-enhanced finite elements for plane elasticity problems. International Journal for Numerical Methods in Engineering, 44(5):615–39, 1999.

[112] C. C. Rankin and F. A. Brogan. An element independent corotational procedure for the treatment of large rotations. Transactions of the ASME. Journal of Pressure Vessel Technology, 108(2):165–74, 1986.

[113] C. C. Rankin and B. Nour-Omid. The use of projectors to improve finite element performance. volume 30 of Comput. Struct. (UK), pages 257–67, UK, 1988.

[114] Charles Rankin. Application of linear finite elements to finite strain using corotation. volume 3 of Collection of Technical Papers - AIAA/ASME/ASCE/AHS/ASC Structures, Structural Dynamics and Materials Conference, pages 1942–1969, Newport, RI, United states, 2006. American Institute of Aeronautics and Astronautics Inc.

[115] S. Reese. A large deformation solid-shell concept based on reduced integration with hourglass stabilization. International Journal for Numerical Methods in Engineering, 69(8):1671–716, 2007.

[116] E. Riks. The application of Newton's method to the problem of elastic stability. Transactions of the ASME. Series E, Journal of Applied Mechanics, 39(4):1060–5, 1972.

[117] E. Riks. Bifurcation and stability, a numerical approach. Technical report, 1984.

[118] C. Sansour and F. G. Kollmann. Families of 4-node and 9-node finite elements for a finite deformation shell theory. An assessment of hybrid stress, hybrid strain and enhanced strain elements. Computational Mechanics, 24(6):435–447, 2000.

[119] M. Schwarze and S. Reese. A reduced integration solid-shell finite element based on the EAS and the ANS concept-Geometrically linear problems. International Journal for Numerical Methods in Engineering, 80(10):1322–55, 2009.

[120] Marco Schwarze and Stefanie Reese. A reduced integration solid-shell finite element based on the EAS and the ANS concept-Large deformation problems. International Journal for Numerical Methods in Engineering, 85(3):289–329, 2011.

[121] A. C. Scordelis and K. S. Lo. Computer analysis of cylindrical shells. American Concrete Institute – Journal, 61(5):539–561, 1964.

[122] P. Sharifi and E. P. Popov. Nonlinear buckling analysis of sandwich arches. 97(EM5):p 13971412–p 13971412, 1971.

[123] J. C Simo. Computational inelasticity, volume 7. Springer, New York ; Berlin, 1998.

[124] J. C. Simo and F. Armero. Geometrically non-linear enhanced strain mixed methods and the method of incompatible modes. International Journal for Numerical Methods in Engineering, 33(7):1413–1449, 1992.

[125] J. C. Simo, F. Armero, and R. L. Taylor. Improved versions of assumed enhanced strain tri-linear elements for 3D finite deformation problems. Computer Methods in Applied Mechanics and Engineering, 110(3-4):359–386, 1993.

[126] J. C. Simo and D. D. Fox. On a stress resultant geometrically exact shell model. I. Formulation and optimal parametrization. Computer Methods in Applied Mechanics and Engineering, 72(3):267–304, 1989.

[127] J. C. Simo, D. D. Fox, and M. S. Rifai. On a stress resultant geometrically exact shell model. III. Computational aspects of the nonlinear theory. Computer Methods in Applied Mechanics and Engineering, 79(1):21–70, 1990.

[128] J. C. Simo and J. G. Kennedy. On a stress resultant geometrically exact shell model. V. Nonlinear plasticity: Formulation and integration algorithms. Computer Methods in Applied Mechanics and Engineering, 96(2):133–71, 1992.

[129] J. C. Simo and M. Ortiz. A unified approach to finite deformation elastoplastic analysis based on the use of hyperelastic constitutive equations. Computer Methods in Applied Mechanics and Engineering, 49(2):221–45, 1985.

[130] J. C. Simo and M. S. Rifai. Class of mixed assumed strain methods and the method of incompatible modes. International Journal for Numerical Methods in Engineering, 29(8):1595–1638, 1990.

[131] J. C. Simo, M. S. Rifai, and D. D. Fox. On a stress resultant geometrically exact shell model. IV. Variable thickness shells with through-the-thickness stretching. Computer Methods in Applied Mechanics and Engineering, 81(1):91–126, 1990.

[132] M. V. Sivaselvan and A. M. Reinhorn. Hysteretic models for cyclic behavior of deteriorating inelastic structures. Technical report, 1999.

[133] Mettupalayam V. Sivaselvan, Oren Lavan, Gary F. Dargush, Haruhiko Kurino, Yo Hyodo, Ryusuke Fukuda, Kiochi Sato, Georgios Apostolakis, and Andrei M. Reinhorn. Numerical collapse simulation of large-scale structural systems using an optimization-based algorithm. Earthquake Engineering and Structural Dynamics, 38(5):655–677, 2009.

[134] Mettupalayam V. Sivaselvan and M Mostafa. Model reduction as a strategy for representing degradation due to local instabilities., 22-24 June 2009.

[135] Mettupalayam V. Sivaselvan and Andrei M. Reinhorn. Lagrangian approach to structural collapse simulation. Journal of Engineering Mechanics, 132(8):795–805, 2006.

[136] W. M. Smolenski. Statically and kinematically exact nonlinear theory of rods and its numerical verification. Computer Methods in Applied Mechanics and Engineering, 178(1-2):89–113, 1999.

[137] Nielen Stander, Anton Matzenmiller, and Ekkehard Ramm. Assessment of assumed strain methods in finite rotation shell analysis. Engineering computations, 6(1):58–66, 1989.

[138] H. Stolarski, T. Belytschko, and Lee Sang-Ho. A review of shell finite elements and corotational theories. Computational Mechanics Advances, 2(2):125–212, 1995.

[139] Strickli.Ja, W. E. Haisler, and Vonriese.Wa. Evaluation of solution procedures for material and or geometrically nonlinear structural-analysis. Aiaa Journal, 11(3):292–299, 1973.

[140] K. Y. Sze, W. K. Chan, and T. H. H. Pian. An eight-node hybrid-stress solid-shell element for geometric non-linear analysis of elastic shells. International Journal for Numerical Methods in Engineering, 55(7):853–78, 2002.

[141] K. Y. Sze, X. H. Liu, and S. H. Lo. Popular benchmark problems for geometric nonlinear analysis of shells. Finite Elements in Analysis and Design, 40(11):1551–69, 2004.

[142] K. Y. Sze and L. Q. Yao. A hybrid stress ANS solid-shell element and its generalization for smart structure modelling. Solid-shell element formulation. International Journal for Numerical Methods in Engineering, 48(4):545–64, 2000.

[143] I. C. Taig and R. I. Kerr. Some problems in the discrete element representation of aircraft structures in Matrix Methods of Structural Analysis. Technical report, 1966.

[144] R. L. Taylor, J. C. Simo, O. C. Zienkiewicz, and A. C. H. Chan. The patch test- A condition for assessing FEM convergence. International Journal for Numerical Methods in Engineering, 22(1):39–62, 1986.

[145] SP. Timoshenko and J.M. Gere. Theory of elastic stability, volume 2nd. MacGraw-Hill, New York, 1963.

[146] SP. Timoshenko and S. Woinowsky-Krieger. Theory of plates and shells. McGraw-Hill, New York, 2nd edition, 1959.

[147] L. Vu-Quoc and X. G. Tan. Optimal solid shells for non-linear analyses of multilayer composites. I. Statics. Computer Methods in Applied Mechanics and Engineering, 192(9-10):975–1016, 2003.

[148] W. Wagner, S. Klinkel, and F. Gruttmann. A robust non-linear solid shell element based on a mixed variational formulation. Computer Methods in Applied Mechanics and Engineering, 195(1-3):179–201, 2006.

[149] G. Wempner. Finite elements, finite rotations and small strains of flexible shells. International Journal of Solids and Structures, 5(2):117–54, 1969.

[150] G. Wempner, D. Talaslidis, and C. M. Hwang. A simple and efficient approximation of shells via finite quadrilateral elements. Transactions of the ASME. Journal of Applied Mechanics, 49(1):115–20, 1982.

[151] E. L. Wilson, R. L. Taylor, W.P. Doherty, and J. Ghabussi. Incompatible displacement models. In S. J. Fenves, N. Perrone, A.R. Robinson, and W.C. Schnobrich, editors, Numerical and Computer Models in Structural Mechanics, pages 43–57. Academic Press, New York, 1973.

[152] Chen Xiao-Ming, Cen Song, Long Yu-Qiu, and Yao Zhen-Han. Membrane elements insensitive to distortion using the quadrilateral area coordinate method. Computers & Structures, 82(1):35–54, 2004.

[153] O. C. Zienkiewicz and R. L. Taylor. The finite element patch test revisited. A computer test for convergence, validation and error estimates. volume 149 of Comput. Methods Appl. Mech. Eng. (Switzerland), pages 223–54, Switzerland, 1997. Elsevier.